DIRECT OBSERVATIONS OF NICKEL SILICIDE FORMATION ON (100) Si AND $Si_{0.75}Ge_{0.25}$ SUBSTRATES USING *IN-SITU* TRANSMISSION ELECTRON MICROSCOPY

RAMESH NATH S/O PREMNATH

(B.Sc.(Hons.), NUS)

A THESIS SUBMITTED

FOR THE DEGREE OF MASTER OF SCIENCE

DEPARTMENT OF MATERIALS SCIENCE

NATIONAL UNIVERSITY OF SINGAPORE

2004

Acknowledgements

I would like to express my utmost gratitude and thanks to my supervisor Professor Mark Yeadon for this project accomplishment. Without his patient guidance, this work will not have been possible. From my early days of ignorance, he had been there to provide knowledge, mentorship and assistance whenever difficulties are encountered. I am also grateful for Prof. Yeadon's invaluable coaching in the handling of his precious transmission electron microscope and the knowledge of the operating techniques and little tricks here and there that he transferred to the me. It is a joy to work with him in the laboratory and get to know him as a friend.

I am also deeply indebted to Dr. Christopher Boothroyd for his mentorship and guidance in helping me better understand the principles of the transmission electron microscope and the Gatan Image Filter. The long discussions we had over tea have definitely helped shaped me to be a better microscopist.

I would also like to thank Dr. Lap Chan (CSM) for being an excellent teacher and facilitator who has helped to put this project together.

I must particularly express my most sincere gratitude to my colleagues and also my friends, Dr. Foo Yong Lim and Soo Chi Wen, for their advice, understanding and help along the way.

I would also like to thank my loved ones who were very supportive of what could be a misadventure, but happily, turned out to be a great learning experience and project.

Finally, I would like to thank Professor Chow Gan Moog, Professor Chua Soo Jin and Professor Alfred Huan for the provision of the laboratory facilities, which made this project possible.

Table of contents

Acknowledgements……………………………………………………………i
Table of contents……………………………………………………………ii
Summary…..…………………………………………………………….. vi
List of tables…………………………………………………………….…..viii
List of figures………………………………………………………….......ix
Nomenclature…………………………………………………………… xvi
List of publications...………………………………………………………xviii

1 Introduction 1

2 Literature Review and Thin Films 5

2.1 Silicon-germanium technology 5

2.1.1 Introduction to SiGe technology 5

2.1.2 $Si_{1-x}Ge_x$ growth issues 7

2.2 Silicide technology 9

2.2.1 Introduction to silicides 9

2.2.2 Formation of silicides for technological applications 11

2.2.3 Requirements for silicides in silicon integrated circuits 13

2.2.4 Comparison of nickel silicide with other silicides 15

2.2.4.1 Titanium disilicide 15

2.2.4.2 Cobalt disilicide 16

2.2.4.3 Nickel monosilicide 19

2.2.4.4 Nickel silicidation on $Si_{1-x}Ge_x$ substrates 22

2.3 Principles of thin films 23

2.3.1 Mechanism for the formation of thin film nickel silicide phases . 24

2.3.2 Agglomeration of thin films ... 27

References ... 29

3 Principles of transmission electron microscopy ... 32

3.1 Introduction to transmission electron microscopy ... 32

3.2 Important electron interactions with the sample in TEM ... 33

3.3 Diffraction ... 36

3.3.1 Theory of electron diffraction ... 36

3.3.2 Structure factor ... 43

3.3.3 Selected area electron diffraction ... 45

3.4 Bright and dark field imaging ... 47

3.5 Basic optics operation of JEM 2000V TEM ... 49

References ... 51

4 Experimental setup ... 52

4.1 The MERLION system ... 52

4.2 Preparation of Si (100) substrates ... 55

4.3 Preparation of $Si_{0.75}Ge_{0.25}$ (100) substrates ... 56

4.4 Nickel deposition ... 58

4.5 Resistive annealing ... 59

4.6 Observation and data collection ... 60

4.6.1 Gatan DualView 780 digital camera ... 61

4.6.2 Gatan Image Filter ... 61

4.6.2.1 Theory of operation ... 62

4.6.2.2 Basic concepts of EELS 64

4.6.2.3 Uses of EELS Data 66

4.6.2.4 EFTEM... 68

4.6.2.5 Selecting an energy loss 68

References 69

5 Results and discussion I: Ni on Si (100) 70

5.1 Ni on clean Si (100) 71

5.1.1 Preliminary inspection of clean Si (100) 71

5.1.2 Nickel deposition on clean Si (100)... 72

5.1.3 Annealing of the 12nm Ni film on clean Si (100) 73

5.2 Ni on oxide-covered Si (100).. 87

5.2.1 Preliminary inspection of oxide-covered Si (100) 87

5.2.2 Nickel deposition on oxide-covered Si (100) 88

5.2.3 Annealing of the 12nm Ni film on oxide-covered Si (100) 88

5.2 Summary of Chapter 5 92

References 93

6 Results and discussion II: Ni on relaxed $Si_{0.75}Ge_{0.25}$ (100)...................... 95

6.1 Preliminary inspection of relaxed $Si_{0.75}Ge_{0.25}$ (100) 96

6.2 Nickel deposition on relaxed $Si_{0.75}Ge_{0.25}$ (100) 99

6.3 Annealing of the 12nm Ni film on relaxed $Si_{0.75}Ge_{0.25}$ (100) 100

6.4 Summary of Chapter 6 112

References 113

7 Conclusion 115

Appendix: Indexing of SAED patterns 118

A.1 Identification of major spots and calibration of SAED patterns 118

A.1.1 Step one 118

A.1.2 Step two and three 120

A.2 Calibration and indexing of SAED pattern in Figure 5.1 (b) 121

A.3 Indexing of SAED pattern in Figure 5.2 (b) 124

A.4 Indexing of SAED pattern in Figure 5.4 (a) 125

A.5 Indexing of SAED pattern in Figure 5.4 (c) 128

A.6 Indexing of SAED pattern in Figure 5.15 (b) 131

Summary

Recent success in the growth technology of $Si_{1-x}Ge_x$ epitaxial thin films has found its potential in high-speed electronic device applications for ultra large-scale integrated (ULSI) circuits, such as complementary metal-oxide semiconductor (CMOS) technology. One of the requirements for the device structures is to form a good ohmic contact that will not degrade the device performance, where metal silicides have played a key role. It is anticipated that they will continue to be used with strained-Si and $Si_{1-x}Ge_x$ device technologies. There is considerable interest in the use of NiSi due to its lower silicon consumption and one-step low temperature of formation. A severe disadvantage of NiSi thin layers, however, is the propensity for agglomeration above ~400ºC and transformation to the high-resistivity nickel disilicide phase between 650 and 750ºC.

In this work, a modified TEM for *in-situ* studies of the thermal reaction of 12nm Ni thin films on (100) Si and relaxed $Si_{0.75}Ge_{0.25}$ substrates was used. Real-time direct observations of the formation and agglomeration of nickel monosilicide films, followed by the mechanism of the nucleation of $NiSi_2$ at higher temperatures in both cases were made. In the case of Ni on (100) Si, two sets of experiments were carried out, namely on clean and oxide-covered Si (100). For the Ni on clean Si experiment, a uniform and pinhole-free but highly strained polycrystalline thin NiSi film was formed at 300ºC. The onset of agglomeration of the NiSi film was observed at a temperature range of 400-500ºC which became more severe at higher temperatures to form isolated NiSi islands. The nucleation of $NiSi_2$ was first observed at 650ºC, occurring at the edges of the NiSi islands, at the free surface of the substrate. Observations are understood from a consideration of the reduction in the free energy barrier for nucleation of $NiSi_2$ at the free

surface of the film where enhanced strain relaxation can occur. For the Ni on oxide-covered Si (100) experiment, epitaxial $NiSi_2$ was the first silicide phase to form at 200ºC with the coexistence of the NiSi and $NiSi_2$ phases in the temperature range of 200-650ºC. At temperatures above 650ºC, the NiSi layer was observed to be entirely consumed to form $NiSi_2$. Observations suggest that the native oxide layer acts as a diffusion barrier, mediating the flux of Ni atoms to the Si surface. This promotes direct nucleation of $NiSi_2$, at temperatures as low as 150ºC.

In the case of Ni on (100) $Si_{1-x}Ge_x$, the agglomeration process of the monosilicide film started to occur at 400°C and became more severe at higher temperatures. EELS and EFTEM analysis at this temperature revealed that Ge atoms from the monosilicide islands had segregated to the grain boundaries and areas of bare substrate making these areas Ge-rich. The formation of $NiSi_2$ islands was first observed after heating in the temperature range of 940-960°C for several minutes, which is ~300°C higher than in the case of Ni on Si (100). This is attributed to the reduced free energy of formation of $NiSi_2$ in the presence of Ge.

List of tables

Table 2.1: ITRS 2001 update of relevant data concerning silicides............................ 14

Table 2.2: Comparison of physical properties of $TiSi_2$, $CoSi_2$ and NiSi 21

Table A.1: Ratio of square of d-spacing between Si (200) and Si (220) planes. 120

Table A.2: Showing the comparison and analysis of the calculated d-spacings of the Ni rings with d-spacing from a standard JCPDS file 04-0850............................. 125

Table A.3: Showing the comparison and analysis of the calculated d-spacings of Figure 5.4 (a) spot pattern with d-spacings from a standard JCPDS file 38-0844 127

Table A.4: Showing the calculated angles between planes of atoms with d-spacings matching closely with experimental data in Figure 5.4 (a).................................. 127

Table A.5: Showing the comparison and analysis of the calculated d-spacings of Figure 5.4 (c) spot pattern with d-spacings from a standard JCPDS file 38-0844 129

Table A.6: Showing the calculated angles between planes of atoms with d-spacings matching closely with experimental data in Figure 5.4 (c).................................. 130

Table A.7: Showing the comparison and analysis of the calculated d-spacings of Figure 5.15 (b) spot pattern with d-spacings from a standard JCPDS file 38-0844 132

Table A.8: Showing the calculated angles between planes of atoms with d-spacings matching closely with experimental data in Figure 5.15 (b) 132

List of figures

Figure 2.1: Polycide and Salicide processes: (a) Polycide structure, (b) Salicide structure.. 12

Figure 3.1: Diagrammatic representation of the interaction between a beam of high-energy incident electrons and a specimen. A number of interactions take place. Transmission electron microscopy (TEM) uses unscattered, inelastically scattered, and narrow-angle elastically scattered electrons 34

Figure 3.2: Defining the incident and diffracted vectors. **K** represents difference between incident ($\mathbf{k_I}$) and ($\mathbf{k_D}$) wave vectors... 38

Figure 3.3: Showing the constructive and destructive interference of two wave fronts 39

Figure 3.4: Ewald sphere construction showing the sphere superimposed on the reciprocal lattice points. Points that intersect the sphere will satisfy the Bragg condition and will appear in the diffraction pattern.. 40

Figure 3.5: (a) Relationship between diffracted intensity and excitation error **s**. (b) Illustrating the relationship between diffracted intensity and excitation error, where relrods intercepted by the Ewald sphere further away from the origin O, are lower in intensity due to excitation error 42

Figure 3.6: (a) The insertion of a selected area aperture allows the formation of the diffraction pattern only from the selected area. (b) Schematic of the formation and geometry of a diffraction spot in relation to the transmitted beam........... 46

Figure 3.7: (a) Objective aperture selecting the on-axis transmitted beam to form a bright field image. (b) Objective aperture selecting the off-axis diffracted

beam to form a displaced dark field image. (c) Another method to form a dark field image with the objective aperture selecting the on-axis diffracted beam. 48

Figure 3.8: Schematic of condenser and objective lens of JEOL 2000V 49

Figure 3.9: Schematic of image forming system in JEOL 2000V 50

Figure 4.1: The MERLION system.. 53

Figure 4.2: Steps involved in preparing Si (100) substrates 55

Figure 4.3: Steps involved in preparing the $Si_{0.75}Ge_{0.25}$ (100) substrates 57

Figure 4.4: The UHV evaporator EFM3 as attached to the MERLION system.......... 58

Figure 4.5: Graph of Current input versus Temperature reading from the Si substrate (the temperatures are measured using a pyrometer), x-axis indicates current, each interval is 0.1, unit: ampere; y axis indicates temperature, each interval is 50, unit: degree Celsius... 60

Figure 4.6: The Gatan DualView system as attached to the MERLION system......... 61

Figure 4.7: The Gatan Image Filter system as attached to the MERLION system...... 62

Figure 4.8: Schematic of the Gatan Image Filter.. 63

Figure 4.9: Showing the electron shells and transitions.. 65

Figure 5.1: Showing (a) EELS spectrum, (b) SAD and bright field image of a clean Si (100) substrate.. 72

Figure 5.2: Corresponding (a) bright field image and (b) SAED for as deposited 12nm Ni on Si (100) 73

Figure 5.3: Strain contrast is observed in (a) bright field and (b) dark field image with the corresponding SAED pattern in (c) showing Si and NiSi reflections......... 74

Figure 5.4: The SAED patterns in (a) and (c) shows an example of two different orientation of NiSi grains with respect to the Si (100) substrate. The red and white dotted line in both SAED patterns represents the reflections of Si and NiSi phase respectively. The simulated diffraction pattern indexed with NiSi reflections are shown in (b) and (d) respectively 76

Figure 5.5: Thermal grooving starts to occur at grain boundaries in (a) indicating the onset of agglomeration. This is followed by liquid-like void growth exposing the Si substrate in (b) at 400-500ºC. 77

Figure 5.6: Showing severe agglomeration occurring in (a) and (b). The nucleation of the new phase was observed at 'N' in (c) and seen propagating through island 'I' until the reaction terminated in (f) 78

Figure 5.7: Images (a) - (e), captured from video recording, illustrates the transformation of island 'I' into an island with two grain boundaries. The time scale of the movement of the boundaries (indicated by the red doted lines) as it propagates through the island is presented in the images. 80

Figure 5.8: The bright field image in (a) shows the NiSi:$NiSi_2$ interface existing in a single island at 650ºC. SAED taken at either side the grain boundary indicates the presence of the $NiSi_2$ and NiSi phase in (b) and (c) respectively. 81

Figure 5.9: Images (a) to (b) outlines the stages of the expansion of the NiSi portions of island 'I'. This is followed by the propagation of the NiSi:$NiSi_2$ interface at one end of the island, until the whole NiSi portion is transformed into $NiSi_2$ as shown in images (c) - (f). The dark field image in (f), was imaged using the $NiSi_2$ (200) reflection outlines the partially formed $NiSi_2$ island. The images in (g) and (h) represents the SAED pattern, bright and dark field images of the fully transformed $NiSi_2$ island 'I' 82

Figure 5.10: Schematic diagram of the transformation from NiSi to $NiSi_2$ of the island 'I' shown in Figure 5.7(a). The diagram is drawn with respect to the fiducial line Z-Z' on island 'I'. (a) Plan view representation of the initial $NiSi_2$ nucleation of NiSi, and cross-sectional representations of (b) initial $NiSi_2$ nucleation, (c) propagation of the NiSi:$NiSi_2$ phase boundaries laterally through the island, (d) lateral expansion of the NiSi regions, and (e) completion of the propagation of the NiSi:$NiSi_2$ phase boundaries through the remainder of the island... 84

Figure 5.11: Reproduced from Wong *et al.* showing the cross-sectional TEM image of NiSi and $NiSi_2$ on Si(100) at 700ºC. The image outlines the sharp faceting between $NiSi_2$ island and Si. 86

Figure 5.12: (a) EELS spectrum showing the oxygen K edge at 532eV, (b) bright field image and (c) SAED of an oxide-covered Si (100)................................. 87

Figure 5.13: Corresponding (a) bright field images and (b) SAED for as deposited 12nm Ni on oxide-covered Si (100).. 88

Figure 5.14: SAED (a) and bright field image (b) of sample heated to 200ºC, showing the formation of $NiSi_2$ with some unreacted Ni. The red dotted line in the SAED represents the Si (100) reflections 89

Figure 5.15: The bright field image in (a) represents the morphology of the sample after ten minutes at 200ºC. The corresponding SAED pattern in (b) shows the formation of NiSi. The red and blue dotted line represents the Si and $NiSi_2$ reflections respectively. The simulated electron diffraction in (c) shows the diffraction pattern of $[\bar{1}02]$ NiSi zone axis (in purple spots)............................ 90

Figure 5.16: At 650ºC, the NiSi phase was consumed to form solely $NiSi_2$ phase as presented in the (a) SAED and (b) bright field image. The red and blue dotted line represents the (100) Si and $NiSi_2$ reflections respectively........................ 92

Figure 6.1: Showing the EELS spectrum taken at low energy loss in (a) with the absence of the carbon and oxygen edges. In (b), the EELS spectrum taken at higher energy loss is used to quantify the elemental composition of silicon and germanium, which was found to be 74.1% and 25.9% respectively. 97

Figure 6.2: Showing (a) SAED and (b) bright field image of a clean relaxed $Si_{0.75}Ge_{0.25}$ substrate.. 98

Figure 6.3: Corresponding (a) SAED and (b) bright field image of as deposited 12nm Ni on a $Si_{0.75}Ge_{0.25}$ substrate 99

Figure 6.4: The bright field image is shown in (a), of 12nm Ni on $Si_{0.75}Ge_{0.25}$ sample at 350 ºC. The corresponding SAED in (b) is indexed with $Si_{0.75}Ge_{0.25}$ plane indices. The red dotted line represents the unit $Si_{0.75}Ge_{0.25}$ (100) reflections. The simulated diffraction pattern in (c) shows the matching spot pattern of a NiSi super-cell. The simulated data is indexed with NiSi plane indices. 101

Figure 6.5: The agglomeration of the Ni(SiGe) is observed in the bright field image in (a) of the sample annealed to 400ºC with the corresponding dark field image in (b) of the silicide islands.. 102

Figure 6.6: The bright field image in (a) showing the area where the EELS analysis was done, in the area of bare substrate for (b) and area of the monosilicide islands in (c). The percentage values represent the combined composition values of the three elements... 103

Figure 6.7: Showing the EFTEM images of (a) Si, (b) Ge and (c) Ni taken of the sample annealed at 550ºC. 104

Figure 6.8: Showing the bright field images of $Ni(Si_{1-y}Ge_y)$ (where $y<0.25$) islands of the sample at 700ºC. An increase in mass-thickness image contrast suggests that the islands have become thicker. The corresponding SAED in (b) of the monosilicide island shows the crystallographic relation: NiSi $[\bar{1}\,\bar{2}\,1]$ // Si [100]. 105

Figure 6.9: Reproduced from Pey *et al.*[4] showing a cross-sectional TEM image of Ni-silicided $Si_{0.75}Ge_{0.25}$ annealed at (a) 500 and (b) 800ºC. Comparing the two images, the monosilicide islands are much bigger and diffused deeper into the substrate at 800ºC... 106

Figure 6.10: Showing the $NiSi_2$ grain with characteristic square plan view shape in (a), with the sides of the grain along the <110> directions. Mass-thickness contrast of the square grain reveals the characteristic inverted pyramidal shape of the $NiSi_2$ phase. The corresponding SAED in (b) (unit cell of Si and $NiSi_2$ in red and blue dotted line respectively) and dark field image in (c) shows the cube-on-cube relationship with the substrate with the crystallographic relation: $NiSi_2$ (100) // Si (100), $NiSi_2$ [100] // Si [100] 108

Figure 6.11: Showing areas of dark and bright patches as the monosilicide islands begin to creep along the surface of the $Si_{0.75}Ge_{0.25}$ substrate upon reaching the temperature range of 940-960ºC 110

Figure 6.12: EFTEM images were obtained for the area of the sample at 940-960ºC shown in (a). The Ni map in (b) outlines the area with the monosilicide islands. From the (c) Ge and (d) Si maps it can be observed that the bright and

dark patches form the bright field image in (a) are localized areas with lower Ge concentration but rich in Si 111

Figure 7.1: Showing a schematic diagram comparing the thermal reaction of 12nm Ni on Si (100) and relaxed $Si_{0.75}Ge_{0.25}$ (100) substrate.. 117

Figure A.1: Showing SAED pattern of a clean Si (100) sample for 12nm Ni on Si experiment from Figure 5.1 (b)... 121

Figure A.2: Showing a simulated diffraction pattern of single crystal Si (100) along the [100] zone axis 123

Figure A.3: SAED pattern for as deposited 12nm Ni on Si (100) sample from Figure 5.2 (b)... 125

Figure A.4: SAED pattern of NiSi film from Figure 5.4 (a) 126

Figure A.5: Showing a simulated diffraction pattern of orthorhombic NiSi along the [$1\bar{3}1$] zone axis 128

Figure A.6: SAED of NiSi film from Figure 5.4 (c) 129

Figure A.7: Showing a simulated diffraction pattern of orthorhombic NiSi along the [010] zone axis 130

Figure A.8: SAED pattern from Figure 5.16(b)... 131

Figure A.9: Showing a simulated diffraction pattern of orthorhombic NiSi along the [$\bar{1}02$] zone axis 132

Nomenclature

BF	Bright field
CMOS	Complementary metal oxide semiconductor
Co	Cobalt
$CoSi_2$	Cobalt Disilicide
DF	Dark field
EELS	Electron energy loss-loss spectroscopy
EFTEM	Energy filtered transmission electron microscope/microscopy
Ge	Germanium
HF	Hydrofluoric
MBE	Molecular beam epitaxy
MERLION	Modified Electron-microscope for ReaL-time In-situ Observations on a Nanoscale
MODFET	Modulation-doped field effect transistor
MOSFET	Metal oxide semiconductor field effect transistor
Ni	Nickel
NiSi	Nickel monosilicide
$NiSi_2$	Nickel Disilicide
OME	Oxide mediated epitaxy
Polycide	Polycrystalline silicon-silicide
RTA	Rapid thermal annealing
SAED	Selected area electron diffraction
Salicide	Self-aligned silicide
Si	Silicon
SiGe	Silicon germanium alloy

SiO_2	Silicon dioxide
SPE	Solid phase epitaxy
TEM	Transmission electron microscope/microscopy
Ti	Titanium
$TiSi_2$	Titanium disilicide
UHV	Ultra-high vacuum
ULSI	Ultra large scale integration

List of publications

1. **Direct observations of the nucleation and growth of $NiSi_2$ on Si (001)**
   M. Yeadon, R. Nath, C.B. Boothroyd and D. Z. Chi,
   13th International Conference on Microscopy of Semiconducting Materials
   Churchill College, University of Cambridge, 31 March – 3 April (2003).

2. **Direct Observations of the Mechanism of Nickel Silicide Formation on (100) Si and $Si_{0.75}Ge_{0.25}$ substrates**
   R. Nath and M. Yeadon
   Electrochemical and Solid-State Letters, Volume 7, Number 10, (2004), G231.

Chapter 1 Introduction

The continual advancement of the deep submicron ultra large scale integrated (ULSI) technology to enhance circuit and system speed has resulted in smaller device dimensions. This has made the fabrication process of integrated circuits more complex. Although significant progress has been made to the equipment and techniques, problems associated with interconnections and contacts, such as parasitic resistance, capacitance and inductance are now beginning to influence circuit performance. Silicides have been a subject of research for many years for a variety of applications in the technology, mostly as contact and interconnect materials. Their compatibility with conventional Si processing, ability to form ohmic contacts with low resistivity and resistance to chemicals has given them an advantage over other choices of materials. However as device structures get smaller, thermal reactions such as grain growth, phase transformation, agglomeration, dopant redistribution and segregation can significantly undermine the electrical properties of silicide interconnects and contacts. To overcome this problem, engineers and scientists must have a thorough understanding of the physical, chemical and atomistic mechanism behind the failure process.

With $Si_{1-x}Ge_x$ substrates emerging as a mature platform technology for high-speed complementary metal oxide semiconductor (CMOS) device applications, metal silicides continue to play a key role in the fabrication of ohmic device contacts and it is anticipated that they will continue to be used with strained-Si and $Si_{1-x}Ge_x$ device technologies. As device dimensions scale into the deep submicron size regime, there is considerable interest in the use of NiSi as a replacement for $CoSi_2$ due in part to the lower silicon consumption and reduced temperature of formation. A severe disadvantage for thin

layers, however, is the propensity for agglomeration above ~400ºC and transformation to the high-resistivity nickel disilicide phase between 650 and 750ºC. The reaction NiSi + Si $\Rightarrow$ $NiSi_2$ is nucleation controlled since the difference in free energies of NiSi and $NiSi_2$ is small, and the surface energy associated with nuclei formation dominates the reaction. The coexistence of NiSi and $NiSi_2$ in agglomerated films on Si (100) has been observed previously, and a correlation between $NiSi_2$ nucleation and NiSi agglomeration proposed. However, experimental confirmation has yet to be obtained; in the case of Ni deposited onto $Si_{1-x}Ge_x$ substrates, the formation of $NiSi_2$ has yet to be reported.

In the present work, the formation and agglomeration of nickel monosilicide on (100) Si and $Si_{0.75}Ge_{0.25}$ substrates is studied during annealing of blanket Ni thin films within the column of an ultrahigh vacuum in-situ transmission electron microscope (TEM). Direct observations of the mechanism of nucleation and growth of $NiSi_2$ from NiSi on Si (100) are presented. The formation of the disilicide phase on epitaxial $Si_{0.75}Ge_{0.25}$ alloy films is observed for the first time.

The following paragraphs give a brief chapter-by-chapter outline of this thesis. The first section in Chapter 2 describes the motivation behind the potential applications of SiGe based devices in the area of high-speed electronic and optoelectronic devices. The following section describes the application and the requirements of silicides in the semiconductor industry. A detailed review of the three commonly used silicides, namely $TiSi_2$, $CoSi_2$ and NiSi, is presented. The theory of thin film formation by diffusion- and nucleation- controlled mechanism is covered in the third section. The kinetics and theory embedded in the agglomeration of thin films is also included in this section.

Since the experiments are carried out in the pole piece of an ultra-high vacuum transmission electron microscope (TEM), Chapter 3 covers the basic theory behind transmission electron microscopy. The discussion is limited to the background information necessary to understand the data that is presented in the Chapter 5 and 6. Firstly a brief introduction to TEM together with analogies to light microscopy is outlined. Next the fundamental electron interactions with an electron transparent sample are discussed. This is followed by the principles of electron diffraction, which is applied to the actual operation of obtaining a selected area diffraction pattern in a TEM. Subsequently, the mechanism for the formation of contrast in bright and dark field imaging is explored. Finally, the overall basic operation of the lenses in the different operating modes of the JEOL 2000V TEM is covered. The JEOL 2000V is the basic TEM, which is part of the highly modified *in-situ* ultra-high vacuum (UHV) TEM used in this study.

In Chapter 4 the experimental details of this study are provided. The first section describes the highly modified *in-situ* ultra-high vacuum (UHV) TEM, which is the primary analytical tool, used in this study. The preparation and cleaning of the Si and $Si_{0.75}Ge_{0.25}$ substrates is discussed in the second and third sections, respectively. The following two sections describe the equipment and conditions used for *in-situ* deposition of the nickel film using electron beam evaporation followed by the *in-situ* annealing using direct resistive heating. Finally the data acquisition tools, the Gatan Imaging Filter (GIF) and DualView digital cameras used throughout this study are presented.

Chapter 5 describes the deposition and annealing of a 12nm Ni film on (i) clean and (ii) oxide-covered Si (100), while Chapter 6 covers the deposition and annealing of a

12nm Ni film on a relaxed $Si_{0.75}Ge_{0.25}$ (100) substrate. For each chapter, the first section presents electron energy loss spectroscopy (EELS), TEM images and selected area electron diffraction (SAED) data obtained from the preliminary inspection of the cleanliness and composition of the substrate. The following section describes the data obtained during the *in-situ* deposition of the nickel film on the substrate. The thermal reaction between the nickel film and the underlying substrate is presented in the next section. At each annealing temperature step, phase transformations and thermal stability for the different nickel silicide phases are presented and discussed with reference to SAED patterns, EELS spectra, bright and dark field images.

Chapter 7 summarizes the primary conclusions of this study and describes further proposed experiments. Lastly, the appendix chapter covers the detailed explanation and steps taken in the indexing of selected area electron diffraction (SAED) patterns indicated in Chapter 5.

Chapter 2 Literature review and thin films

2.1 Silicon-germanium technology

2.1.1 Introduction to SiGe technology

The present integrated circuit market is mostly dominated by the silicon-based technologies. There are many reasons for this dominance, but the most important one is the low cost of fabrication of Si chips[1]. This is due to the ability of conventional Si processing technology to fabricate billions of transistors, all with near identical properties across ever increasing diameter slices of silicon. The phenomenal yields that are obtained on a CMOS line are far from achievable from other types of technology. In addition, the natural properties of silicon to form silicon insulators such as SiO_2 and Si_3N_4 have made fabrication processes of silicon-based chips much cheaper compared to the other alternative materials.

From the 1960s, device features have continued to decrease in size exponentially governed by Moore's Law. This has lead to an increase in the density and performance of CMOS as well as a decrease in the cost per transistor on a CMOS chip over the years. However, this trend has also led to the cost of fabrication plants scaling upwards at an exponential rate. Therefore, with the huge amount of capital and knowledge presently tied up in both Si production and research, it is difficult to persuade companies to change to completely new and untried technologies. CMOS is so cheap and dominant that one will only use other materials in applications where Si cannot compete and this has allowed them to dominate in areas such as optoelectronics and analogue or high-speed markets (e.g. radio frequency).

One such promising material is $Si_{1-x}Ge_x$, of which layers may be grown pseudomorphically on silicon wafers and which allows one to engineer the bandgap, energy band structure, effective masses, mobility and numerous other properties while fabricating circuits using conventional Si processing and tools[2]. The reason for this ability for band gap engineering is due to the strain produced in the layer of $Si_{1-x}Ge_x$ when grown epitaxially on Si substrates. The 4.2% larger lattice constant of Ge in comparison with Si, introduces a compressive biaxial strain in the $Si_{1-x}Ge_x$ layer. This asymmetry of the strain with respect to the (100) growth direction leads to a splitting of the six-fold degenerate conduction band and also of the heavy-hole/ light-hole valence band degeneracy. The strain-induced splitting of the valleys in the conduction band by over 300meV allows only the two Δ_2 valleys to be occupied even at room temperature compared to six valleys in Si, producing a significant reduction in intervalley scattering[3]. These provide the lowest possible mass of $m = 0.19m_o$ for electron transport in the (100) quantum well plane and leads to drastic improvement electron mobility, which is more than a factor of 3 higher than in conventional Si devices. Holes also have increased mobility[4] in strained $Si_{1-x}Ge_x$ due to subband splitting, which reduces scattering and the effective mass.

Many SiGe products are already available in the semiconductor market in numerous applications, due to extensive research in this field. The first $Si_{1-x}Ge_x$ device to be integrated with a conventional CMOS production line is the Si/SiGe heterojunction bipolar transistor (HBT). In a bipolar fabrication process, the thin $Si_{1-x}Ge_x$ base layer can be doped to higher densities, which reduces the resistivity of the base and hence the time constant for switching. The reduced bandgap of the base also helps to increase the gain of

the transistor as the heterojunction discontinuity between the base and the emitter reduces the hole injection into the emitter. In addition, grading the Ge content in the base builds an electric field into the device and accelerates the carriers across the base, therefore increasing the speed of the transistor.

One of the most exciting $Si_{1-x}Ge_x$ results to date has been achieved with modulation doped field effect transistors (MODFETs) grown on virtual substrates, which have been developed from successful experience gained with III-V MODFETs. Modulation doped strained-Si quantum wells grown on relaxed $Si_{1-x}Ge_x$ MODFETs yield faster transistors than any other p-channel transistor in literature. This is due to an increase in the carrier mobility by a factor of 2 to 3.

2.1.2 $Si_{1-x}Ge_x$ growth issues

However, if the thickness of the $Si_{1-x}Ge_x$ layers grown pseudomorphically on bulk Si substrates reaches above the critical thickness, the layer relaxes by forming misfit dislocations. If the volume density of misfit dislocations is substantially high, many of these misfit dislocations can interact to create threading dislocations that thread to the surface. These defects can form a dislocation density at the surface of order 10^{12} cm^{-2}, which can significantly reduce the mobility and electronic quality of the material. This can be characterized by a typical crosshatch pattern oriented along (110) on the $Si_{1-x}Ge_x$ layer surface. However, if a step or linearly graded buffer is grown to the desired Ge concentration at high enough temperature and at low enough grading rate, then dislocation density may be reduced to below 10^6 cm^{-2} for $Si_{0.7}Ge_{0.3}$. This is due to faster growth at higher temperatures, which allows a lower Ge gradient and also increases the

velocity of dislocations threading through the sample, which thread down into the Si substrate rather than up to the surface. Therefore, the nucleation of additional dislocations is suppressed with graded layer growth. Such substrates are termed virtual substrates.

However nucleation of additional dislocations is not suppressed when thicker graded layers are grown to higher Ge concentration. The crosshatch surface roughness interacts with the strain fields due to the misfit dislocations, blocking threading dislocation glide and leading to the pile-up of the dislocations. The formation of pile-ups causes the nucleation of additional threading dislocations, as the trapped threading dislocations can no longer contribute to strain relief. Although growth on off cut Si has been shown to reduce the number of pile-ups by improving the surface roughness, it does not eliminate the problem completely. In an earlier work by Currie *et al.*[5], they demonstrated a technique utilizing chemical-mechanical polishing (CMP) which allowed them to grow relaxed graded buffer layers to 100% Ge without an increase in the threading dislocation density. The graded layers were grown at a rate of 10% Ge μm^{-1}, and at the 50% Ge graded buffer layer, the CMP step was introduced to remove 5000Å of the 1.5μm 50% Ge cap layer. It was found that the additional step arrested the increase in threading dislocation density with Ge concentration. Hence, the planarization of the surface during this step must free the threads seen in pile-ups in the sample and allow the dislocations to relieve the strain introduced in the subsequent growth, eliminating the driving force for the nucleation of additional threading dislocations. This was proven in the results when a 100% Ge graded buffer layer was grown at a rate of 10% Ge μm^{-1} with the CMP step, and this layer showed a final threading dislocation density an order of

magnitude lower than that of a 100% Ge graded buffer layer sample grown at a rate of the 5% Ge μm^{-1} with no CMP step.

2.2 Silicide technology

2.2.1 Introduction to silicides

In a silicon integrated circuit, isolated active-device regions are connected through specific electrical paths, employing high conductivity, thin film structures, fabricated above the SiO_2 insulator that covers the silicon surface. Whenever a connection is needed between a conducting film (metal) and an active region in a device (single crystal semiconductor), an opening in the SiO_2 must be provided to allow such contacts to occur. The metal and single crystal semiconductor substrate contact gives rise to a parasitic resistance component R_{CO}, which contributes to the overall parasitic series resistances that can exist in the path between the metal-to-Si substrate interface and the region where the actual transistor action begins. In metal oxide semiconductor field effect transistors (MOSFETs), R_{CO} is the contact resistance found between the metal and single crystal silicon source/drain region, while in bipolar transistors, R_{CO} can be found in the base, emitter and collector contacts. Therefore, R_{CO} is always one of the parasitic series resistance components whenever metal to semiconductor contacts are made. It is a macroscopic quantity that depends on the contact size, the semiconductor sheet resistance and the contact geometry as well as the specific contact resistivity, ρ_c. As semiconductor device dimensions shrink both vertically and laterally, device currents and current densities increase. Hence, if the metal to semiconductor contact area is also scaled, R_{CO} increases. This problem can be suppressed if there can be improvements to increase the

contact size while decreasing the sheet resistance of the semiconductor. Another equally important aspect for contact properties is to form ideal or near-ideal ohmic contacts between the metal and semiconductor interface. However when metal-to-semiconductor contacts are fabricated, they possess non-ohmic and rectifying characteristics, which are termed Schottky contacts. This type of contact can serve as diodes in some applications in integrated circuits but not as ohmic contacts to MOS or bipolar devices.

Silicides were found to be suitable ohmic contact materials to reduce the parasitic component of R_{CO}. These are compounds of metal and silicon (Si) atoms. In silicon integrated circuits (IC), refractory metal silicides have been implemented in devices to lower the sheet resistance and to form good ohmic contacts with the underlying highly doped Si active regions. They have been preferred to pure metals because of the stability of their contacts with Si, resistance to electromigration and their self-passivating nature by forming SiO_2 in an oxygen-rich environment. In addition, the reaction of the metal with Si but not with SiO_2 is an important factor in most device applications. This allows an alignment of the silicide with SiO_2-defined window edges giving rise to maximum contact area, which surpasses other patterning techniques such as lithography. They can also withstand the chemicals normally encountered during device fabrication processes. Most importantly, many metal silicides such as platinum, palladium, tungsten, molybdenum, titanium and other metals have reasonably good compatibility with conventional Si processing[6,7].

2.2.2 Formation of silicides for technological applications

The important applications[8] of silicides, and which are utilized currently in the multi-billion-semiconductor industry are:

- Polycrystalline silicon-silicide (Polycide): a well-designed polycide gate has four times less gate sheet resistance (~10 Ω/□) compared to a conventional polysilicon gate (~40 Ω/□). Figure 2.1 (a) illustrates such a process whereby (i) a local oxidation is performed to physically and electrically isolate a transistor area; (ii) a uniform layer of poly-Si (dotted) is deposited with a uniform layer of metal silicide layer formed above it (by the deposition of a metal layer followed by annealing); (iii) the MSi_2 and poly-Si structure is etched to expose areas for shallow junction formation; (iv) the formation of source and drain regions by doping and the formation of spacers.
- Self-aligned silicide (Salicide): A typical process whereby a layer of blanket metal is deposited on the entire transistor structure (normally after source and drain formation) and annealed. In Figure 2.1 (b), such a process is performed whereby (i) the gate region is formed with source and drain regions already defined as in Figure 2.1 (a) except that polycide is not formed on top of the gate; (ii) a metallic layer of Ti or Co is deposited uniformly on the surface of the wafer; (iii) annealing is done to form metal silicide at the interface where Si is exposed. In principle, silicides are formed only where the metal is in contact with the Si substrate (i.e. on top of the source, drain and gate); (iv) etch-back is done to remove those areas where silicides are absent to form a

salicide device whereby low resistivity contacts are present at source, drain and gate.

- Local interconnects: Short silicide wires that connect adjacent devices to make simple functional groups over a very short distance.

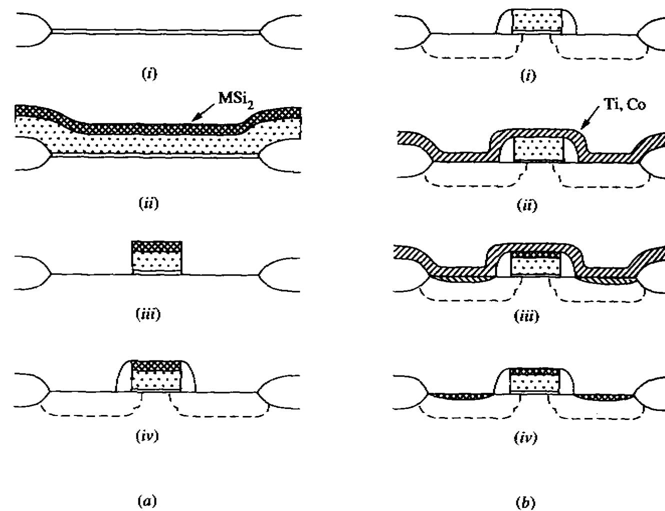

Figure 2.1 Polycide and Salicide processes: (a) Polycide structure, (b) Salicide structure.

Between polycide and salicide, the latter is more important for scaling of high-performance CMOS devices. They are used to lower sheet, series and contact resistances of gate and source/drain regions. By increasing device performance and lowering RC delays[9], salicide allow faster operation of devices. To investigate the application of salicide for deep-submicron technologies, we need to understand the fundamental materials aspects of controlling silicide phase formation and evolution. The most important silicides with good-aligning properties are NiSi, $CoSi_2$ and $TiSi_2$, and which the properties of each silicide will be discussed in the preceding sections.

Silicides can also be prepared in different ways. Traditionally, they were formed by annealing a thin-film metal-Si composite deposited in one of the following methods:

- Metal on Si or poly-Si: metal is deposited either by sputtering, evaporating or electroplating;
- Cosputtering metal and silicon on Si, poly-Si or oxide in the desired ratio from two independent targets;
- Cosputtering on Si, poly-Si, or oxide from a hot-pressed silicide target;
- Coevaporating on Si, poly-Si or oxide elements in a two-filament or double e-gun evaporator;
- Chemical vapor deposition (CVD), at atmospheric or lower pressures, of silicide on Si, poly-Si, or oxide.

2.2.3 Requirements for silicides in silicon integrated circuits

Due to the desired properties of silicides for ULSI applications, only a few metals emerge as suitable. They are titanium (Ti), cobalt (Co) and nickel (Ni) forming $TiSi_2$, $CoSi_2$ and NiSi respectively. The requirements are follows:

1. Low resistivity and low contact resistance
2. Easy to form
3. Easy to etch for pattern generation
4. High thermal stability for post-silicidation processing steps
5. High chemical and mechanical stability
6. Compatibility with salicide and Si processing
7. Good surface smoothness

8. Good device characteristics and lifetimes

9. Window contacts – Low contact resistance and minimal junction penetration

Besides fulfilling the requirements above, there are additional requirements that future silicides for ULSI technology needs. Table 2.1 lists some of the more important properties of future silicides according to the International Technology Roadmap for Semiconductor (ITRS) 2001.

Year of Production	**2002**	**2003**	**2004**	**2005**	**2007**
MPU/ASIC ½ pitch (nm)	*130*	*107*	*90*	*80*	*65*
Drain extension x_j (nm)	22-36	19-31	15-25	13-22	10-17
Contact x_j (nm)	39-78	33-66	27-45	24-47	18-37
Max. Si consumption (nm)	19-38	16-32	13-26	11-23	9-18
Silicide Thickness (nm)	29.2	24.8	20.4	17.6	13.8
Contact Silicide sheet Rs (Ω/□)	5.1	6.1	7.4	8.5	10.9
Contact max. Rs (Ω/cm^2)	3.20E-07	2.70E-07	2.10E-07	1.80E-07	1.10E-07

Table 2.1 ITRS 2001 update of relevant data concerning silicides

For window contacts for ULSI technology, the requirements are: (i) minimum Si consumption, (ii) low contact resistance and (iii) minimum junction penetration. As shown in Table 2.1, as the technology node decreases to 0.1μm and below, the Si consumption has to decrease, the contact sheet resistance will increase due to smaller contact areas so contact maximum resistivity has to decrease to accommodate, and

junction penetration has to decrease in order to avoid junction spiking. We will review the three important types of silicides in the next section and compare each one of them to see if they fit into the future ULSI requirements.

2.2.4 Comparison of nickel silicide with other silicides

There have been a number of excellent reviews by Tu[10] and Nicolet and Lau[11] on silicide formation. Murarka[12] and d'Heurle and Gas[13] reviewed silicide properties that affect very large scale integration (VLSI) technology implementations. Maex[14] provided an outstanding review on silicide device applications. Colgan[15] gave a detailed review of the formation and stability of silicides on polycrystalline Si and, together with Gambino; they evaluated the scientific and technological aspects of silicides and ohmic contacts[16]. In this section we give a detailed review for $TiSi_2$, $CoSi_2$ and NiSi as well as nickel silicidation on $Si_{1-x}Ge_x$ substrates.

2.2.4.1 Titanium disilicide ($TiSi_2$)

$TiSi_2$ is a polymorphic material and may exist as two different phases, i.e. C49 $TiSi_2$ and C54 $TiSi_2$. C49 $TiSi_2$ is metastable phase of orthorhombic structure and has a higher resistivity compared to orthorhombic face-centered C54 $TiSi_2$[17]. It was experimentally found that C49 $TiSi_2$ formed before C54 $TiSi_2$ during silicidation annealing and eventually transformed to stable phase C54 $TiSi_2$ at higher temperatures. The reactions can be summarized as:

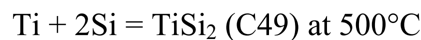

$$Ti + 2Si = TiSi_2\ (C49)\ \text{at}\ 500°C$$

$$TiSi_2\ (C49) = TiSi_2\ (C54)\ \text{at}\ 700°C$$

$TiSi_2$ is currently preferred for volume manufacturing in the semiconductor industry down to 0.25µm technologies. However, its scalability to deep-sub-micron technologies is facing difficulties, mainly in obtaining low sheet resistance on narrow gates with conventional processing[18,19,20]. The increase in sheet resistance with decreasing line width can be attributed to incomplete transformation from high resistivity $TiSi_2$ C49 to low resistivity $TiSi_2$ C54 phase. One way to reduce sheet resistance is by a high temperature anneal. The solutions brought about by innovations may bring about the extension of Ti-salicide processing by up to three generations at best. However, there are a few limitations. Firstly, smaller dimensions require the transition temperature of C49 to C54 phase to rise. However, junction scaling requires decreasing silicide thickness, which causes agglomeration at lower temperatures[21]. These mutually exclusive requirements put a severe test on the temperature window for the Ti-salicide process. Besides this, another obstacle facing the introduction of such novel solutions mentioned in this section is the complexity in implementing them in foundry manufacturing.

Another limit for $TiSi_2$ is the bridging failure caused by the phenomenon known as creep up[22]. Silicidation of $TiSi_2$ proceeds by the mechanism where the dominant diffusing species is the Si atom. This movement of Si atoms into the metal film causes silicidation to occur in the sidewall in MOSFET gate structures. The possibility of silicide bridges forming between the gate and source or drain causes a short in the device.

2.2.4.2 Cobalt disilicide ($CoSi_2$)

The reactions of Co with Si to form $CoSi_2$ follow the steps below:

$$2Co + Si = Co_2Si \qquad (250°C)$$

$$Co_2Si + Si = 2CoSi \quad (450°C)$$

$$CoSi + Si = CoSi_2 \quad (650°C)$$

The main choice for replacing Ti salicide from and below 0.18μm technologies is $CoSi_2$. Unlike $TiSi_2$, $CoSi_2$ has no line width limit problem (because its phase is independent of dimension) and can be scaled to the nanometer-level[23]. Moreover, $CoSi_2$ tends to form thicker films at the edge of gate structures. This can result in a slight reverse line width effect, whereby the sheet resistance decreases as the geometry shrinks. From an application point of view, a decrease in sheet resistance is favorable. However, the uniformity of films is uneven from this point and will affect subsequent layers of material that are deposited further down the processing steps.

Many levels of research are geared towards nanoscale production of cobalt salicide. However, despite the various advantages $CoSi_2$ brings to silicidation, there are still problems to overcome before mass production with high yield is possible. The rest of this section will give a brief summary of these problems and the methods available to address them.

Detavernier et al.[24] showed that $CoSi_2$ is sensitive to oxygen contamination due to the formation of a SiO_x diffusion barrier between CoSi and the unreacted Co. In $TiSi_2$, oxygen contamination is less critical due to the reducing nature of Ti. By using a Ti cap in $CoSi_2$ formation, any unreacted Co will be protected from oxygen contamination (that may be present in the ambient) and thus prevents oxidation of Co. Ti acts as a reducing agent for any SiO_x barrier that maybe present between the reaction interfaces due to ineffective cleaning. Another role of Ti is that it getters oxygen that was incorporated into

the Co film during deposition. In addition, Goto et al.[25] used a TiN capping to prevent oxidation of the Co layer and obtained a smooth $CoSi_2$ film in a salicide process.

Besides oxygen contamination, $CoSi_2$ suffers from diode leakage problems on shallow junctions. This is due to the formation of polycrystalline $CoSi_2$ whereby a smooth interface is hard to achieve and junction spiking is a recurring problem[26,27]. Kittl *et al.* presented an overview of Ti and Co salicide developments[28] and discussed the materials issues that control the scalability of Ti and Co silicides for deep sub-micron CMOS. Some of the ways in which diode leakage can be prevented include (i) use of a sputter clean step to reduce contaminants at the reaction interface; (ii) use of a higher temperature rapid thermal annealing (RTA) step that reduces diode leakage in proportion to higher temperatures (higher temperature will lead to the dissolution of spikes and hence an improvement in $CoSi_2$-Si interface roughness); and (iii) prolonged annealing after complete silicide formation. However silicide agglomeration, and degradation of source-drain series resistance set an upper limit for the RTA thermal budget.

Thermal stability is another important factor[29] for consideration as processes are scaled down to the deep sub-micron range. Gate oxide integrity (GOI) is a concern for Co salicide since Co contamination degrades GOI and Co diffusivities and solubilities in Si are high (significantly higher than those of Ti) at high temperatures. Degradation of film and interface morphology at high temperatures, as well as process conditions that induce rough non-uniform silicide-Si interfaces, can affect GOI, which can be avoided by a careful control of the thermal history of silicidation.

In summary, some of the challenges facing the use of cobalt silicide in the semiconductor industry for sub-0.1μm manufacturing are: (i) Co is sensitive to oxygen

contamination especially for narrower line widths, (ii) Co processes are very sensitive to surface conditions and cleaning steps are very important, (iii) higher junction leakage from Co spikes and (iv) thermal stability and dopant diffusion leading to concerns with GOI at high temperature processing steps.

2.2.4.3 Nickel monosilicide (NiSi)

The silicidation process of Ni on Si substrates has been well established in the literature[11,12]. They are produced by depositing rather thick (>30 nm) Ni films on (111) or (100) Si wafers followed by annealing at different temperatures. The reactions of Ni with Si go through the following steps:

$$2Ni + Si = Ni_2Si \quad (250°C)$$

$$Ni_2Si + Si = 2NiSi \quad (300°C)$$

$$NiSi + Si = NiSi_2 \quad (750\text{-}800°C)$$

Ni reacts with Si substrates at about 250°C to form Ni_2Si, which is a diffusion-controlled mechanism with activation energy of approximately 1.5eV.[30] At temperatures higher than about 300°C, NiSi has been observed to grow by a diffusion-controlled mechanism as well; Ni atoms diffuse through the growing NiSi layer with activation energy of about 1.65eV. In addition, the NiSi layers tend to grow faster on (100) silicon than on (111) silicon.[31] The monosilicide phase has the lowest resistivity among the Ni silicides and therefore it is desirable for device fabrication. NiSi has an orthorhombic structure with lattice parameters a = 0.518nm, b = 0.334nm, and c = 0.562nm, and space group P*nma*. NiSi is stable on Si substrates up to 750-800°C, where $NiSi_2$ forms by consuming more Si.[32] The formation of the disilicide phase is nucleation

controlled and it can be grown epitaxially on (100) and (111) silicon.[33] This is due to the fact that $NiSi_2$ has a cubic CaF_2 structure with a lattice parameter a = 0.5406nm, which has a small lattice mismatch of 0.4% compared with silicon at room temperature. In earlier works[34,35], it has been shown that $NiSi_2$ can grow epitaxially on a silicon (100) substrate at temperatures as low as 220-280°C, with a thin silicon dioxide layer between the nickel and substrate layers. Markers experiments[36] have shown that in all the three nickel silicide phases mentioned, at their temperature of formation, the diffusion coefficients for nickel atoms are at least ten times greater than the corresponding coefficients for the silicon atoms, so that all three silicides can be said to form through metal motion.

As mentioned, the monosilicide phase has the lowest resistivity among the Ni silicides and therefore it is the most desirable silicide phase for device fabrication. Table 2.2 compares the properties of NiSi with $TiSi_2$ and $CoSi_2$ and shows the number of advantages[22,37] NiSi. First, silicidation of NiSi can be accomplished at a single annealing step with a wider temperature window at lower temperature (350-750°C), when compared to $TiSi_2$ and $NiSi_2$. Secondly, NiSi consumes less Si during silicidation which is an important aspect for the formation of shallow source and drain junctions in deep submicron CMOS. In addition the NiSi has the ability to maintain low resistivity even for line widths down to 0.1μm[35,37]. The salicide process for NiSi is controlled by a mechanism where the metal atoms are the dominant diffusing species. This prevents the creep up mechanism, which forms bridging silicides between the gate and source or drain, shorting the device.

Property	$CoSi_2$	NiSi	$TiSi_2$
Thin Film Resistivity (Ωμ-cm)	14-20	14-20	13-20
Si consumption in terms of thickness of metal layer deposited	3.6	1.8	2.3
Form. Temp. RTA1 (°C) RTA2	400-450 700-800	300-750	625-675 850-900
Melting Temp. (°C)	1326	992	1500
Eutectic Temp. (°C)	1204	964	1330
Schottky Ht. for electrons (eV)	0.65	0.67	0.6
Schottky Ht. for holes (eV)	0.45	0.43	0.49
Diffusing Species	Co, for $CoSi_2$ Si, for CoSi	Ni	Si
Film stress (dyn/cm^2)	1.2×10^{10}	1.5×10^{10}	6×10^{9}

Table 2.2 Comparison of physical properties of $TiSi_2$, $CoSi_2$ and NiSi.

One of the major challenges for NiSi in Si device application is its relatively poor thermal stability beyond 700°C that leads to the formation of the higher resistivity disilicide phase. In addition, there is an increasing tendency for NiSi to agglomerate at temperatures as low as 600°C, which is a concern for the back-end CMOS process[38]. Silicide on polycrystalline structures is more vulnerable to thermal degradation than silicide on single crystalline Si. On poly-Si, layer inversion (inversion of the position of the silicide and the poly-Si due to poly-Si grain growth) was reported to start at 550ºC[39]. The driving force for layer inversion to occur has been attributed to poly-Si grain growth in order to reduce the grain boundaries.

To overcome these problems, there have been efforts to enhance the phase stability and thermal stability of NiSi in order to widen the silicidation temperature-processing window and to allow a larger backend processing thermal budget. It was found that alloying Ni with Pt on both Si (100) and Si (111) increases the temperature of agglomeration of the monosilicide layer to above 800ºC and retards the formation temperature of $NiSi_2$ to above 900ºC.[40] The poly-inversion and $NiSi_2$ were also suppressed to elevated temperatures with alloying of the NiSi layer on poly Si.[41] In addition, it has been recently shown that high-dose BF_2^+-implanted Si (001) significantly enhances the thermal stability of NiSi. The presence of fluorine dramatically reduced the NiSi/Si(100) interface roughness while increasing the $NiSi_2$ nucleation temperature.[42]

2.2.4.4 Nickel silicidation on $Si_{1-x}Ge_x$ substrates

The importance of the application of $Si_{1-x}Ge_x$ in Si-based devices was highlighted in section 2.1. One of the important requirements for device application is the formation of ohmic or rectifying contacts using the salicide process. As a result, the thermally induced interfacial reaction between metal/ $Si_{1-x}Ge_x$ has been studied for Pt[43,44], Pd, Co[45,46,47,48], Ti[48,49,50] and Ni[51,52,53,54]. Various degrees of germanium segregation or formation of segregated layered structures were observed in the reactions of these metal/ $Si_{1-x}Ge_x$ systems. The difference of heat of formation of silicide and germanide offers the driving force for the segregation of Ge rich Si-Ge alloys.

Many silicides of Ni share similar crystallographic structures and have close lattice parameters with their counterpart germanides. For example NiSi and NiGe have the same orthorhombic structure and therefore should form a solid solution. Previous

studies[51,52,53] indicated the formation of a ternary alloy monogermanosilicide $Ni(Si_{1-x}Ge_x)$ when a thin layer of Ni (≤30nm) deposited on $Si_{1-x}Ge_x$ substrates is annealed to temperatures of 300-400°C. The reaction is mainly diffusion controlled with Ge and Ni as the dominant diffusing species. Above 500°C, Ge segregation to the grain boundaries was observed, this resulted in the formation of Ge-rich $Si_{1-z}Ge_z$ grains sandwiched in between Ge-deficient $Ni(Si_{1-u}Ge_u)$ islands, where $u<x<z$.[52,54]. The monosilicide film became discontinuous at 700°C, which suggests the onset of agglomeration. Since Ge acts as a dominant diffuser during annealing, it seemed that Ge segregation enhanced the agglomeration of the monogermanosilicide film. The $NiSi_2$ or $Ni(Si\text{-}Ge)_2$ were not observed even at annealing temperatures of 900°C.

2.3 Principles of thin films

In the first part of this section, the principles of thin film formation of the different nickel silicide phases will be reviewed. For a thermal reaction between a Ni film and Si (100), there are two different reaction-controlled mechanisms, namely diffusion-controlled and nucleation-controlled, governing the formation of the silicide phases. The principles outlined would be heavily borrowed from ideas developed by d'Heurle *et al.* (Ref. 31 and 33). We will then explore the theory behind agglomeration of thin films and the kinetics embedded in this phenomenon.

2.3.1 Mechanism for the formation of thin film nickel silicide phases

When two solids, in our case Ni and Si, in contact with each other interact to form a new phase Ni-Si, the rate-controlling mechanism is diffusion controlled if the new phase grows linearly as a function of the square root of time. The Arrhenius relation as is shown in equation 2.1 can express the rate of reaction by this mechanism as function of temperature according to an activation energy.

$$\text{Rate of reaction} = Ce^{-Q/RT} \tag{2.1}$$

where Q = activation energy, J/mol or cal/mol
R = molar gas constant, 8.314 J/ (mol. K)
T = temperature, K
C = rate constant, independent of temperature

Equation 2.1 can be rewritten in the natural logarithmic form as:

$$\text{Ln rate} = \text{Ln constant} - \frac{Q}{RT} \tag{2.2}$$

The value of the gradient of slop of the plot of Ln rate against 1/T will give the activation energy of the diffusion-controlled reaction. As mentioned in the literature, the mobility of Ni atoms is substantially faster than that of Si atoms, during a reaction at the Ni/Si interface. Therefore the diffusion of Ni atoms into the Si substrate can be expressed as a solution to Fick's second law given by equation 2.3,

$$\frac{C_s - C_x}{C_s - C_o} = erf\left(\frac{x}{2\sqrt{Dt}}\right) \tag{2.3}$$

where C_s = surface concentration of Ni diffusing into Si
C_o = initial uniform concentration of element in solid
C_x = concentration of element at distance x from surface at time t
x = distance from surface
D = diffusivity of Ni in Si
t = time

Rewriting equation 2.3 gives the linear relation between the square of the thickness of the nickel silicide and time

$$x^2 = erf^{-1}\left(\frac{C_s - C_x}{C_s - C_o}\right)4Dt \qquad (2.4)$$

$$\Rightarrow \qquad x^2 \propto t$$

Using the theory discussed above, NiSi and Ni_2Si were determined to grow by the diffusion-controlled mechanism by d'Heurle *et al.*, with activation energies of about 1.7 and 1.5 eV respectively.

Nucleation-controlled reactions between two solids in contact are characterized by an instantaneous reaction, which occurs at a critical temperature, the new phase is non-planar or discontinuous, and a high temperature reaction that excludes diffusion as a rate controlling mechanism. This point is completely valid only with thin films in general. For thicker films, nucleation occurs first and is followed by diffusion-controlled growth. In order to understand the mechanism of nucleation, the classical theory of nucleation must first be visited. Nucleation of crystalline phase consists of the formation of a nucleus of a size large enough for grain growth. The lowering of free energy of the system, ΔG, drives the nucleation process. However, the growth of the nucleus will be opposed by any larger interfacial area with a specific surface energy, σ. The calculated ΔG_1 per unit volume of a system to an average nucleus radius, r, will give a free energy of

$$\Delta G = br^2\sigma - ar^3\Delta G_1 \qquad (2.5)$$

where a and b are geometrical terms that take account the fact that if the nucleus is a crystal, it will generally not be spherical because of its anisotropic characteristics.

The maximum of ΔG gives a critical radius r^* of the nucleus where nuclei of size larger than r^* will tend to grow while smaller nuclei will dissolve. The critical size of the nucleus can be given by:

$$r^* = \frac{2b\sigma}{3a\Delta G_1} \quad (2.6)$$

The free energy of the critical nuclei at any temperature T becomes:

$$\Delta G^* = \frac{4b^3\sigma^3 T_c^2}{27a^2\Delta H^2 (T - T_c)^2} \quad (2.7)$$

At that temperature, the rate of nucleation ρ^* can be presented to be proportional to the concentration of critical nuclei and to the rate at which such nuclei can form,

$$\rho^* = K\, e^{(-\Delta G^*/kT)}\, e^{(-Q/kT)} \quad (2.8)$$

where $e^{-Q/kT}$ is a diffusion term and K is a proportionality factor.

Above the equilibrium point, where the activation energy for the rate of nucleation surpasses the one obtained for diffusion, it can be shown from equation 2.6 and 2.7 that the rate of nucleation will vary approximately as $e^{-(1/T)}$. This implies that the nucleation process occurs within a narrow temperature range at a very fast rate, meaning that it is not possible to carry out experimental observations of the kinetics.

According to the derivation of equation 2.7, it can be shown that

$$\Delta G^* \propto \Delta\sigma^3 / \Delta G_1^2 \quad (2.9)$$

ΔG^* becomes large, when ΔG_1 is small. One can anticipate that ΔH, the enthalpy change of transition, will be small when ΔG_1 is small. Although there is a distinction between the two quantities, the relation between them follows the same trend. Therefore a reaction will be nucleation-controlled when the system is driven by a small ΔG_1 or ΔH

where a slow nucleation rate will occur accompanied simultaneously by an increase in surface energy.

In the case of the formation of Ni_2Si and NiSi, the ΔG_1 value is rather large with $\Delta\sigma$ relatively small, which suggests that the nucleation effects in their formation should be negligible. Since $NiSi_2$ grows epitaxially on Si substrates, the calculated values ΔG_1 and $\Delta\sigma$ for the formation of $NiSi_2$ from NiSi and Si are low, even at high temperatures. Therefore, the difficulty in nucleation to form $NiSi_2$ results primarily from the physical effects of the reaction between NiSi and Si. This can be explained by the fact that when $NiSi_2$ forms from NiSi and silicon, there is a total volume decrease of about 12%. The change in volume during the nucleation would introduce an additional consideration in the form of elastic stresses. It has been shown that the elastic interaction is not likely to be negligible, and the rate-controlling nucleation for $NiSi_2$ is actually imposed by the decrease in enthalpy due to elastic stresses. However, if one is able to form $NiSi_2$ directly from the direct reaction of Ni with Si instead of NiSi with Si, the change in free energy for this reaction would be proportional to $\Delta G_1(NiSi_2)$ and ΔG^* would be much smaller, so that the reaction would cease to be nucleation-controlled.

2.3.2 Agglomeration of thin films

Models[55,56] proposed for the agglomeration of thin films suggest a two-step process; void formation and void growth. In the first step, it is known that grooves form at grain boundaries of a polycrystalline thin film at high temperatures due to the process of thermal grooving.[57] The grooving process occurs to maintain a energy balance

between the two surface energies and the one grain boundary energy at the grain boundaries as shown in equation 2.9.

$$\gamma_b = 2\gamma_s \sin\theta \tag{2.10}$$

From the conditions stated, there is an equilibrium angle needed to be established to reach local equilibrium. Diffusion of atoms away from the regions of high curvature will continue until the groove reaches the substrate where a constant curvature surface (equilibrium angle) is reached. At this stage a stable void is formed in the film. The second step, which involves the growth of the void, is driven by the reduction of the curvature created in the film edge profile. The film becomes discontinuous when the voids and the islands of the material are formed.

From equilibrium calculations, it can be shown that agglomeration should depend on the ratio (L_c/X) where L_c is the critical grain size and X is the film thickness. By decreasing the grain size or increasing the film thickness this will decrease the ratio, which will prevent agglomeration. In addition, prevention of surface grooving by decreasing grain boundary energies or raising surface energies, can also in turn suppress the agglomeration process.

References:

[1] I. Rin, *III-V Review* **8(4)**, (1995), 20.
[2] D.J. Paul, *Advanced Material* **11(3)**, (1999), 191.
[3] M.T. Currie, C.W. Leitz, T.A. Langdo, G. Taraschi, E.A. Fitzgerald and D.A. Antoniadis, *J. Vac. Sci. Technol. B* **19(6)**, (2001), 2268.
[4] C.W. Leitz, M.T. Currie, M.L. Lee, Z-Y. Cheng, D.A. Antoniadis and E.A. Fitzgerald, *J. Appl. Phys.* **92(7)**, (2002), 3745.
[5] M.T. Curie, S.B. Samavedam, T.A. Langdo, C.W. Leitz and E.A. Fitzgerald, *Appl. Phys. Lett*. **72**, (1998), 1718.
[6] Karen Maex and Marc Van Rossum, *Properties of Metal Silicides*, Institution of Electrical Engineers, UK, (1995), Chapt. 2.
[7] K. Maex, *Mater. Sci. Eng.* **R11**, (1993), 53.
[8] C.Y. Chang and S.M. Sze, *ULSI Technology*, McGraw-Hill, (1996), Chapt. 4.
[9] A.R. Chapman, C.C. Wei, D.A. Bell, S. Aur, G.A. Brown, R.A. Haken, *IEDM Tech. Digest,* (1991), 489.
[10] K.N. Tu, J.W. Mayer and J.M. Poate, *Interdiffusion and Reactions,* Wiley, New York, (1978), Chapt. 10.
[11] M.A. Nicolet and S.S. Lau, *VLSI Electronics: Microstructure Science,* Vol. 6, Academic Press, New York, (1983), Chapt. 6.
[12] S.P Murarka, *Silicides for VLSI Applications,* Academic, New York, (1983), Chapt. 3.
[13] F.M. d'Heurle and P. Gas, *J. Mater. Res.* **1**, (1986), 205.
[14] K. Maex, *Mater. Sci. Eng.* **R11**, (1993), 53.
[15] E.G. Colgan, J.P. Gambino and Q.Z. Hong, *Mater. Sci. Eng.* **R16**, (1996), 43.
[16] J.P. Gambino and E.G. Colgan, *Materials Chemistry and Physics* **52,** (1998), 99.
[17] R.V. Nagabushnam, S. Sharan, G. Sandhu, V.R. Rakesh, R.K. Singh and P. Tiwari, *MRS symposium proceedings* **402,** (1996), 113.
[18] J.B. Lasky, J.S. Nakos, O.J. Cain and P.J. Geiss, *IEEE Trans. Electron Devices* **ED-38,** (1991), 262.
[19] R.A. Roy, L.A. Clevenger, C. Cabral Jr., K.L. Saenger, S. Biauer, J. Jordan-Sweet, J. Bucchignano and O.B. Stephenson, *Appl. Phys. Lett.* **66,** (1995), 1732.
[20] J.A. Kitti, D.A. Prinslow, P.P. Apte and M.F. Pas, *Appl. Phys. Lett.* **67,** (1995), 2308.
[21] T.P. Nolan and R. Sinclair, *J. Appl. Phys.* **71,** (1992), 720.
[22] T. Moimoto, T. Ohguro, H.S. Momose, T. Ilinuma, I. Kunishima, K. Suguro, I. Ktakabe, H. Nakajima, M. Tsuchiaki, M. Ono, Y. Katsumata and H. Imai, *IEEE Transaction on Electron Devices* **42(5)**, (1995), 915.
[23] K. Maex, *Semi. International* **18(3),** (1995), 75.
[24] C. Detavernier, R.L. Van Meirhaeghe, F. Cardon, R.A. Donaton and K. Maex, *Microelectronic Engineering* **50,** (2000), 125.
[25] K. Goto, T. Yamazaki, A. Fushida, S. Inagaki and H. Yagi, *Symp. VLSI Technol. Dig. Tech. Papers*, IEEE New York, (1994), 119.
[26] K. Goto, A. Fushida, J. Watanabe, T. Sukegawa, K. Kawamura, T. Yamazaki and T. Sugii, *IEDM Tech. Digest,* (1995), 449.
[27] J.Y. Dai, Z.R. Guo, S.F. Tee, C.L. Tay, Eddie Er and S. Redkar, *Appl. Phys. Lett.* **78(20)**, (2001), 3091.

[28] J.A. Kittl, Q.Z. Hong, *Thin Solid Films* **320**, (1998), 110.
[29] A. Alberti, F. La Via, S. Ravesi, E. Rimini, *Microelectronic Engineering* **50**, (2000), 179.
[30] J.O. Olowolafe, M.A. Nicolet and J.W. Mayer, *Thin Solid Films* **38**, (1976), 143.
[31] F.M. d'Heurle, C.S Petersson, J.E.E Badlin, S.J. La Placa and C.Y Wong, *J. Appl. Phys.* **55**, (1984), 4208.
[32] S.S. Lau and N.W. Cheung, *Thin Solid Films* **71**, (1980), 117.
[33] F.M. d'Heurle, *J. Mater. Res.* **3(1)**, (1988), 167.
[34] L.J. Chen, C.M. Doland, I.W. Wu, J.J. Chu and S.W. Liu, *J. Appl. Phys.* **62**, (1987), 2789.
[35] V. Teodorescu, L. Nistor, H. Bender, A. Sttgen, A. Lauwers, K. Maex and J. Van Landuyt, *J. Appl. Phys.* **90(1)**, (2001), 167.
[36] F. d'Heurle, S. Petersson, L. Stolt and B. Strizker, *J. Appl. Phys.* **53(8)**, (1982), 5678.
[37] T. Ohguro *et al.*, *IEEE Trans. Electron Devices* **41**, (1994), 2305.
[38] R. Mukai, S. Ozawa and H. Yagi, *Thin Solid Films* **270**, (1995), 567.
[39] S. Nygren, D. Caffin, M. Ostling and F.M. d'Heurle, *Appl. Surf. Sci.* **53**, (1991), 87.
[40] D. Mangelinck, J.Y. Dai, J.S. Pan and S.K. Lahiri, *Appl. Phys. Lett.* **75(12)**, (1999), 1736.
[41] P.S Lee, D. Mangelinck, K.L Pey, J. Ding, D.Z. Chi, T. Osipowicz, J.Y. Dai and A. See, *Microelectronic Engineering* **60**, (2002), 171.
[42] A.S.W. Wong, D.Z. Chi, M. Loomans, D. Ma, M.Y. Lai, W.C. Tjiu, S.J. Chua, C.W. Lim and J.E. Greene, *Appl. Phys. Lett.* **81(27)**, (2002), 5138.
[43] Q.Z. Hong, J.W. Mayer, *J. Appl. Phys.* **66**, (1989), 611.
[44] H.K. Liou, X. Wu, U. Gennser, *Appl. Phys. Lett.* **60**, (1992), 577.
[45] R.A. Donaton, K. Maex, A. Vantomme, G. Langouche, Y. Morciaux, A. St. Amour and J.C. Sturm, *Appl. Phys. Lett.* **70(10)**, (1997), 1266.
[46] B.I. Boyanov, P.T. Goeller, D.E. Sayers and R.J. Nemanich, *J. Appl. Phys.* **84(8)**, (1998), 4285.
[47] C. Detavernier, T.R.L. Van Meirhaeghe, F. Cardon and K. Maex, *Thin Solid Films* **384**, (2001), 243.
[48] L.J. Chen, J.B. Lai, C.S. Lee, *Micron* **33**, (2002), 535.
[49] D.B. Aldrich, Y.L. Chen, D.E. Sayers, R.J. Nemanich, S.P. Ashburn and M.C. Ozturk, *J. Appl. Phys.* **77(10)**, (1995), 5107.
[50] D.B Aldrich, F.M. d'Heurle, D.E. Sayers and R.J. Nemanich, *Physical Review B* **53(24)**, (1996), 16279.
[51] R.D. Thompson, K.N. Tu, J. Angillelo, S. Delage and S.S Iyer, *J. Electrochem. Soc.* **135**, (1988), 3161.
[52] J.S. Luo, W.T. Lin, C.Y. Chang and P.S. Shih, *Nucl. Instr. and Meth. in Phys. Res. B* **169**, (2000), 124.
[53] H.B. Zhao, K.L. Pey, W.K. Choi, S. Chatto, E.A. Fitzgerald, D.A. Antoniadis, P.S. Lee, *J. Appl. Phys.* **92(1)**, (2002), 214.
[54] K.L. Pey, W.K. Choi, S. Chattopadhyay, H.B. Zhao, E.A. Fitzgerlad, D.A. Antoniadis and P.S. Lee, *J. Vac. Sci. Technol. A* **20(6)**, (2002), 1903.
[55] E. Jiran and C.V Thompson, *J. Electron. Mat.* **19(11)**, (1990), 1153.
[56] T.P. Nolan, R. Sinclair and R. Beyers, *J. Appl. Phys.* **71(2)**, (1992), 720.

[57] W.W. Mullins, *J. Appl. Phys.* **28(3)**, (1957), 333.

Chapter 3 Principles of transmission electron microscopy

3.1 Introduction to transmission electron microscopy

Electron microscopy can be seen to be superior in a number of ways to conventional visible light microscopy[1]. This is primarily due to the shorter wavelength of electrons compared to visible light photons, giving the possibility of much higher diffraction-limited spatial resolution. Wavelengths associated with electron beams suggest that resolving powers on the order of 10^{-3} nm should be possible, but other factors limit the resolving power of electron microscopes to levels currently approaching 0.1nm. Secondly, small-limiting apertures in the lenses found in electron microscopes increase the depth of field to the order of metres at the viewing screen compared to light microscopes, whereby the height difference of more than the wavelength of the light source present on the sample surface will not appear focused at the same time. Furthermore, the many complex interactions of a high-energy electron beam with the sample give rise to very useful analytical signals, giving quantitative information about the specimen composition and crystallographic structure. This is not the case for the visible light microscope.

Electron microscopes can be classified into two major groups: scanning electron microscopes (SEM) and transmission electron microscopes (TEM). For this study we will only concentrate on TEM, which is the primary analytical tool. The best way of understanding how a TEM works is to use the analogy of a slide projector. A slide projector consists of a light source (a very bright lamp) and a lens (called a condenser

lens), which focuses as much as possible of the light from the lamp onto the slide. The light then passes through the slide onto a second lens (objective lens), which forms an enlarged image of the slide on a screen. Similarly for a TEM, it starts with a source of electrons (the "lamp"). The electron beam is condensed onto the specimen (the "slide") by a condenser lens. Behind the specimen is the objective lens, which focuses and magnifies the image onto a viewing (fluorescent) screen. However this very basic description eludes several important aspects needed to understand the principle and design of the TEM. Most importantly to be taken in consideration for discussion in this chapter is the interaction of electrons with a thin foil specimen which is what makes transmission electron microscopy possible, that is, the formation of contrast in electron images and diffraction patterns. However the discussion will be limited to the background necessary to understand the information present in the experimental sections.

3.2 Important electron interactions with the sample in TEM

The energetic electrons in the TEM strike the sample and various reactions can occur as shown in Figure 3.1. Interactions of interest in this project are those transmitted through a thin electron transparent sample. We now briefly describe the interactions[2,3] and their relevance to this study. Their effects were apparent in the TEM images obtained during the course of our experiments, and a considerable amount of electron optical/analytical information can be gained by the use of appropriate detectors and display equipment. These observations and analysis will be noted in the discussion section.

Unscattered electrons

Source

Incident electrons, which are transmitted through the thin specimen without any interaction occurring inside the specimen.

Utilisation

The transmission of unscattered electrons is inversely proportional to the specimen thickness. Areas of the specimen that are thicker will have fewer transmitted unscattered electrons and so will appear darker, conversely the thinner areas will have more transmitted electrons and thus will appear lighter.

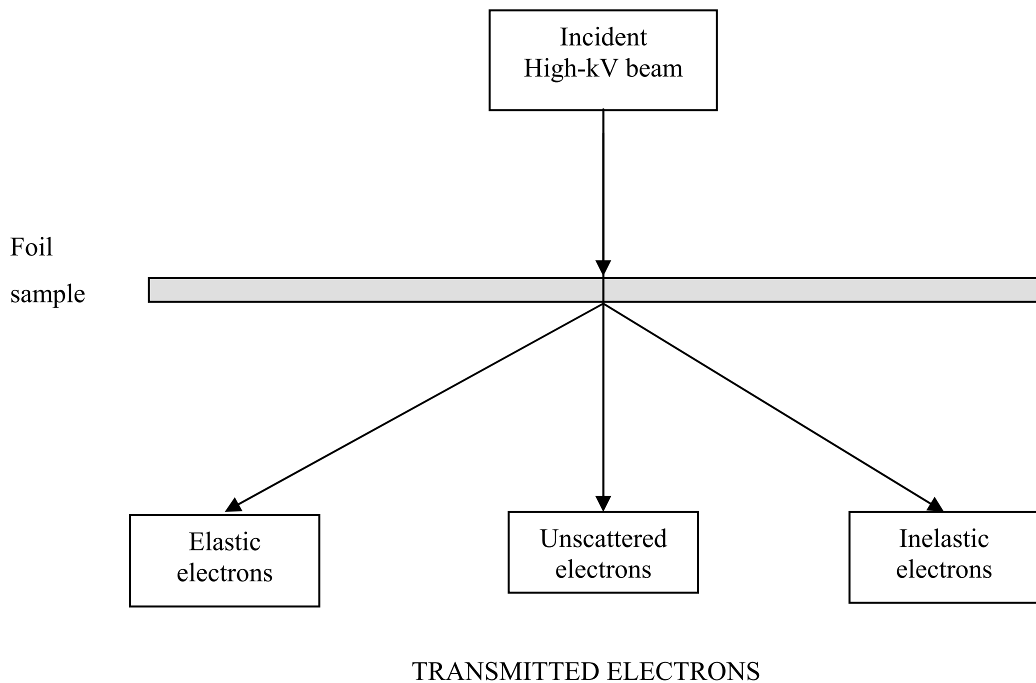

Figure 3.1 Diagrammatic representation of the interaction between a beam of high-energy incident electrons and a specimen. A number of interactions take place. Transmission electron microscopy (TEM) uses unscattered, inelastically scattered, and narrow-angle elastically scattered electrons.

Elastically scattered electrons

Source

Incident electrons that are scattered (deflected from their original path) by atoms in the specimen in an elastic fashion (no loss of energy). These scattered electrons are then transmitted through the remaining portions of the specimen.

Utilisation

Electrons obey Bragg's Law and thus are scattered according to Wavelength=2*distance between the diffracting atomic planes in the specimen*sine (angle of scattering). All incident electrons have approximately the same energy (thus wavelength) and enter the specimen normal to its surface. All incident electrons that are scattered by the same atomic spacing will be scattered by the same angle. These "similar angle" scattered electrons can be collated using magnetic lenses to form a pattern of spots; each spot corresponding to a specific atomic spacing (a plane). This is called a diffraction pattern, which can then yield information about the orientation, atomic arrangements and phases present in the area being examined.

Inelastically scattered electrons

Source

Incident electrons that interact with specimen atoms in an inelastic fashion, losing energy during the interaction. These electrons are then transmitted through the rest of the specimen.

Utilisation

Inelastically scattered electrons can be utilised two ways

- Electron Energy Loss Spectroscopy (EELS): the inelastic loss of energy by the incident electrons is characteristic of the elements that were interacted with. These energies are unique to each bonding state of each element and

thus can be used to extract both compositional and bonding (i.e. oxidation state) information on the specimen region being examined.

- Energy Filtered TEM: The element characteristic inelastic scattered electrons that are selected by a energy-selecting slit can be used to form an energy-selected version of the TEM image to form element maps

3.3 Diffraction

The preceding section has clearly demonstrated the duality of the particle-wave properties of electrons, whereby a high energy beam of electrons that is transmitted through a thin foil can either be inelastically scattered like a particle or undergo diffraction (elastically scattered), which is a wave nature. For this section, the theoretical basis for understanding electron diffraction, which is an indispensable part of TEM, will be discussed. In order to develop this understanding, the concepts of reciprocal lattice, Bragg Law and Eswald sphere is reviewed.

3.3.1 Theory of electron diffraction

In the field of diffraction[4,5], one must think of any crystal as having two lattices, the real lattice and the reciprocal lattice. To illustrate this point, let us define any real lattice vector using vectors **a**, **b** and **c** which are also unit-cell lattice constants in real space. Similarly, any reciprocal lattice vector can be defined by vectors **a***, **b*** and **c***. These vectors can be defined by the relations

$$a^*.\mathbf{b} = \mathbf{a}^*.\mathbf{c} = \mathbf{b}^*.\mathbf{a} = \mathbf{b}^*.\mathbf{c} = \mathbf{c}^*.\mathbf{a} = \mathbf{c}^*.\mathbf{b} = 0 \qquad (3.1)$$

which implies that **a*** is normal to both **b** and **c**. We also define that

$$a^* = \frac{b \wedge c}{V_c},\ b^* = \frac{c \wedge a}{V_c},\ c^* = \frac{a \wedge b}{V_c} \tag{3.2}$$

where V_c is the volume of unit cell, which is given by $\mathbf{a} \bullet \mathbf{b} \wedge \mathbf{c}$

Therefore the reciprocal lattice is so called because all lengths are in reciprocal units with respect to the real space lattice. Infinite crystal lattice planes in real space are represented by points in reciprocal space. In contrast, TEM specimens where crystals have to be thin enough for electrons to transmit through in real space are represented as rods in reciprocal space or relrods. Understanding the concept of reciprocal lattice, we next define an important reciprocal lattice vector $\mathbf{g}_{hkl}$, which is defined as

$$\mathbf{g}_{hkl} = h\,\mathbf{a}^* + k\,\mathbf{b}^* + l\,\mathbf{c}^* \tag{3.3}$$

where *h*, *k* and *l* are integers, and are the Miller indices of a plane. Considering that all the vectors in the (*hkl*) plane are normal to the vector, the unit vector, n, parallel to g is $\frac{g}{|g|}$. Therefore the shortest distance from the origin O can be given by:

$$n \bullet \frac{a}{h} = \frac{g}{|g|} \bullet \frac{a}{h} = \frac{(ha^* + kb^* + lc^*)}{|g|} \bullet \frac{a}{h} = \frac{1}{|g|} \tag{3.4}$$

Since the origin O always lies on a plane of this family of planes, the distance between parallel (*hkl*) planes can be given by:

$$d_{hkl} = \frac{1}{|g|} \tag{3.5}$$

We will now discuss the elastic scattering of an electron wave when it interacts with an atom in a unit cell (that is with an origin) in the far field. Plane wavefronts will only be considered, that is the wave is flat and k is normal to this wavefront as shown. The diagram defines the incident vector $\mathbf{k_I}$, the diffracted vector $\mathbf{k_D}$ and **K**. From the Figure 3.2 we find a definition for the difference vector, **K**:

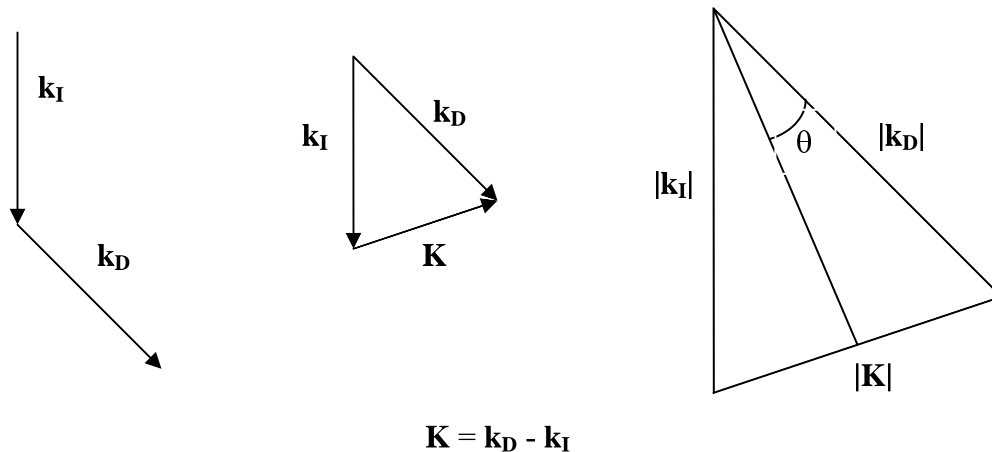

Figure 3.2 Defining the incident and diffracted vectors. **K** represents difference between incident ($\mathbf{k_I}$) and ($\mathbf{k_D}$) wave vectors.

Provided that the electron wave undergoes elastic scattering, we can define $|\mathbf{k_I}| = |\mathbf{k_D}| = |\mathbf{K}| = 1/\lambda$. Using simple trigonometry we define from Figure 3.2 that

$$|\mathbf{K}| = \frac{2\sin\theta}{\lambda} \tag{3.6}$$

However the electron wave interaction shown is only for one atom. If we now consider interference between waves scattered from two parallel planes of atoms, then we have to introduce constructive and destructive interference. From Figure 4.3, we have two planes of atoms, P1 and P2 normal to the vector CB.

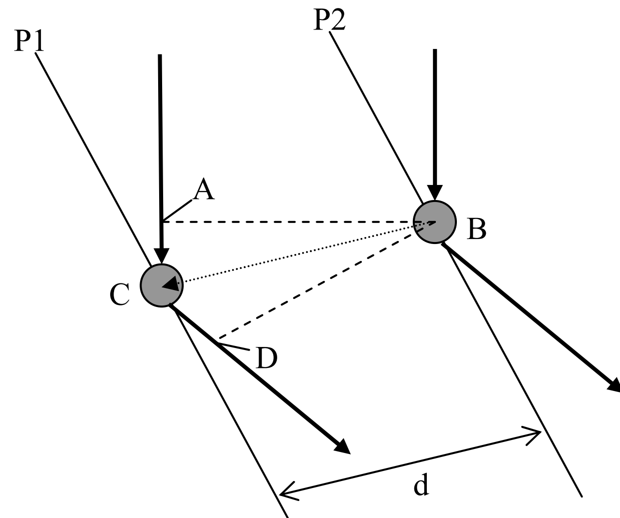

Figure 3.3 Showing the constructive and destructive interference of two wavefronts.

When the planes of atoms diffract the electron wavefronts, you can define the path difference traveled by the two rays as

$$AC + CD = 2d \sin \theta \qquad (3.7)$$

It is known from the last section that at the Bragg angle electron waves interfere constructively. At this angle, the path difference is given by nλ, and the equation (3.7) becomes

$$n\lambda = 2d \sin \theta_B \qquad (3.8)$$

From equation (3.6) and (3.8), we can express vector $|\mathbf{K}_B| = \frac{1}{d}$. Comparing with equation (3.5), we can derive $\mathbf{K}_B = \mathbf{g}$ at the Bragg conditions, that is $\theta = \theta_B$.

Based on the concepts that have been derived, we can now construct a sphere of radius 1/λ, generally called the "Ewald sphere". Figure 3.4 shows the representation of the sphere in two dimensions. When an incident beam of vector $\mathbf{k_I}$ is incident on a crystal with origin O, all the possible diffracted vectors, $\mathbf{k_D}$ that may arise lie on a sphere with radius equals to the incident wave vector $\mathbf{k_I}$, that is1/λ. If we place the sphere in the reciprocal lattice, at any point when the surface of this sphere intersects a reciprocal point, the Bragg condition is met, and that point will appear in the diffraction pattern as shown in Figure 3.4. Therefore a diffraction pattern is, in fact, the intersection of the Ewald sphere with reciprocal points.

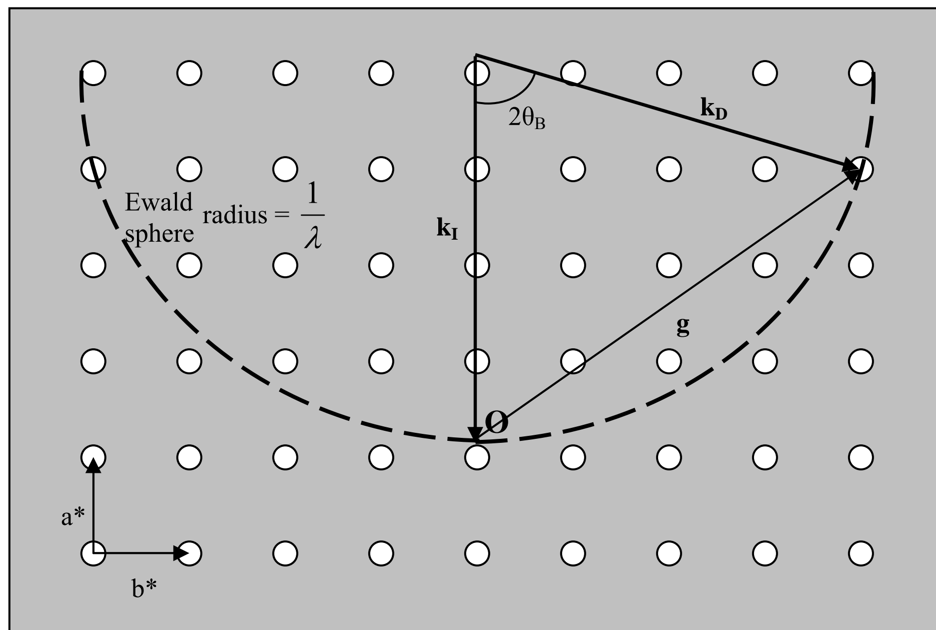

Figure 3.4 Ewald sphere construction showing the sphere superimposed on the reciprocal lattice points. Points that intersect the sphere will satisfy the Bragg condition and will appear in the diffraction pattern.

It is clear from the description of the Ewald sphere that the radius of the sphere changes as we change the energy of the incident beam (kV). As the kV increases, the

sphere becomes bigger with a larger radius and the surface of the sphere becomes flatter with a more useful curvature for obtaining information. This however, affects the diffraction pattern because the length of **g** decreases as kV increases. Therefore, the spacing between each lattice point, which satisfies the Bragg condition, is closer at higher kV. This can be noticed clearly in a diffraction spot pattern, where the spots are closer at higher kV.

As mentioned for TEM samples, in reciprocal space instead of points, rods or relrods are found. The Fourier transformation of an infinite real space lattice will result in reciprocal lattice points. However in a TEM specimen, being a thin foil, it has finite lattice points in real space, which will result in relrods in reciprocal space, after Fourier transformation. This is illustrated in Figure 3.5 (a), where relrods from the reciprocal lattice points protrude out of the reciprocal plane at the origin. When the Ewald sphere is constructed, we can observe that the sphere "misses" the centre of the two relrods drawn in this diagram. The amount by which the Ewald sphere misses the centre of the relrod is called the excitation error, s. The larger the value of s, the lower the intensity of the relrod. This can clearly observed in a single crystal Si (001) spot diffraction pattern, where the spots corresponding to the planes of atoms away from the origin, the undiffracted central beam, have a lower intensity than those near the origin.

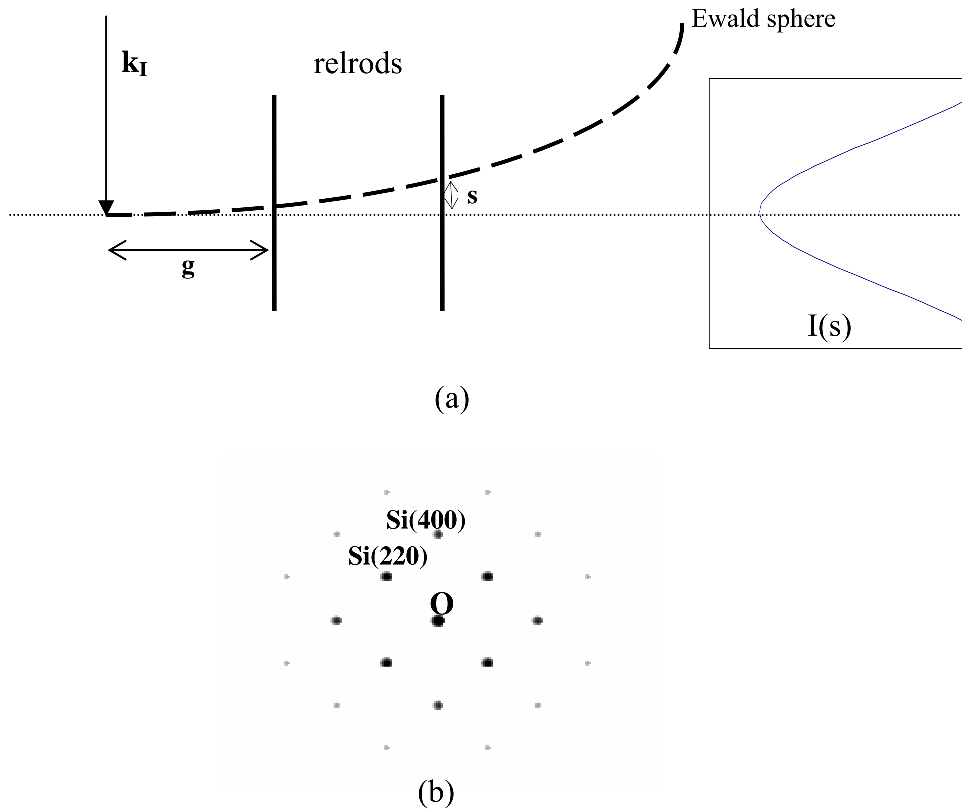

Figure 3.5 (a) Relationship between diffracted intensity and excitation error s. (b) Illustrating the relationship between diffracted intensity and excitation error, where relrods intercepted by the Ewald sphere further away from the origin, O, are lower in intensity due to excitation error.

In conclusion, a diffraction pattern shows the intersection of the Ewald sphere with reciprocal relrods in the reciprocal lattice space. The resulting pattern is a Laue spot diffraction pattern as shown in Figure 3.5 (b), which is an example for a single crystalline sample. However, if a random polycrystalline sample is examined, the reciprocal lattice points become spheres. This is because the same reciprocal lattice has every possible orientation with respect to the incident beam. This give rise to the Debye Scherrer powder ring diffraction pattern.

3.3.2 Structure factor

Since we have developed an explanation of diffraction under the Bragg conditions, we can now look at the effects of the structure of the crystalline material on the intensity of diffracted beams. Unit cells are stacked on each other to make up a crystal structure. So we must first, write down the equation of the amplitude of the electron beam scattered from a unit cell:

$$A_{cell} = \frac{e^{2\pi i k \cdot r}}{r} \sum_i f_i(\theta) e^{2\pi i K \cdot r_i} \tag{3.9}$$

where the summation is over all *i* atoms in the unit cell and θ is the angle of the diffracted beam relative to the incident beam. The vector **r** is the distance from a point P on the bottom of the specimen to the scattering center, and $\mathbf{r}_i$ is the position of atom *i* in the unit cell. $f_i(\theta)$ is the atomic scattering factor for the "*i*" atom. We can define the quantities $\mathbf{r}_i$ and **K** as vectors in real and reciprocal space respectively

$$\mathbf{r}_i = x_i\boldsymbol{a} + y_i\mathbf{b} + z_i\mathbf{c} \tag{3.10}$$

$$\mathbf{K} = h\mathbf{a}^* + k\mathbf{b}^* + l\mathbf{c}^* \tag{3.11}$$

It can be seen that specific unit cell geometry will play a role in the intensity of the diffraction spot. We can then rewrite equation (3.9) as:

$$A_{cell} = \frac{e^{2\pi i k \cdot r}}{r} \sum_i F(\theta) \tag{3.12}$$

We can define F(θ) as the structure factor of the unit cell, which depends on the nature of all the atoms in the unit cell, their positions, and the direction in which the beam is propagating. This introduces "selection rules" for diffraction spots for different crystal structures. For a body-centered-cubic (BCC) crystal, atoms are placed at the (0,0,0) and (1/2, 1/2, 1/2) positions. When we include this information into the equation, we can obtain the selection rules for the BCC system:

$$F = 2f \qquad (h + k + l) \text{ even}$$

$$F = 0 \qquad (h + k + l) \text{ odd}$$

Similarly, for face-centered cubic (FCC) crystals:

$$F = 4f \qquad (h + k + l) \text{ even or all odd}$$

$$F = 0 \qquad (h + k + l) \text{ mixed even and odd}$$

For a more complicated crystal structure such as the diamond cubic crystal structure for silicon, we have to think of it consisting of two penetrating FCC Si lattice which are displaced by a basis vector of (1/4, 1/4, 1/4) from each other. This gives the selection rules for this crystal structure:

$$F = 4(f_{Si} - if_{Si}) = 0 \quad h, k, l \text{ all even and } (h+k+l) = 2N \text{ where N is odd}$$

This means that (200), (222), (420) spots will not appear in a Si (100) diffraction pattern due to this selection rule. This selection is true for X-ray diffraction data. However for electron diffraction pattern, not all the spots satisfy the Bragg condition, due

to the smaller Bragg angle (in terms of mrad) of high energy electrons, which can be, determine from equation (3.8). Therefore in the case of Si (100), with the omission of (111), only (220), (400), (620) reflections are frequently observed in electron diffraction.

3.3.3 Selected area electron diffraction

At this point, we have covered the theoretical background needed to understand electron diffraction from TEM samples. We shall now turn the attention to the actual acquisition of electron diffraction patterns in a conventional TEM. It is important to obtain a diffraction pattern from a specific region of the TEM sample. The principle of this process is known as selected area electron diffraction (SAED), which can be understood with reference to Figure 3.6 (a). When an incident beam strikes a TEM sample, all transmitted and diffracted rays contribute to the diffraction pattern formed in the back focal plane of the objective lens. However if a selected area diffraction aperture is inserted coplanar with the image only transmitted and diffracted rays that originate within the darkened region of the specimen are allowed into the remaining magnification system. Therefore, the diffraction pattern formed on the viewing screen only originates from the darkened region of the sample. The magnification factor of a SAED is usually discussed in terms of an equivalent camera length that would be necessary to produce the same magnification in a diffraction camera without any lenses. This approach can be schematically shown in Figure 3.6 (b), where an incident beam is diffracted to form a two spot diffraction pattern, a transmitted spot and diffracted spot, on the viewing screen. If the distance between the transmitted to the diffracted spot is R, and the camera length is L then we have,

$$2\theta = \frac{R}{L} \approx 2\sin\theta \text{ for small values of } \theta \text{ (mrad)} \tag{3.13}$$

Rearranging Bragg relation, $2 \sin \theta = \frac{\lambda}{d_{hkl}}$ and substituting into the equation above:

$$Rd_{hkl} = \lambda L \tag{3.14}$$

where λL is the camera constant which describes the magnification of the diffraction pattern. This is a very important relation, which is the basis for indexing and interpreting the SAED patterns obtained from the experiments carried out which would be illustrated in the results and discussion chapters.

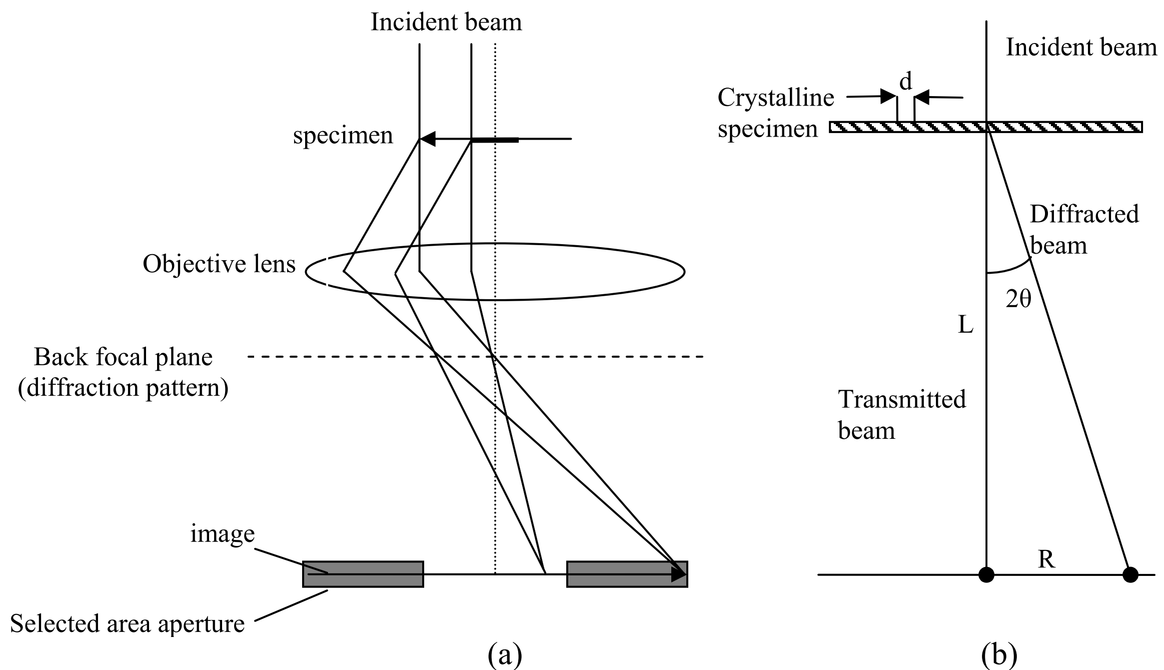

Figure 3.6 (a) The insertion of a selected area aperture allows the formation of the diffraction pattern only from the selected area. (b) Schematic of the formation and geometry of a diffraction spot in relation to the transmitted beam.

3.4 Bright and dark field imaging

As in most imaging techniques, contrast allows images to be viewed. Basically, contrast is actually formed when there is scattering of the radiation, which is used to illuminate a specimen. In TEM imaging, contrast can be formed by several ways. One such source of contrast is mass thickness contrast, which results from elastic scattering of electrons. This scattering is a strong function of the atomic number Z, the density ρ and the thickness of the specimen. Another type is called "Z contrast" which is due to the difference in atomic masses that may be present in the specimen. This differs from mass thickness contrast in the sense that only high angle, incoherently scattered electrons are used. This is typically used in scanning transmission electron microscopy (STEM), where a special detector known as a high angle annular dark field (HAADF) detector is used to form the images. For crystalline specimens, the primary source of contrast is from diffraction. The presence of crystal lattice defects, difference in thickness and atomic number due to the presence of different phases, and artifacts that may have occurred during sample preparation affect the local diffracted intensities of the electron beam passing through the sample. This imaging mode is termed *diffraction contrast*. The contrast resulting from these factors will be further illustrated in the analysis of the bright and dark field images in the discussion chapters. We will discuss the exact method for obtaining bright and dark field images in a conventional TEM.

In a conventional TEM, an objective aperture situated in the back focal plane of the objective lens is inserted to only allow the electron beam of interest through to the rest of the microscope to form an image. For the formation of bright field images, the objective aperture is used to select the transmitted beam traveling along the optic axis and

blocking off diffracted beams so as to form the image. This creates diffraction contrast in the image as shown in Figure 3.7 (a). Alternatively, the objective aperture could be displaced from the optic axis as shown in Figure 3.7 (b); to allow a diffracted beam to pass through while intercepting the transmitted and other diffracted beams. The image formed is known as a displaced dark field image. But it is a poor quality image because of additional spherical aberration and astigmatism present when the electron path is not close to the optic axis. In order to retain the resolution of the bright field mode, the incident beam is tilted by 2θ, which will allow the diffracted beam to travel along the optic axis as shown in Figure 3.7 (c). This technique is known as centered dark field imaging, and was used to obtain the dark field images in this study.

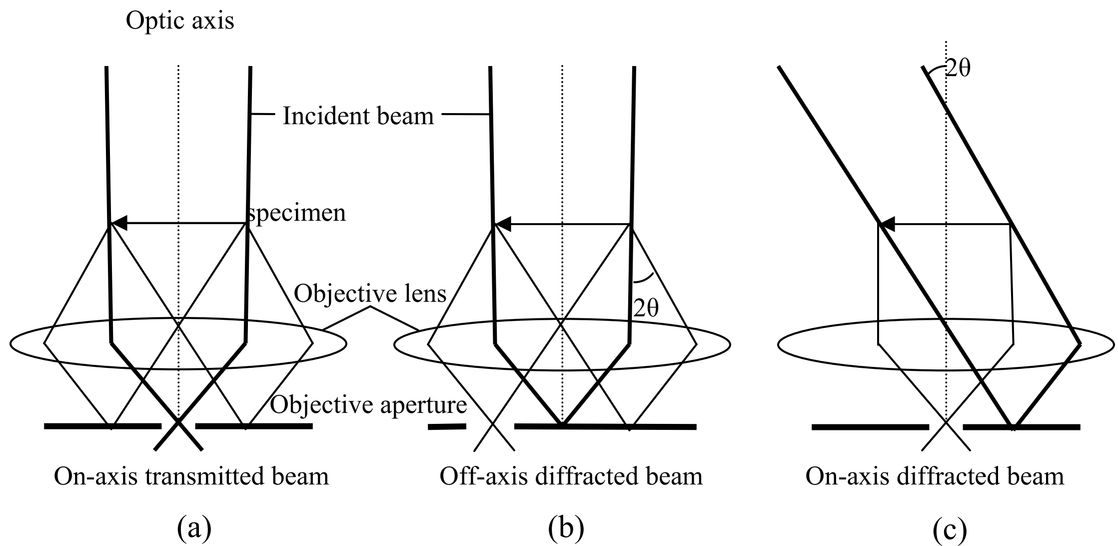

Figure 3.7 (a) Objective aperture selecting the on-axis transmitted beam to form a bright field image. (b) Objective aperture selecting the off-axis diffracted beam to form a displaced dark field image. (c) Another method to form a dark field image with the objective aperture selecting the on-axis diffracted beam.

3.5 Basic optics operation of the JEM 2000V TEM

Figure 3.8 shows a schematic diagram of the condenser and objective lens portions of the JEM 2000V TEM, which is the basic TEM used in this study. The basic operation of the optics in TEM for the different imaging modes will be discussed. The electrons are accelerated to 200kV in the LaB_6 thermal electron gun. CL1 is the first condenser lens whose function is to create a demagnified image of the gun crossover and control the minimum spot size obtainable in the rest of the condenser system. CL 2 is the second condenser lens whose function is to converge the beam at the specimen and control the diameter of the illuminated area of the specimen. The condenser aperture, CL, controls the fraction of the beam that hits the specimen and the intensity of illumination. This aperture increases resolution but degrades intensity and there is a tradeoff whenever an aperture is used. Parallel illumination mode, illustrated in the Figure 3.8, provides the best resolution but reduced intensity.

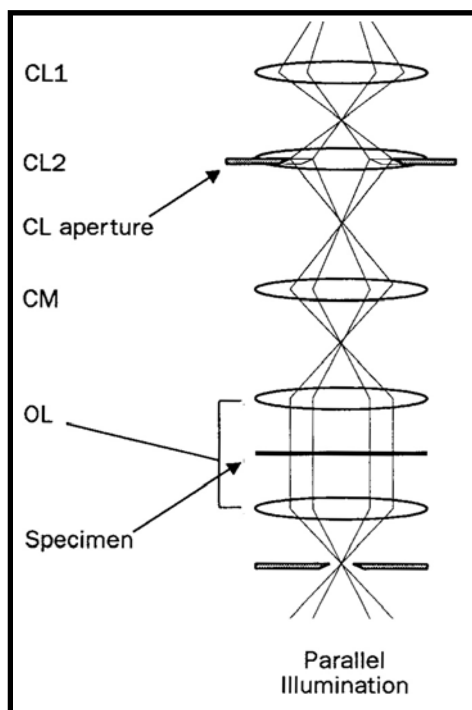

Figure 3.8 Schematic of condenser and objective lens of JEOL 2000V.

The objective lens, OL, forms an inverted initial image, which is subsequently magnified. Both the diffracted and unscattered electrons are focused by the objective lens. A diffraction pattern is formed at the back focal plane of the objective lens. The sample sits within the objective lens. The objective aperture is placed in the back focal plane of the image. Its function, as discussed in section 3.4, is to select those electrons, which will contribute to the image, and thereby affect the

appearance of the image, improving the contrast of the final image.

Figure 3.9 shows a schematic diagram of the imaging forming system in the JEM 2000V TEM. Below the objective aperture is the field limiting aperture or more commonly called as the selected area diffraction aperture in section 3.3.3. Its role is to allow the selection of an area of a sample to contribute to the diffraction pattern. The first intermediate lens can be focused on either the initial image formed by the objective lens, or the diffraction pattern formed at the back focal plane of it magnifies the image by a constant factor and determines whether the viewing screen shows a diffraction pattern or an image. Magnification in the electron microscope can be varied from hundreds to several hundred thousands times. This is done by varying the strength of the 2nd and 3rd intermediate lenses and the projector lens. Not all lenses will necessarily be used at lower magnifications.

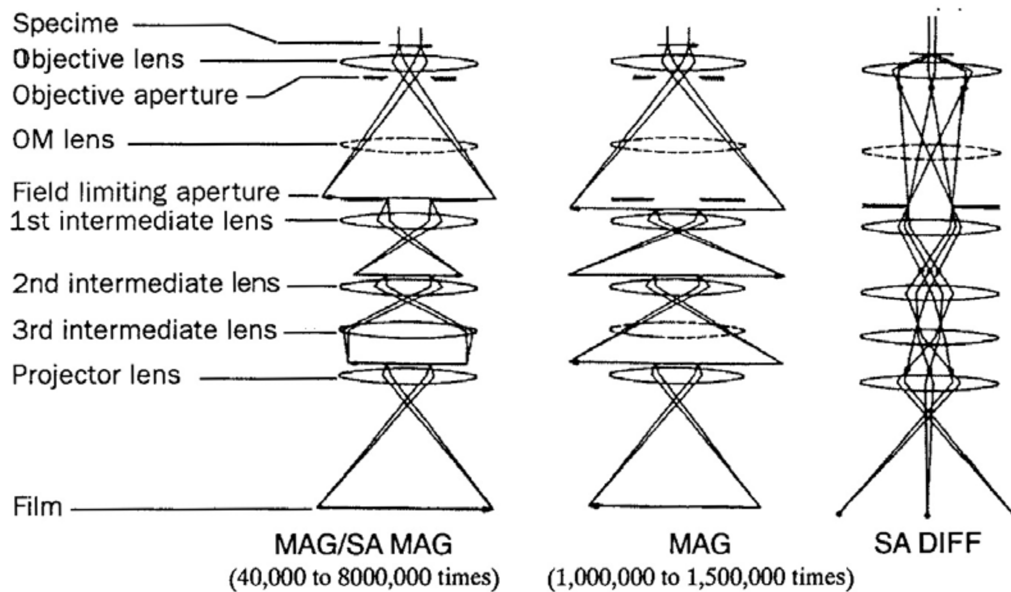

Figure 3.9 Schematic of image forming system in JEOL 2000V TEM.

References:

[1] Elizabeth M. Slayter and Henry S. Slayter, *Light and electron microscopy*, Cambridge University Press, USA, (1992), Chapt. 2.
[2] Stanley L. Fledger, John W. Heckamn Jr and Karen L. Klomparens, *Scanning and Transmission Electron Microscopy, an Introduction,* W.H. Freeman and Co, (1993), Chapt. 3.
[3] M.H. Loretto, *Electron Beam Analysis of Materials,* 2nd edition, University Press, (1994), Chapt. 1.
[4] J.M. Cowley, *Diffraction Physics,* Elsevier-Science Publishers B.V., Amsterdam, (1990), Chapt. 2.
[5] D.B. Williams and C.B. Carter, *Transmission Electron Microscopy – Diffraction,* Plenum, New York, (1996), Chapt. 12.

Chapter 4 Experimental setup

This chapter covers the analytical equipment and sample preparation used in this study. The first section describes the highly modified *in-situ* ultra-high vacuum (UHV) TEM, which is the primary analytical tool, used in this study. This is followed by discussion of the preparation and cleaning of the (100) Si and $Si_{0.75}Ge_{0.25}$ substrates. The *in-situ* deposition of the nickel film using electron beam evaporation followed by the *in-situ* annealing using direct resistive heating will be discussed. Finally the data acquisition tools, the Gatan Imaging Filter (GIF) and DualView digital cameras, used throughout the experiment are presented.

Two types of substrates were used to conduct the experiments in the MERLION system. They are (i) clean and oxide covered Si (100) and (ii) relaxed $Si_{0.75}Ge_{0.25}$ (100) substrates. Our experiments involve the *in-situ* deposition of thin nickel films of 12nm thickness at ambient temperature and followed by *in-situ* annealing to induce a thermal reaction between the Ni film and the underlying substrate.

4.1 The MERLION system

The chief analytical tool used in our work is a highly modified *in-situ* ultra-high vacuum (UHV) Transmission Electron Microscope (TEM) -**M**odified **E**lectron-microscope for **R**ea**L**-time **I**n-situ **O**bservations on a **N**anoscale (MERLION). Built from

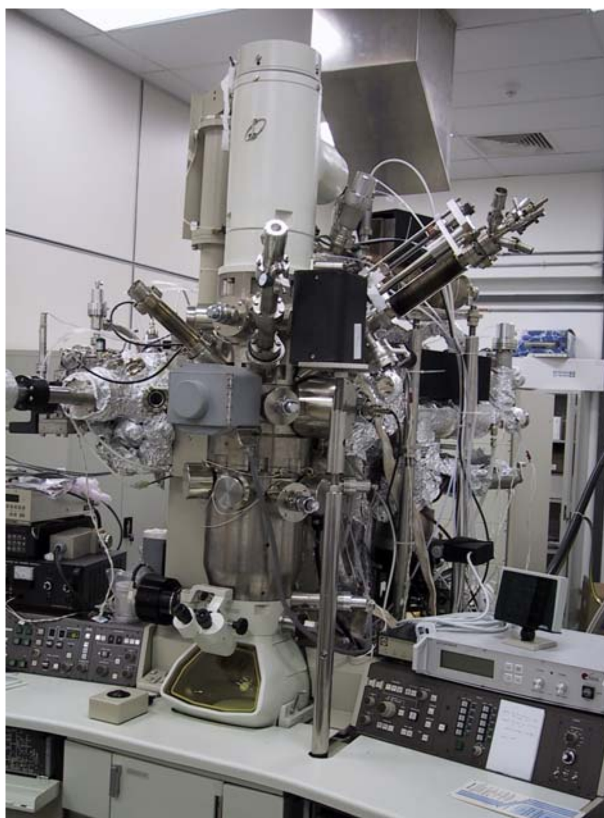

Figure 4.1 The MERLION system.

a JEOL JEM-2000V TEM machine, the MERLION comprises a 200kV electron beam-line (using a LaB_6 thermal filament) that was integrated into an UHV materials growth chamber. The JEM-2000V machine is designed to perform microscopy, such as high resolution electron microscopy, electron diffraction, analytical microscopy (EDS, EELS, etc.) in ultra high vacuum of 10^{-8} Pa order. The main features of the JEM-2000V are:

- The specimen surface is purified in the microscope column or “pre-treating chamber”. The purified specimen is placed under a clean environment for microscopy. Use of special specimen holders makes possible studies of atomic level phenomena on the specimen surface due to specimen heating, evaporating, gas reaction, etc.

- The specimen can be purified by heating, evaporating and/or treated by gas reaction in the "pre-treating chamber" before microscopy.
- Constant high-resolution microscopy is assured under UHV by using a motor-driven goniometer employing perfect metal seals thus ensuring perfect vacuum sealing.
- Use of top class high-resolution objective lens improves atomic level microscopy. Since a condenser-objective lens is employed, electron diffraction in the nanometer area and convergent beam electron diffraction can easily be performed. Other detectors, such as EELS, can be mounted optionally if desired.
- The α-selector is equipped to ease the illumination system selection.

The MERLION system houses a unique system for the *in-situ* development of advanced materials which comprises of: (a) *in-situ* gas injection and electron beam evaporation; (b) *in-situ* sample heating (1200°C) and (c) *in-situ* EELS (electron energy loss spectroscopy) and EFTEM (energy-filtered TEM). The system enables deposition of a range of materials onto different substrates, and the direct observation of micro- and nano-structure evolution through the high-resolution imaging and diffraction capabilities of the TEM. Deposition may be performed either by electron beam evaporation, reactive gas injection, or both. The MERLION system is equipped for quantitative image acquisition and analysis via an electron spectrometer, enabling electron energy loss spectroscopy and energy-filtered TEM. Real-time video recording of microstructural evolution is accomplished by an integral video-rate TV camera.

4.2 Preparation of Si (100) substrates

Boron-doped, *p*-type silicon wafers (resistivity of 6-9 Ωcm) with <100> orientation were used as starting substrates for our experiments. The outline of the steps involved in preparing the Si substrates is shown in Figure 4.2. The wafers were cut to exactly 6.5 by 2 mm rectangles, to fit the size specification of the UHV TEM double tilt direct heating holder.

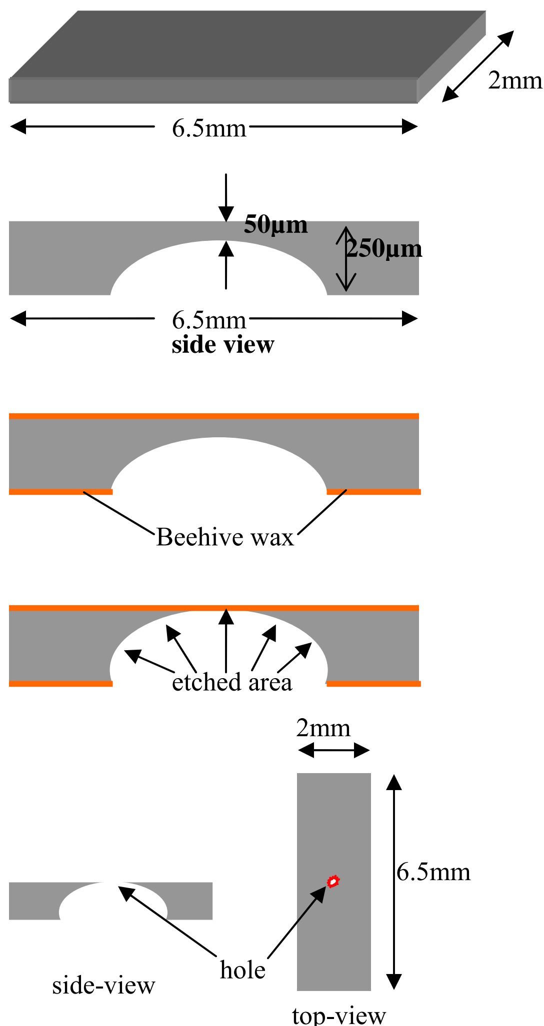

6.5 by 2 mm rectangle samples were hand ground to 250µm from the backside of wafer.

The hand ground wafers were unaxially dimpled to remove 200µm leaving behind 50µm, to form a groove in the middle of the wafer.

The dimpled wafers were then coated with a protective beehive wax except for the groove area for the subsequent etching step.

The wafers were then etched in a 49%HF: 70%HNO_3:H_2O mixture in the ratio of 1:3:1, under a transmission light microscope until perforation. TEM analysis can be done in the thin areas around the holes. Etching occurs only in the groove area which is without the beehive wax.

The wafers were then boiled in tricholoethylene (TCE), acetone, methanol and ethanol to remove the beehive wax. The sideview and top view shows a clean sample with thin area (in red in top-view) around the hole region.

Figure 4.2 Steps involved in preparing Si (100) substrates.

Prior to loading in the microscope the samples were cleaned using standard SC-I and SC-II processes, followed by dipping in 20% HF for 30 seconds to remove native oxide. To obtain an oxide-covered Si (100) surface, the last 20% HF step to remove the native oxide was missed out.

4.3 Preparation of relaxed $Si_{0.75}Ge_{0.25}$ (100) substrates

The $Si_{0.75}Ge_{0.25}$ relaxed films were grown using the ultra-high vacuum chemical vapour deposition (UHVCVD) technique. A 3μm $Si_{1-y}Ge_y$ (y:0→0.25) relaxed graded buffer layer was grown on p-type (100) silicon wafers to the desired concentration at a grading rate of 10% Ge μm^{-1}, at 900 °C and 25mTorr. Subsequently, a uniformly relaxed $Si_{1-x}Ge_x$ layer (x = 0.25) of thickness 3.0μm was grown over the substrate. The frontside of the $Si_{0.75}Ge_{0.25}$ wafer was then subjected to chemical mechanical polishing (CMP), leaving behind a uniformly smooth surface, with the thickness of the relaxed $Si_{0.75}Ge_{0.25}$ films down to 1μm. Details of the growth conditions and characterisation of the relaxed $Si_{0.75}Ge_{0.25}$ films can be found elsewhere.[1,2,3]

The procedure used to prepare the TEM samples for the relaxed $Si_{0.75}Ge_{0.25}$ substrates differs from the one used for Si (100) explained in the preceding section. This is because the relaxed $Si_{0.75}Ge_{0.25}$ film on the frontside of the wafer tended to be etched away when samples were prepared using the etching method described. Therefore an alternative method was used, whereby the relaxed $Si_{0.75}Ge_{0.25}$ substrates were prepared using the conventional mechanical polishing method is described in Figure 4.3.

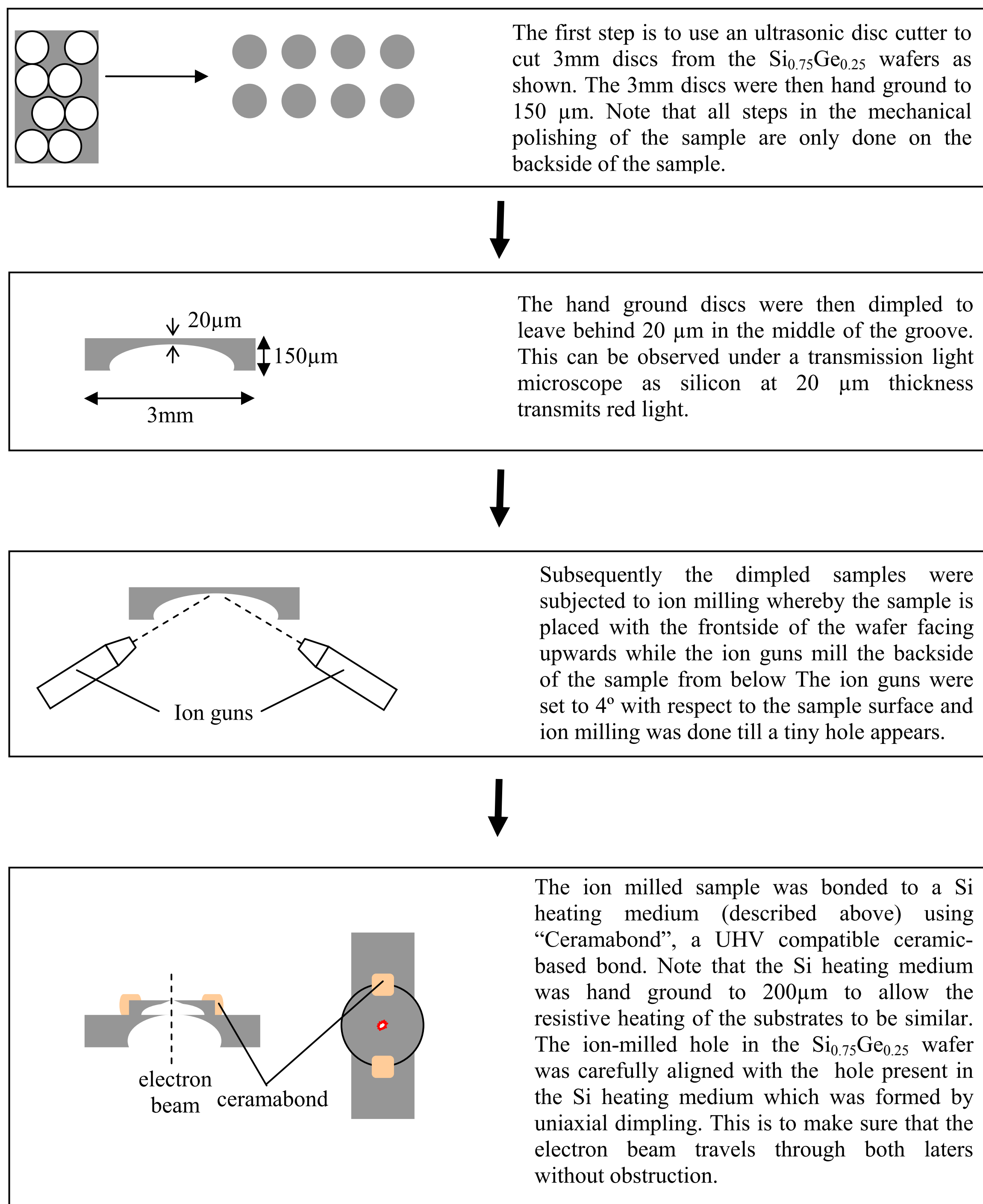

Figure 4.3 Steps involved in preparing $Si_{0.75}Ge_{0.25}$ (100) substrates.

4.4 Nickel deposition

In the UHV evaporator EFM 3 (Evaporator with integral Flux Monitor) the evaporant is either evaporated from a bar, from a rod or from a crucible. This is achieved by electron bombardment heating. The bombarding electron beam induces a temperature rise of the evaporant, causing evaporation. Figure 4.4 shows the evaporator attached to the MERLION system.

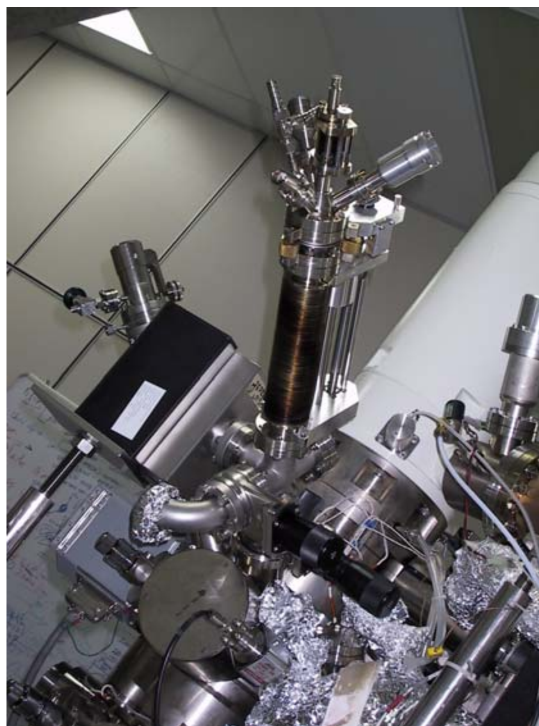

Figure 4.4 The UHV evaporator EFM3 as attached to the MERLION system.

The crucible-free evaporation is characterized by an ultimate degree of cleanliness with only slight increases of background pressure. From an appropriate crucible, low melting point, low vapor pressure or reactive materials can be evaporated. The instrument is designed for high precision sub-monolayer up to multi-layer deposition of a wide variety of evaporants, including highly refractory materials.

Once calibrated the flux monitor replaces the necessity of a quartz thickness monitor that continuously monitoring the evaporation rate directly. The beam exit column contains an ion-collector, which serves as a flux monitor. At a given electron emission current I_{EM} and e-beam energy, the ion flux measured is directly proportional to the flux of evaporated atoms. The EFM comes with a shutter at its outlet, which can be opened and closed by a rotary drive. This allows precise flux adjustment prior to exposure, and exact control of the evaporation time. The evaporation cell is contained in a water-cooled copper cylinder (cooling shroud). This, and the fact that just a restricted region of the evaporant is heated, means that the background pressure during evaporation is kept below 10^{-10} mbar. But this also depends on the target material and on the pumping speed of the vacuum system.

The specifications for *in-situ* Ni deposition using the EFM3 are: 2mm diameter Ni rod, 900V, 9-15mA emission current, 25 nA of ion current giving a deposition rate of 2nm/hour. The deposition was calibrated using thickness measurements obtained by ex-situ Rutherford Backscattering Spectroscopy (RBS). The deposition time for 12nm of Ni film takes 6 hours. This deposition condition was applied to all the experiments in this study.

4.5 Resistive annealing

Resistive annealing of samples was done by electrical connections from the sample holder internally to an external regulated DC power supply. Anneal temperatures were calibrated using an infrared pyrometer with an emissivity setting of 0.70 used based on

published Si emissivity tables[4]. Figure 4.5 shows a plot of current (mA) input to the Si substrate versus temperature readings from the substrate using the pyrometer.

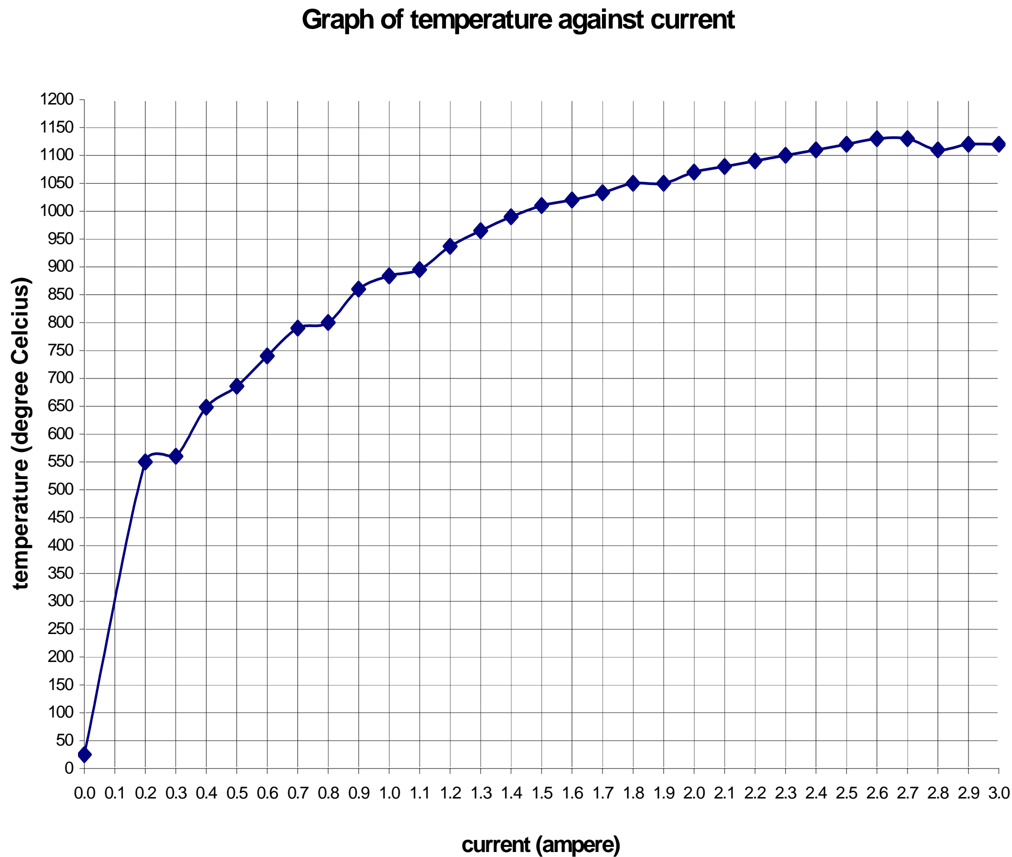

Figure 4.5 Graph of current input versus temperature reading from the Si substrate (the temperatures are measured using a pyrometer), x-axis indicates current, each interval is 0.1, unit: ampere; y axis indicates temperature, each interval is 50, unit: degree Celsius.

4.6 Observation and data collection

For this section, the two different data acquisition devices, which are part of the MERLION system, are covered. Firstly, the Gatan DualView digital camera and its specifications are explained. This is followed by a brief description of the Gatan Image Filter (GIF). The theory and the application of the GIF are described in detail in the next

few sections, which is necessary to understand the information presented in the results and discussion chapters.

4.6.1 Gatan DualView 780 digital camera

The Gatan DualView digital camera (pointed to by the yellow arrow in Figure 4.6) has a large field of view, real time imaging, MPEG video recording mode, full 360-degree image rotation and totally automatic exposure control. The camera features an anti-blooming control to allow the capture of diffraction patterns without image streaking artifacts.

Figure 4.6 The Gatan DualView system as attached to the MERLION system.

4.6.2 Gatan Imaging Filter (GIF)

The GIF (as shown in Figure 4.7) is attached beneath the camera chamber of the JEOL JEM-2000V, adds to it the capabilities of Energy-filtered TEM (EFTEM) Imaging and Electron Energy Loss Spectroscopy (EELS). The GIF's sophisticated electron optics

and energy selecting slit allow images and diffraction patterns produced by the TEM to be transformed into energy-filtered (energy-selected) images and diffraction patterns. Alternately the GIF can form electron energy-loss spectra with a range of energy dispersions. The images, diffraction patterns or spectra can be observed in real-time via a TV-rate CCD camera or can be acquired by a Multi-Scan CCD camera (MSC) directly onto a PC computer for processing, display, annotation or printing.

Figure 4.7 The Gatan Image Filter system as attached to the MERLION system.

4.6.2.1 Theory of operation

In normal operation, the GIF entrance aperture (as shown in Figure 4.8) is used to select a part of the image or diffraction pattern that is projected by the microscope into the viewing chamber [5]. The electrons enter the magnetic prism and are bent by approximately 90°. The exact bending angle of the electrons depends on their energy; the greater the energy-loss it has experienced, the larger the angle the electron is bent

through. Besides bending the electron beam and creating energy dispersion, the prism also forms a focused energy dispersed image at some distance behind the prism. This is the energy-loss spectrum. The energy dispersion created by the magnetic prism decreases with the primary energy of the electrons and drops below 1 μm/eV at primary energies ≥200 KeV.

The energy-selecting slit is located in the plane of the focused energy-loss spectrum. It can be pneumatically inserted into the spectrum for energy-filtered imaging, or alternatively be left out for unfiltered imaging or spectroscopy. The design of the slit is such that the position of the bottom slit edge is fixed, whereas the top edge can be moved up and down.

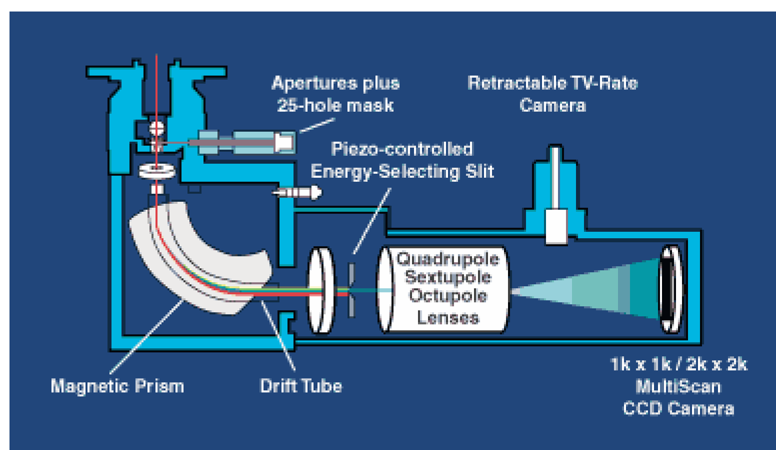

Figure 4.8 Schematic of the Gatan Image Filter.

The post-slit quadrupole-sextupole assembly is located right after the energy-selecting slit. It can be operated in two modes:

1. In the EELS Mode, it projects the focused energy-loss spectrum at the energy-selecting slit onto the cameras.

2. In the EFTEM Mode, it takes the electrons that were selected by the energy-selecting slit and projects an energy-selected, achromatic, aberration free version of the TEM image selected by the entrance aperture onto the cameras.

These two modes are described in detail in the next sections.

4.6.2.2 Basic concepts of EELS

When a fast (about 100kV) electron traverses a thin foil of a material, it may create various excitations by transferring (losing) energy to the material[6]. The excited states decay by emitting the transferred energy in the form of an X-ray, visible photon, Auger electron, heat, etc. Electron energy-loss spectroscopy (EELS) probes the primary excitation and therefore registers each excitation event independently of the exact de-excitation mechanism.

Three energy regions in the energy loss spectra can be distinguished. Energy losses of a few meV to a few hundred meV are predominantly due to vibrational excitations (phonons), but they can only be studied with energy resolution significantly better than that of most EELS systems. Collective excitations (plasmons), intraband and interband transitions cause energy losses between a few eV to 40eV. At energy losses above 40eV, one finds the inner shell excitations. These occur at energies

$$\Delta E \geq E_F - E_B \tag{4.1}$$

where ΔE is the energy loss, E_F is the Fermi level energy, and E_B is the binding energy of the inner shell (always negative).The corresponding feature in an energy loss

spectrum is an inner shell loss edge, whose threshold energy usually agrees to within a few eV with the known ionization energy for the appropriate electron shell of the atom. EELS of the inner shell losses therefore provide a convenient method of identifying atoms of different types in a thin foil of a material.

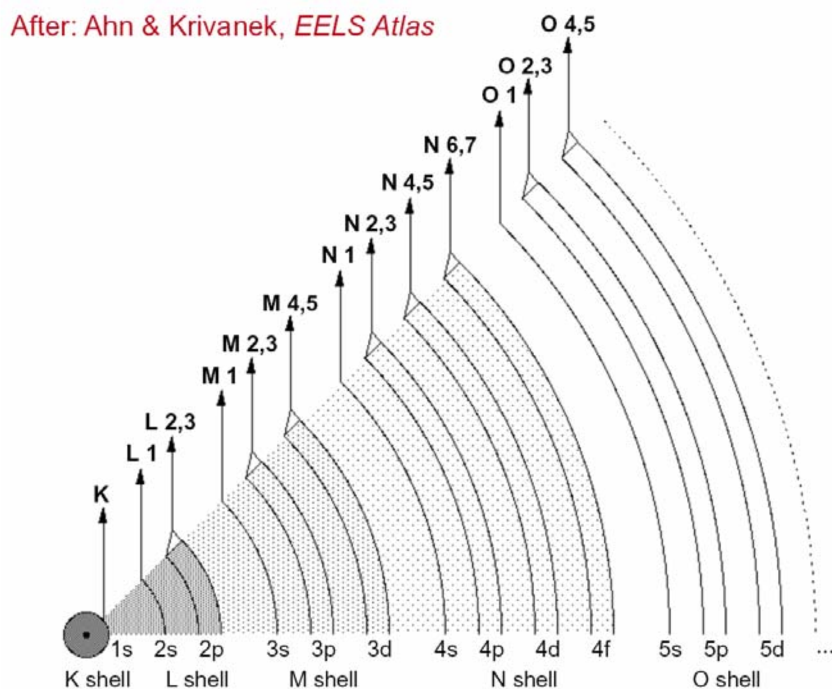

Figure 4.9 Showing the electron shells and transitions (adapted from reference 6).

The various inner shell edges that are labeled following standard spectroscopic notation are illustrated in Figure 4.9. Not all transitions listed occur in every atom. For instance, in Al, only the K and L shells are completely filled, and these give rise to the K and L edges. The M shell in Al is partially filled, and electrons from this shell give rise to the plasmon loss at 15eV and other low energy features. Further, electrons occupying certain shells such a M_1 and N_1 almost never give rise to recognizable features in an electron energy-loss spectrum, and the energies for the innermost shell transitions in

heavy elements are rather high (>10keV), and therefore not of interest to EELS. However, in general there is always at least one strong edge in the energy region 100-3000eV that is usable for every element, and for many elements there are edges in the optimum EELS energy region, which spans roughly 200eV to 1000eV.

4.6.2.3 Uses of EELS data

There are several levels of usage for EELS data. But however, only two of them, which were used for our studies, will be discussed. The simplest level is qualitative microanalysis that is the identification of the elements present in a thin microscopic sample as discussed above. The ionization edges of different elements are unique and are used as fingerprints to identify their presence in an EELS spectrum. Next, quantitative analysis whereby the composition of the sample can be determined by comparing the strength of its inner shell losses to calculated cross-sections. Although the calculations are actually carried out by the GIF software, the understanding of the method of calculation is important. Let us assume that we quantifying a K edge, although this can also apply to all other edges. The K-shell intensity above the background, I_K, is related to the probability of ionization, P_K, and the total transmitted intensity, I_T

$$I_K = P_K I_T \tag{4.2}$$

In a good thin specimen we can approximate I_T to the incident intensity, neglecting backscatter and absorption effects.

$$P_K = N\sigma_K \exp\left(\frac{1}{\lambda_K}\right) \quad (4.3)$$

where N is the number of atoms per unit area of the specimen (thickness t) that contribute to the K edge. The assumption of a single K-shell ionization event with cross-section σ_K is reasonable, given the large mean free path (λ_K) for ionization losses; but it explains why you have to make thin specimens. It also means that the exponential term is very close to unity, and so

$$I_K \approx N\, I_T \quad (4.4)$$

$$N = \frac{I_K}{\sigma_K I_T} \quad (4.5)$$

Therefore we can measure the absolute number of atoms per unit area of the specimen simply by measuring the intensity above background in the K edge and dividing by the total intensity in the spectrum and the ionization cross-section. We can easily extend this expression to a spectrum containing two edges from elements A and B, in which case the total intensity drops out and we can write

$$\frac{N_A}{N_B} = \frac{I_K^A \sigma_K^B}{I_K^B \sigma_K^A} \quad (4.6)$$

Equation 4.6 defines the ratio of the two elements A and B and can be applied to the other edges.

4.6.2.4 EFTEM

The analogy for the operating principle of the imaging filter used in the EFTEM mode is that of the imaging column of the TEM. As described in section 3.4, when an electron beam transverses a thin foil, the diffraction pattern of the specimen is located in the back focal plane of the objective lens. An objective aperture located in this plane can be used to select a part of the diffraction pattern and the selected part is transformed by the post-objective imaging lens into a magnified image, which is projected onto the viewing screen. With the imaging filter, the magnetic prism transforms the image or diffraction pattern projected by the TEM into the viewing chamber into an energy-loss spectrum and therefore plays a role similar to the objective lens. The plane of the focused spectrum is analogous to the back-focal plane of the objective lens. The energy-selecting slit can select part of the energy-loss spectrum for imaging and therefore plays the role of the objective aperture. The post-slit quadrupoles play the role of the post-objective lenses and can either produce a magnified, energy-selected image, or can produce a spectrum by imaging the plane of the energy-selecting slit.

4.6.2.5 Selecting an energy-loss

In both EFTEM and EELS mode, it is possible to shift between different energy-losses by moving the spectrum at the energy-selecting slit. For the GIF installed on the MERLION system, the energy-loss is selected by increasing the primary energy (high voltage) of the TEM. For example, if the zero-loss peak is in the center of the energy selecting slit and the imaging filter is selecting electrons of the primary energy E_0 eV. If the primary energy is then increased by E_1 eV, the new image will still be formed with

electrons of energy E_0 eV, meaning that it is formed with electrons that have lost precisely E_1 eV.

Since it would be unwise to increase the high voltage of any TEM above its maximum rating, the GIF control of the microscope primary energy is implemented in such a way that it can only decrease the primary energy. This means that in normal operation, the beam energy is automatically lowered by 3 keV as soon as the GIF is started up. In operation it can then increase as desired to select energy-losses up to 3 keV.

In the case of the MERLION system, whereby the primary energy of the JEOL JEM-2000V TEM is 200 keV, the actual energy of the electrons going through the specimen is 197 keV and the prism current is set to admit 197keV energy electrons through the energy-selecting slit. If the GIF setting is then adjusted to observe a 1 keV energy-loss image, the energy of the electrons going through the sample is increased to 198 keV, but the absolute energy of the electrons that go through the TEM column and are selected by the imaging filter will remain at 197 keV.

References:

[1] E.A. Fitzgerald and S.B. Samavedam, *Thin Solid Films* **294**, (1997), 3.
[2] M.T. Curie, S.B. Samavedam, T.A. Langdo, C.W. Leitz and E.A. Fitzgerald, *Appl. Phys. Lett*. **72**, (1998), 1718.
[3] C.S. Tan, W.K. Choi, L.K. Bera, K.L. Pey, D.A. Antoniadis, E.A. Fitzgerald, M.T. Currie and C.K. Maiti, *Solid-State Electron.* **45**, (2001), 1945.
[4] F. Roozeboom, *Advances in rapid thermal and integrated processing,* Kluwer Academic Publishers, Boston, (1996), Chapt. 4.
[5] D.B. Williams and C.B. Carter, *Transmission Electron Microscopy – Spectrometry,* Plenum, New York, (1996), Chapt. 37 and 38.
[6] C.C. Ahn, O.L. Krivanek, R.P Burgner, M.M. Disko, P.R. Swann, *EELS Atlas (A reference guide of electron energy loss spectra covering all stable elements)*, Gatan Inc., (1983).

Chapter 5 Results and discussion I: Ni on Si (100)

In this chapter, the first set of experiments, which is the thermal reaction of 12nm Ni film on clean and oxide-covered Si (100) is presented in section 5.1 and 5.2 respectively. A preliminary inspection of the cleanliness of the sample surface, which was carried out before the start of each experiment, is covered in the first sub-section. The following subsection describes the data obtained during the *in-situ* deposition of the nickel film on the Si substrate. The thermal reaction between the nickel film and the underlying substrate is presented in the last sub-section. At each annealing temperature step, phase transformations and thermal stability for the different nickel silicide phases are presented and discussed with reference to selected area electron diffraction (SAED) patterns, bright and dark field images obtained.

In this chapter, only indicated diffraction patterns will be used as examples to show how the calibration and indexing were done in the Appendix. Secondly, it should be noted that the section that shows the thermal reaction of Ni on oxide-covered Si is not the main focus in this work. It was done solely to demonstrate the effect of contaminants such as an oxide layer that may be present between the Ni and Si layer.

5.1 Ni film on clean Si (100)

5.1.1 Preliminary inspection of clean Si (100)

Electron energy loss (EELS) spectra, selected area electron diffraction (SAED) patterns, and bright field images were obtained to monitor the cleanliness of the sample. This was carried out in areas of the substrate where the focus of the experiment was. Any observations of carbon contaminants or oxide layers would deem the sample not suitable for the experiment. The experiment was conducted away from very thin areas where bending of the Si thin foil may occur. Bending may produce an external strain factor, which will affect the data obtained during reactions that occur in the experiments.

The EELS spectrum in Figure 5.1 (a) shows the Si $L_{2,3}$ and L_1 edges at energy loss of 99.2 and 149eV respectively. The spectrum was compared with standard EELS spectra found in the EELS Atlas[1]. It was also observed from the EELS data that there is no chemical shift of the energy at which the Si edges occurs. This suggests that there are no foreign atoms, such as oxygen, present in the Si substrate. The spectrum also indicated the absence of the carbon and oxygen K edge, at energy losses of 284 and 532eV respectively.

From the SAED taken from the clean Si sample shown in Figure 5.1 (b), the diffraction pattern shows a central spot with the symmetrical Si spots (refer to Appendix section A.2 for detailed indexing). There are no additional diffraction spots or rings that usually arise when there are contaminants present on the sample. Note that the (200) and (020) reflections, forbidden for the Si structure, do not appear in the SAED pattern. The corresponding bright field image in Figure 5.1 (c) shows the absence of dark patches, which appear if there are contaminants on the sample.

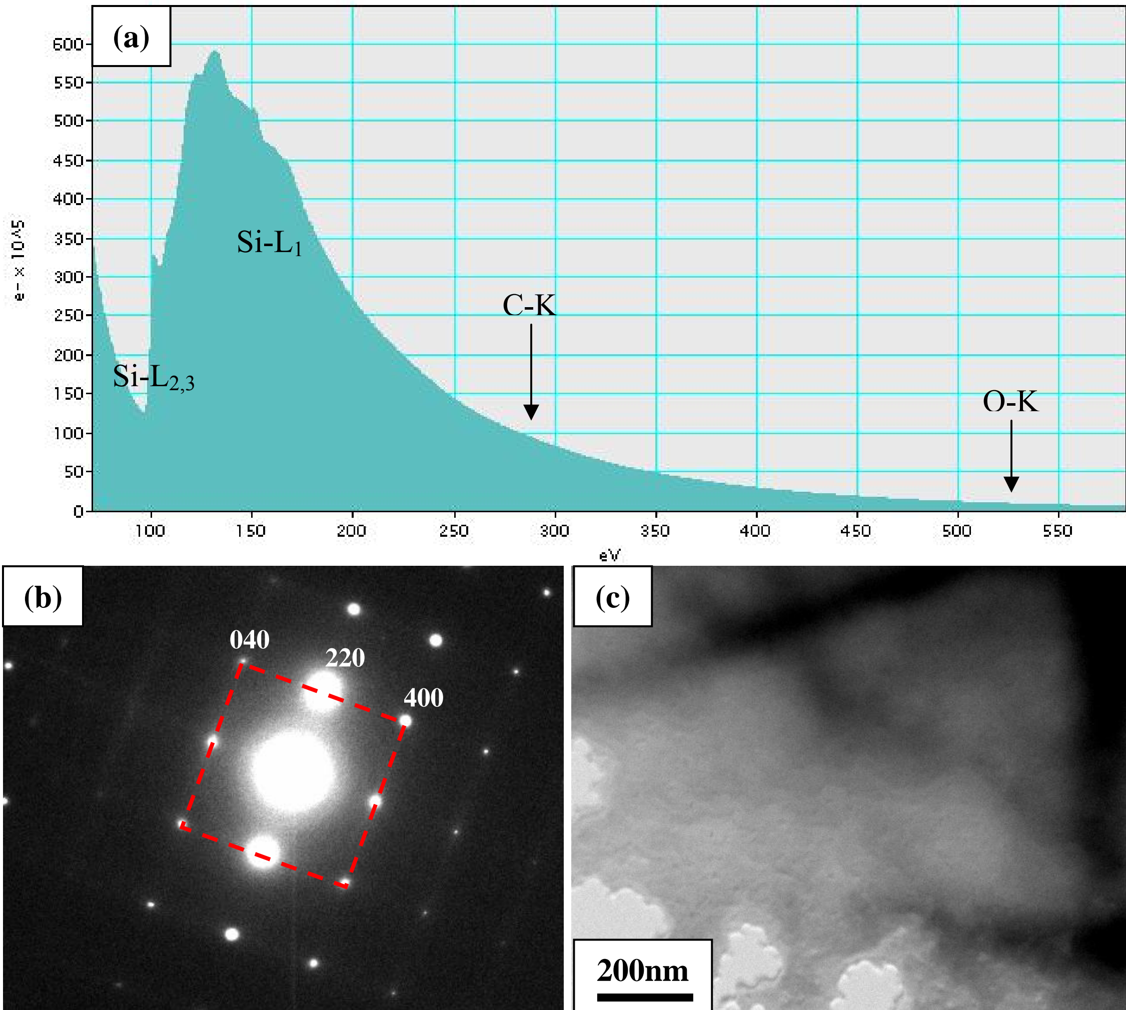

Figure 5.1 Showing (a) EELS spectrum, (b) SAED and (c) bright field image of a clean Si (100) substrate.

5.1.2 Nickel film deposition on clean Si (100)

After the preliminary inspection, nickel was deposited *in-situ* on a clean Si (100) substrate using the EFM3 evaporator. The conditions applied to deposit 12nm of Ni film on Si (100) are described in section 4.4. A uniform coverage of the substrate was achieved, with a Ni film of average grain size of ~8nm, as seen in Figure 5.2 (a). The SAED in Figure 5.2 (b) shows the rings corresponding to the face-centered cubic polycrystalline Ni film and spots of the (001) oriented Si substrate, (Refer to Appendix

section A.3 for detailed indexing). Additional faint rings with the Si (220) reflections as their centers in the SAED are accounted for by multiple diffraction. No evidence of a reaction of the Ni film with the Si (100) substrate was seen.

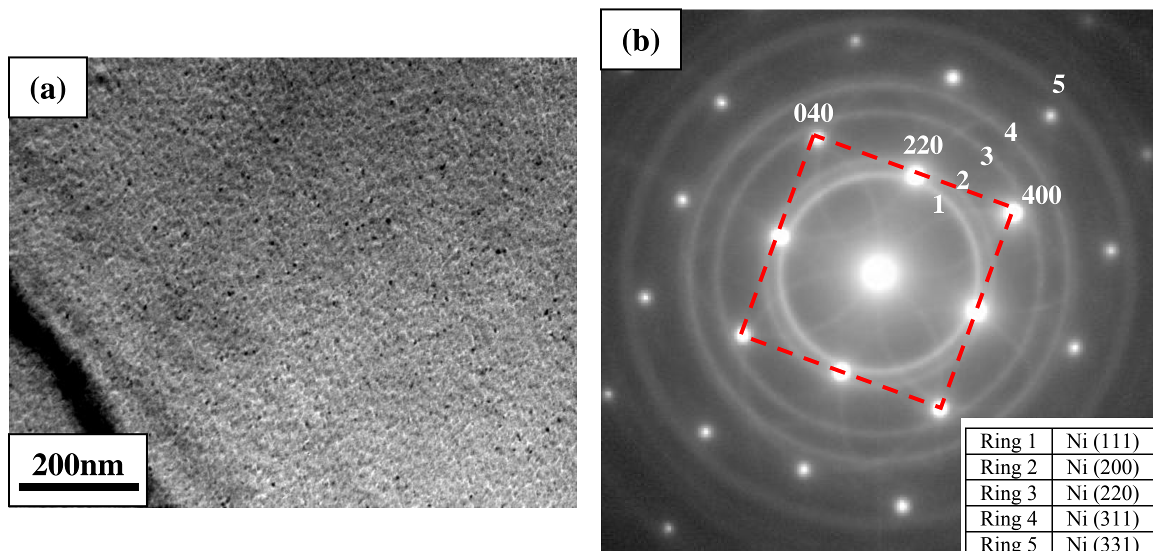

Ring 1	Ni (111)
Ring 2	Ni (200)
Ring 3	Ni (220)
Ring 4	Ni (311)
Ring 5	Ni (331)

Figure 5.2 Corresponding (a) bright field image and (b) SAED for as deposited 12nm Ni on Si (100).

5.1.3 Annealing of the 12nm Ni film on clean Si (100)

The sample was annealed at a rate of 30ºC per minute to a temperature of 300ºC. An initial reaction to form NiSi was observed above ~150ºC. Multiple reaction fronts were observed propagating rapidly across the surface to consume interfacial Ni. After 50 minutes annealing at 300ºC, it was confirmed from Figure 5.3 that the Ni deposit had transformed entirely to NiSi, forming a continuous polycrystalline film.

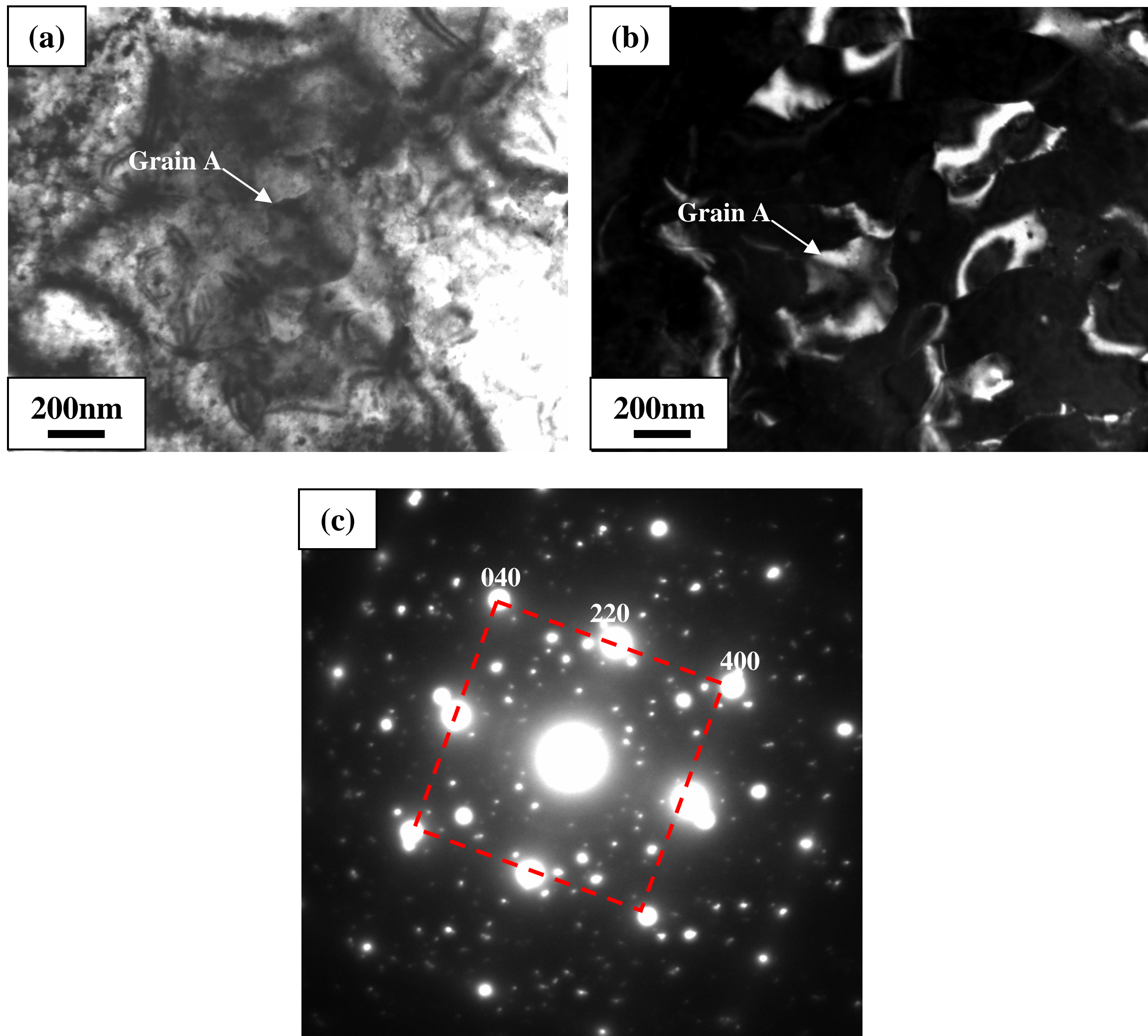

Figure 5.3 Strain contrast is observed in (a) bright field and (b) dark field images with the corresponding SAED pattern in (c) showing Si and NiSi reflections.

Figure 5.3 (a) represents the bright field image with the corresponding dark field image of the NiSi film. A polycrystalline film with large randomly oriented as well as irregular shaped grains is observed. The presence of bend contours in between and within the grains, shows the evidence of a highly strained silicide film. The high degree of strain is to be expected since NiSi and Si possess different crystal structures and lattice parameters. NiSi exhibits the orthorhombic MnP crystal structure with a = 5.18Å, b = 3.34Å and c = 5.72Å and space group P*nma*, whilst Si exhibits the cubic diamond crystal

structure with a = 5.4309Å[2]. In addition, when comparing the thermal expansion coefficients of silicon (2.6 ppm/°C) and the typical value for silicides (10 ppm/°C)[3], it is clear that the thermal expansion in NiSi is significantly larger. This will lead to increased interfacial strain.

Figure 5.3 (c) shows the spot diffraction pattern of the NiSi polycrystalline film rather than a ring pattern as shown in case of as-deposited Ni film on Si (100). This is attributed to the larger grain size of approximately 200nm, in the polycrystalline NiSi film. In comparison with the smaller grains size (~8nm) for the Ni as deposited, there are much fewer randomly oriented NiSi grains to contribute to a ring diffraction pattern. But instead, Figure 5.3 (c) shows a diffraction pattern that consists separate spot diffraction patterns from the large single crystalline NiSi grains.

Further analysis using a smaller selected area aperture to form diffraction patterns, revealed that the grains in the NiSi film have different orientations with respect to the Si (100) substrate. Figure 5.4 shows the two examples of SAED patterns taken of two different NiSi grains. By indexing the SAED patterns, the following crystallographic relations of the grains can be deduced:

1. From Figure 5.4 (a): NiSi [1 $\bar{3}$ 1] // Si [100]
2. From Figure 5.4 (c): NiSi [010] // Si [100]

The experimental data was verified with simulated diffraction patterns using the Electron Microscopy Software Java (JEMS) version 1.3402W2003. In the SAED patterns, the large number of diffraction spots in positions forbidden by the NiSi space group is attributed to the effects of multiple diffraction (Refer to Appendix section A.4 and A.5 for detailed indexing).

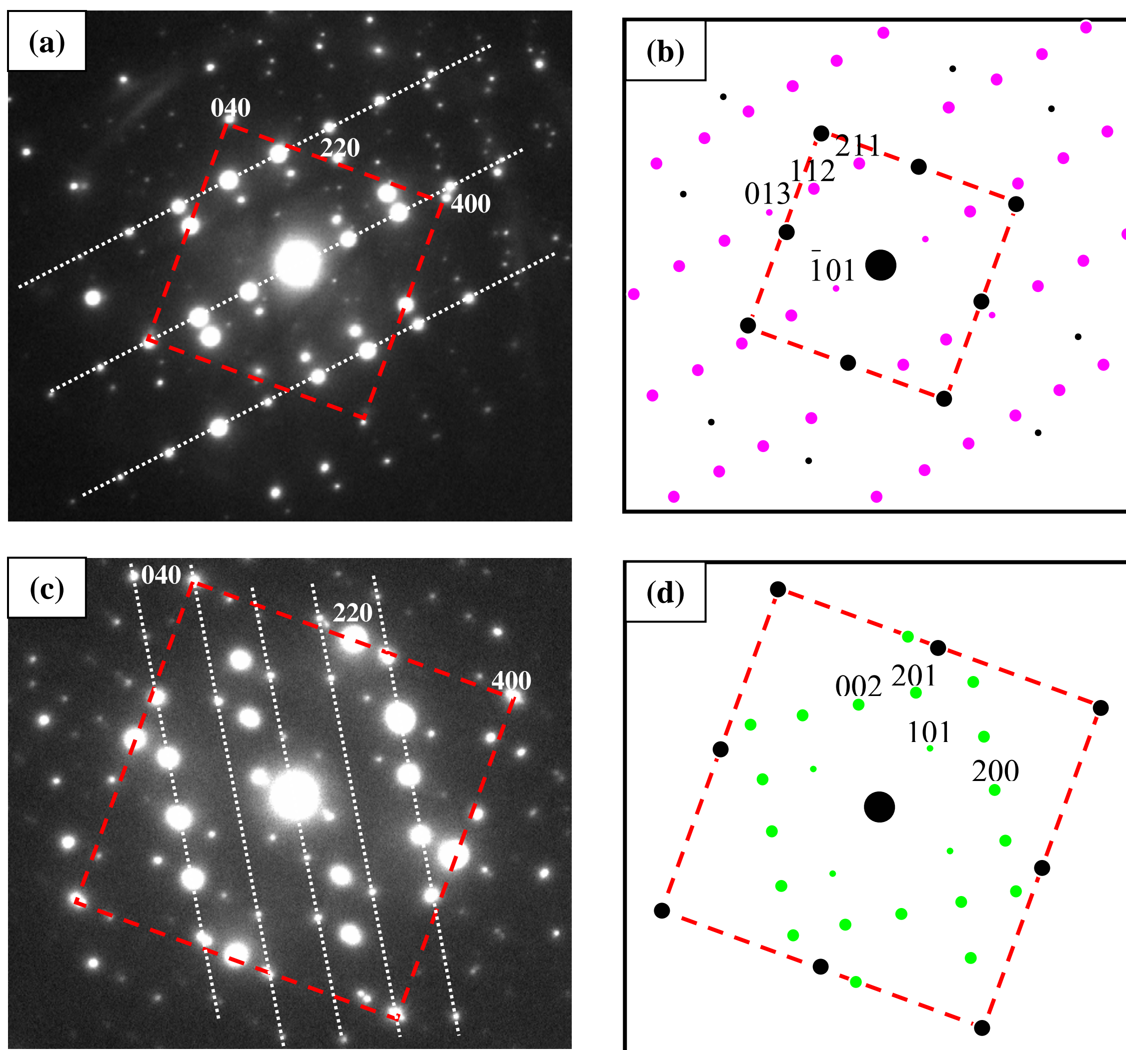

Figure 5.4 The SAED patterns in (a) and (c) show an example of two different orientation of NiSi grains with respect to the Si (100) substrate. The red and white dotted line in the both the SAED patterns represents the reflections of the Si and NiSi phase respectively. Simulated diffraction patterns indexed with NiSi reflections are shown in (b) and (d) respectively.

During further heating in the temperature range 400-500ºC, some grain growth was observed, the average grain size increasing from ~200nm at 300ºC to ~300nm at 450ºC. Voids then began to appear in the film as shown in Figure 5.5 (a), by a process of grain boundary thermal grooving[4,5] (as determined by an increase in the intensity of electron transmission through the grain boundary regions). In Figure 5.5 (b), void growth starts to occur through liquid-like (capillary) agglomeration.

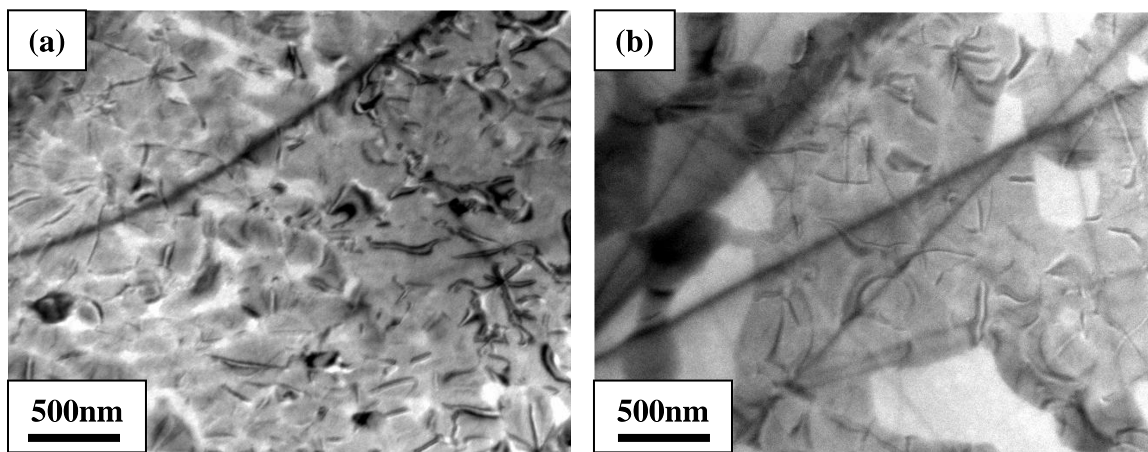

Figure 5.5 Thermal grooving starts to occur at grain boundaries in (a) indicating the onset of agglomeration. This is followed by liquid-like void growth exposing the Si substrate in (b) at 400-500ºC.

The observations were consistent with the model of Jiran and Thompson for the agglomeration of thin films of Au on fused silica[6], where the agglomeration process was shown to be dependent on the ratio (L_c/X) where L_c is the critical grain size and X is the film thickness (as discussed in section 2.3.2). The film now comprised isolated islands of NiSi, as may be seen from the bright field images in Figure 5.5 (b). The formation and agglomeration of NiSi at this temperature is consistent with a number of previous reports where annealing of Ni/Si (100) was studied using techniques such as *in-situ* X-ray diffraction, *in-situ* ellipsometry as well as ex-situ TEM. (see example Olowolafe *et al.*[7], d'Heurle *et al.*[8], Julies *et al.*[9], Tinani *et al.*[10]).

Upon heating the sample to ~550°C, agglomeration becomes more severe and dynamic observations of the later stages of this process was captured by video recording and are presented as the series of video images in Figure 5.6. These images were taken at approximately 1 second between the frames presented. During this interval, the islands continue to break up, as may be seen by comparison of area 'X' in both images in Figures 5.6 (a) and (b).

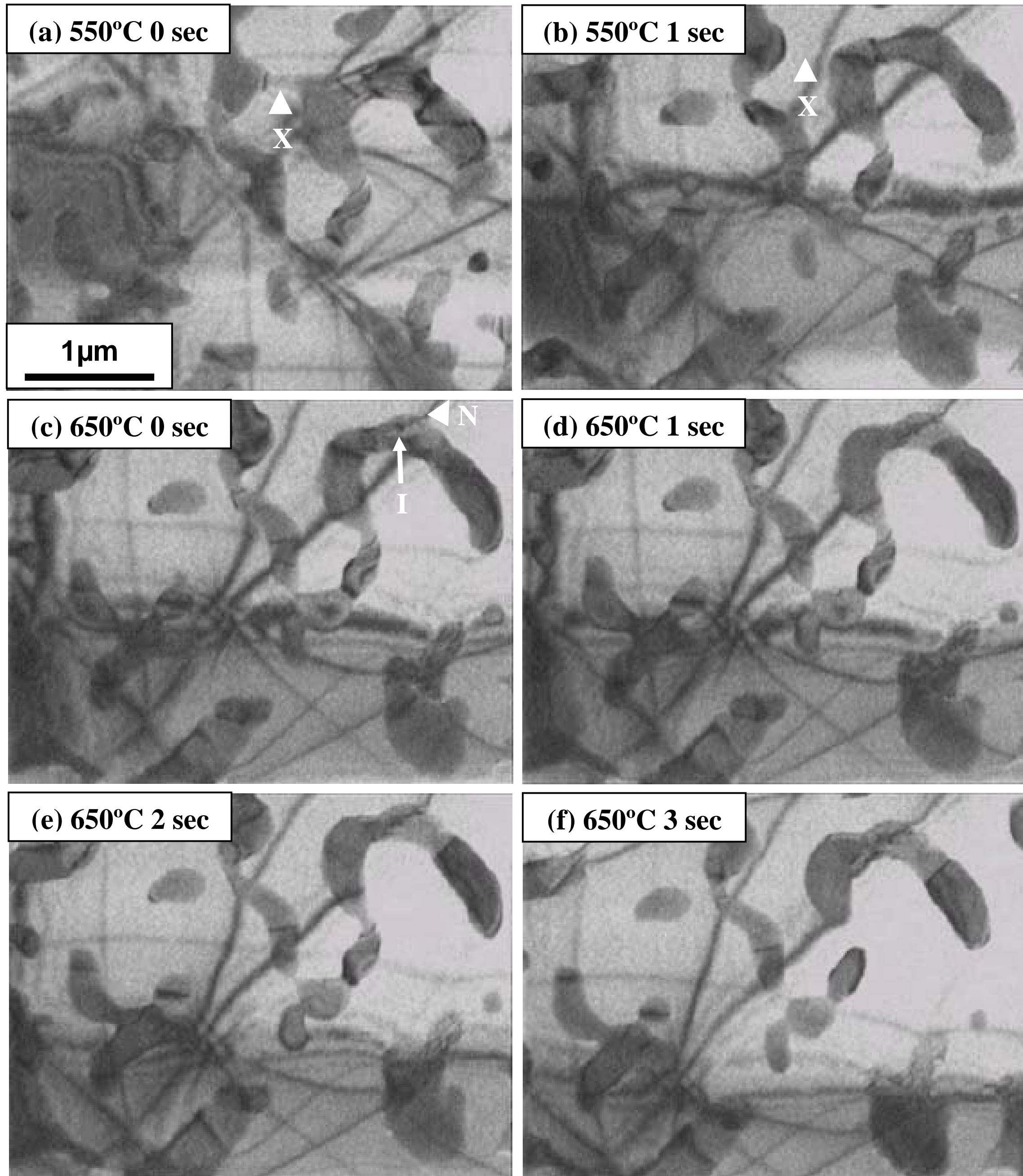

Figure 5.6 Showing severe agglomeration occurring in (a) and (b). The nucleation of the new phase was observed at 'N' in (c) and seen in (d) and (e) propagating through island 'I' until the reaction terminates in (f).

During further annealing of the sample to 650ºC, attention was focused on the island marked 'I' in Figure 5.6 (c). The nucleation of another phase was observed to

occur at the edge of the island, in the location marked ‘N’. The newly formed interface propagated laterally across the entire width of the film, thereby forming two distinct grain boundaries. The two boundaries then propagated through the NiSi island in opposite directions until the configuration shown in the bright field image of Figure 5.6 (f) was attained.

The transformation of this island terminating with two-grain boundaries is further illustrated in Figure 5.7. The red dotted line represents the movement of the grain boundaries as it propagated through the island during the reaction, with the time scale indicated. With reference of Figure 5.7 (a), mass-thickness contrast before nucleation suggested that the region of NiSi at the extreme right-hand end of this island in area A was of greater thickness than the remainder of the island. The nucleation of the new phase was therefore observed in the thinner portions of the film indicated by area N. Following nucleation at the island edge, the reaction front was observed to rapidly propagate across the entire width of the island; the two phase boundaries formed propagated in opposite directions through the island, Figures 5.7 (b) - (e), at a rate of ~100nms^{-1}. Their motion was rapidly arrested as they approached the ends of the island, at the stage shown in Figure 5.7 (f). At this point, mass-thickness contrast indicated that the two ends of the island have further agglomerated to form thicker regions in comparison to the other regions of the island.

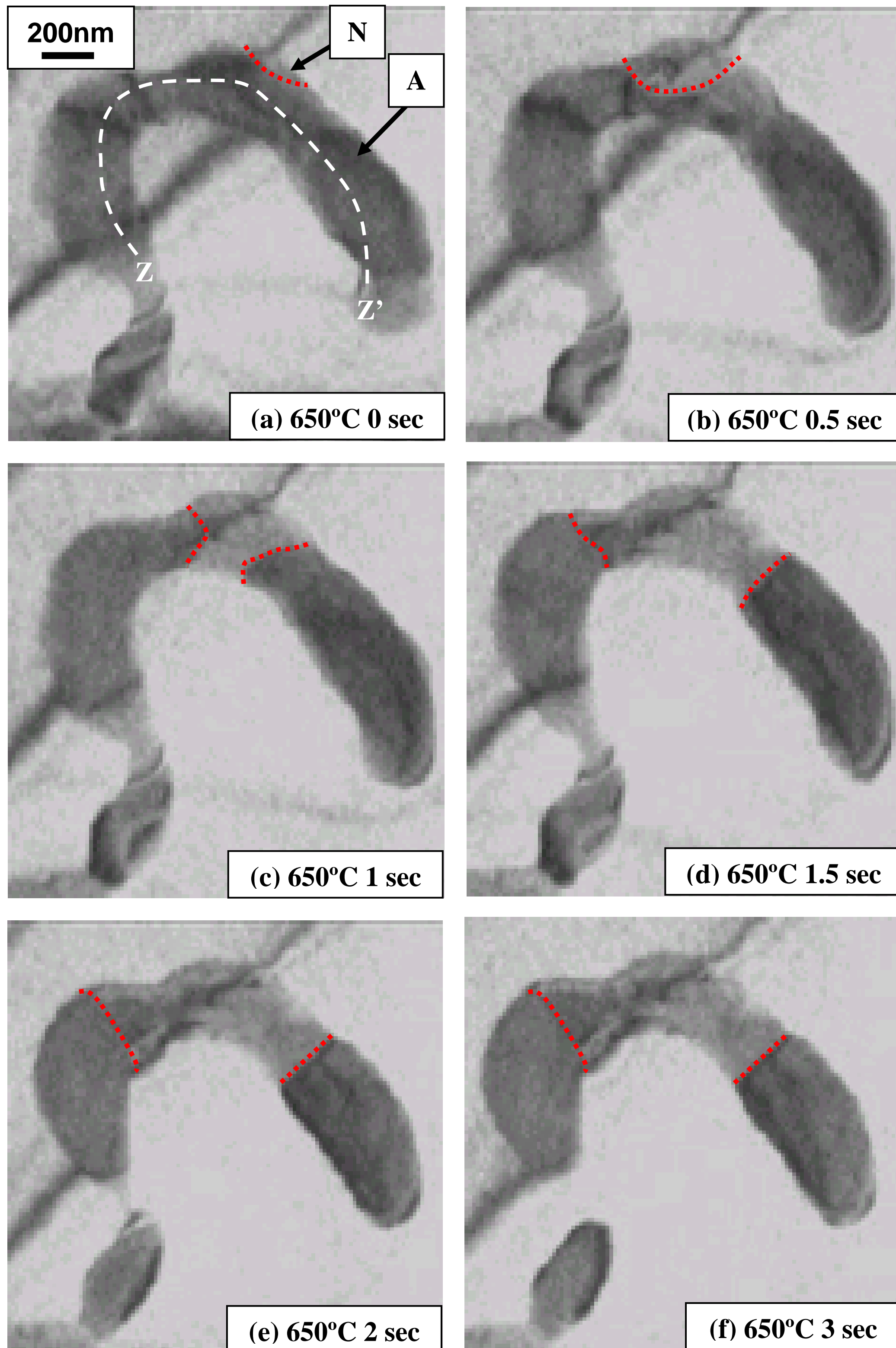

Figure 5.7 Images (a) - (e), captured from a video recording, illustrate the transformation of island 'I' into an island with two grain boundaries. The time scale of the movement of the boundaries (indicated by the red doted lines) as it propagates through the island is presented in the images.

At this stage, SAED patterns taken from the either side of the grain boundaries showed that a NiSi:$NiSi_2$ interface existed at that moment as presented in Figure 5.8. Therefore two distinct regions of NiSi remain, bounding a central portion of $NiSi_2$ within island 'I'. The arresting of the boundary propagation is likely to be a consequence of the interfacial tension associated with the increased width of the island, in combination with an increased thickness of the NiSi phase as it agglomerates.

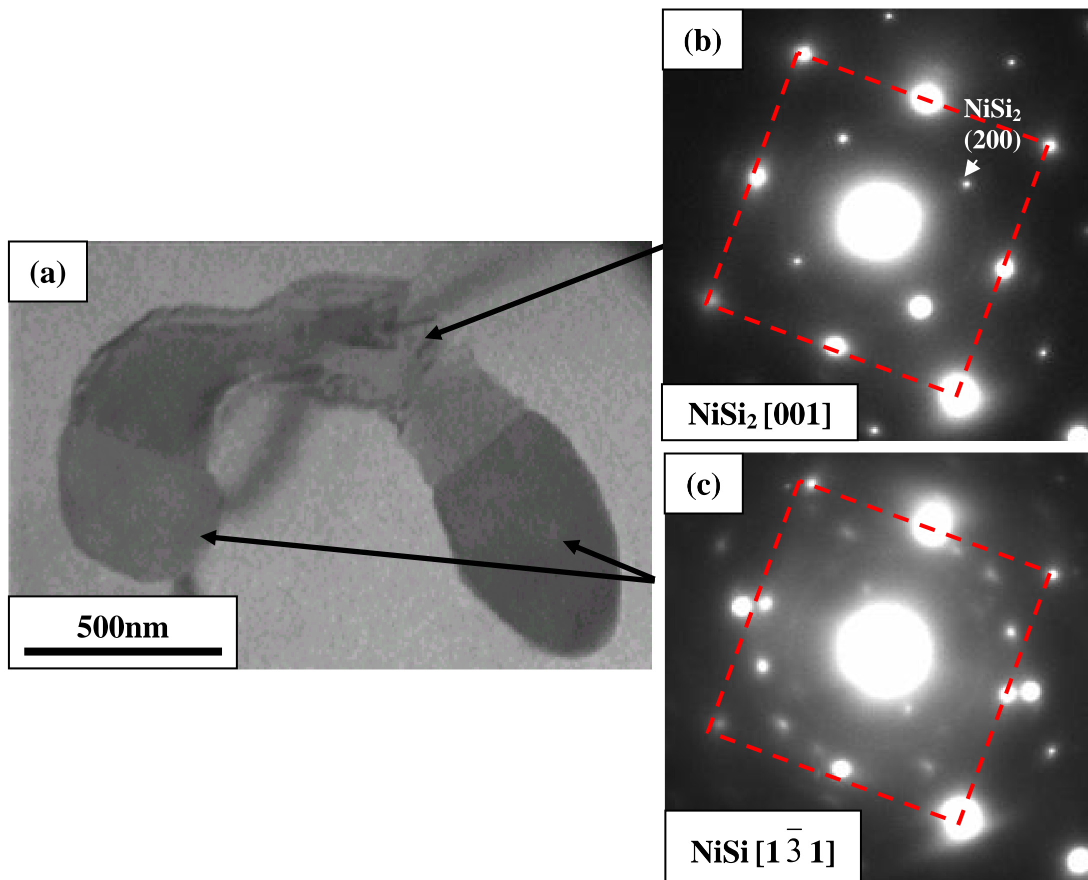

Figure 5.8 The bright field image in (a) shows the NiSi:$NiSi_2$ interface existing in a single island at 650º. SAED taken at either side of the grain boundary indicates the presence of the $NiSi_2$ and NiSi phase in (b) and (c) respectively.

The sample temperature was further increased to ~700ºC, and the projected area of each of the NiSi regions was observed to slowly increase (implying lateral diffusion of Ni). No further transformation to $NiSi_2$ was observed during this expansion. The law of conservation of material implies that the NiSi portions were decreasing in thickness (Figures 5.9 (a) - (b)). In the case of the island labeled 'I', an increase in area of approximately 27% was measured over a period of 30 minutes. Following this expansion, the NiSi:$NiSi_2$ interface finally resumed propagation through the remainder of the film (Figures 5.9 (c) - (g)). The island was thus transformed entirely to $NiSi_2$. No grain boundaries could be identified within the island, implying the island was entirely single crystalline. Due to the small lattice mismatch (~0.4%), the $NiSi_2$ phase exhibits a cube on cube epitaxial orientation with $NiSi_2$ (100) // Si (100), $NiSi_2$ [100] // Si [100].

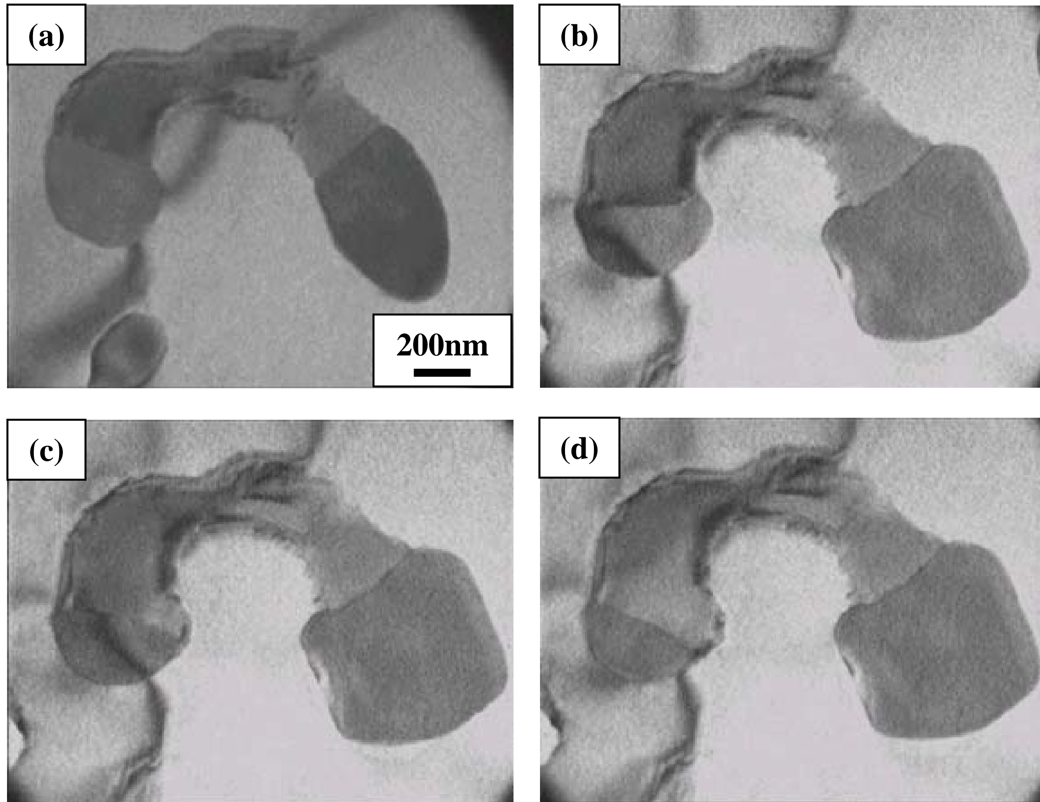

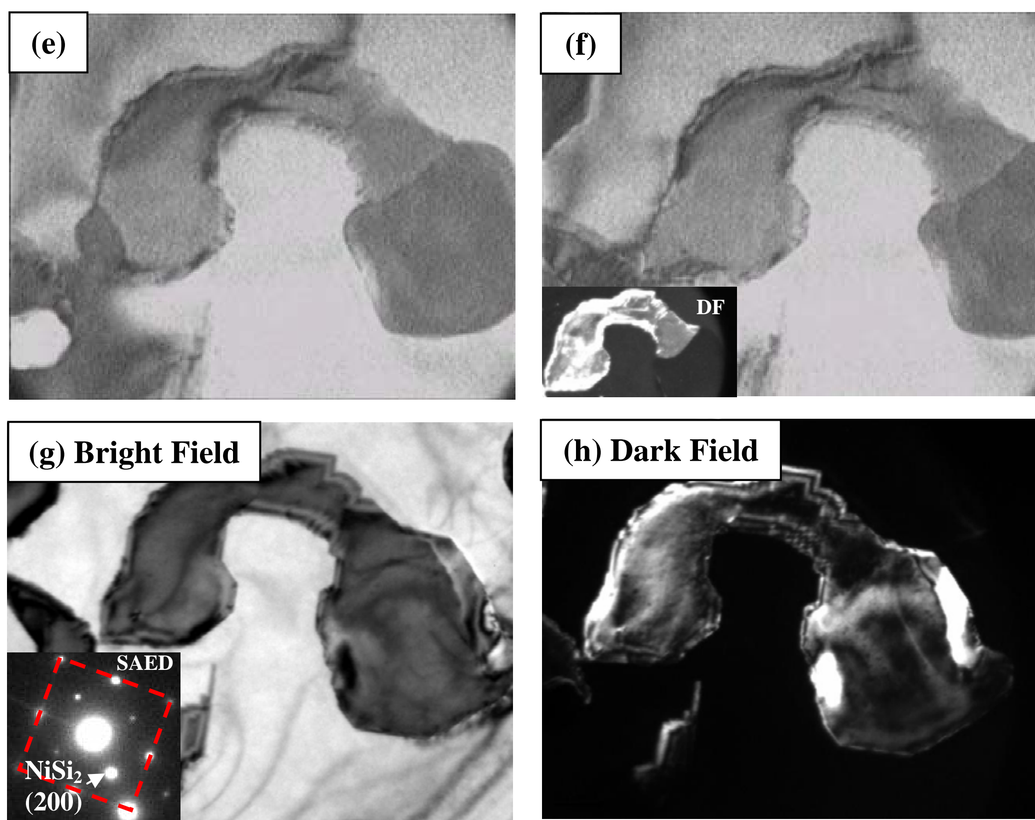

Figure 5.9 Images (a) to (b) outline the stages of the expansion of the NiSi portions of island 'I'. This is followed by the propagation of the NiSi:$NiSi_2$ interface at one end of the island, until the whole NiSi portion is transformed into $NiSi_2$ as shown in images (c) - (f). The dark field image in (f), was imaged using the $NiSi_2$ (200) reflection and outlines the partially formed $NiSi_2$ Island. The images in (g) and (h) represent the SAED pattern, bright and dark field images of the fully transformed $NiSi_2$ island 'I'.

In summary, the situation is illustrated schematically in Figures 5.10 (a) - (e). The nucleation of $NiSi_2$ and propagation through the island shown in Figures 5.7 and 5.9 is represented in cross-section in Figures 5.10 (a) - (e). The diagrams are drawn with respect to the line Z-Z' superimposed on the island 'I' of Figure 5.7 (a). Initial nucleation is observed to occur at the triple junction between the Si substrate, the NiSi island and vacuum, in the thinner region of the film (Figures 5.10 (a) and (b)). The NiSi:$NiSi_2$ phase boundary subsequently propagates through the NiSi film until the boundary approaches the ends of the island, at which stage propagation was observed to be arrested (Figure 5.10 (c)).

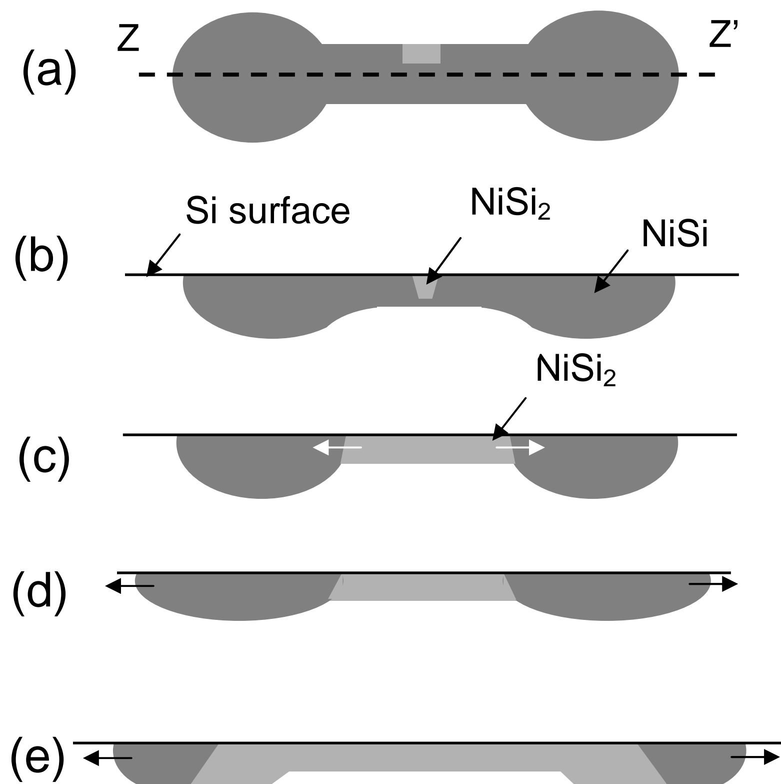

Figure 5.10 Schematic diagram of the transformation from NiSi to $NiSi_2$ of the island 'I' shown in Figure 5.7 (a). The diagram is drawn with respect to the fiducial line Z-Z' drawn on island 'I'. (a) Plan view representation of the initial $NiSi_2$ nucleation of NiSi, and cross-sectional representations of (b) initial $NiSi_2$ nucleation, (c) propagation of the NiSi:$NiSi_2$ phase boundaries laterally through the island, (d) lateral expansion of the NiSi regions, and (e) completion of the propagation of the NiSi:$NiSi_2$ phase boundaries through the remainder of the island.

Then the temperature was increased to ~700ºC, and the projected area of each of the NiSi regions was observed to slowly increase. Following this expansion, the NiSi: $NiSi_2$ interface finally resumed propagation through the remainder of the film (Figure 5.10 (e)). The island was thus transformed entirely to $NiSi_2$.

The reaction NiSi + Si → $NiSi_2$ is known to result in a total volume contraction of ~12%[11]. Associated with this contraction there will be an increase in the strain energy of the system, and this will introduce an additional barrier to the nucleation of $NiSi_2$.

Considering the free energy change ΔG upon formation of a nucleus of $NiSi_2$, of radius r, we may write:

$$\Delta G = - ar^3 \Delta G_v + br^2 \gamma_i + E_{el} \qquad (1)$$

where a and b are geometrical factors related to the shape of the nucleus ($a=4/3\pi$, $b=4\pi$ in the case of a sphere), ΔG_v is the volume free energy change upon transformation to the disilicide phase, γ_i is the interfacial energy at the NiSi: $NiSi_2$ boundary and E_{el} is the elastic strain energy induced by the volume contraction upon formation of $NiSi_2$.

It has been suggested that the strain induced in the film due to the volume contraction may be most efficiently relieved (minimized) at or close to the free surface of the film[12], where surface relaxation can more readily occur, as compared with a more deeply buried region of the interface. Since the NiSi film breaks up into the form of discrete islands prior to disilicide formation, nucleation of $NiSi_2$ might therefore be expected to occur at the NiSi:Si interface close to the free surface. This is indeed consistent with the plan-view observations described above.

Furthermore, nucleation is observed to occur preferentially in the thinner regions of islands of variable thickness. The surface strain relief mechanism proposed for initial $NiSi_2$ nucleation will be enhanced in thin regions since the volume shrinkage of the island will occur closer to the free surface. We note that, in competition with this, the overall surface area: volume ratio of the $NiSi_2$ nuclei will be higher in thinner (more shallow) regions. However, the $NiSi_2$ nuclei will be bounded primarily by either Si or free surface (vacuum), with the NiSi:$NiSi_2$ interface being a relatively small fraction of the total

surface. $NiSi_2$ exhibits the CaF_2 structure which is similar to the diamond cubic structure of Si, the $NiSi_2$ lattice parameter being ~0.5% smaller than that of Si. The interfacial energy may therefore be expected to be substantially lower than that between NiSi and $NiSi_2$. This assertion is supported by the fact that sharp, planar interfaces are typically observed between $NiSi_2$ and Si in cross-sectional TEM image[12,13] (refer to Figure 5.11).

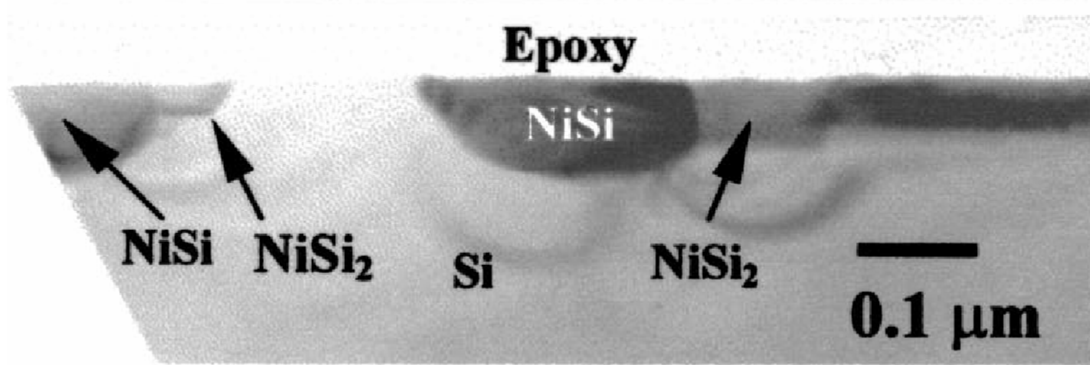

Figure 5.11 Reproduced from Wong *et al.* showing the cross-sectional TEM image of NiSi and $NiSi_2$ on Si (100) at 700ºC. The image outlines the sharp faceting between the $NiSi_2$ island and the Si.

In comparison to earlier works where a thicker Ni film (~ 200nm) was deposited on Si (100), the reported nucleation temperature for $NiSi_2$ was approximately 800ºC, which is much higher when compared to 650ºC, the observed temperature for this experiment. By depositing thick Ni films (>100nm), the agglomeration for the NiSi film was absent even at temperatures just below the nucleation temperature of $NiSi_2$ (see section 2.3.2). Therefore the triple junction of the NiSi, Si and vacuum ceased to exist in this system and the nucleation of $NiSi_2$ occurred only at the NiSi-Si interface. This would increase the nucleation energy barrier ΔG, as the contribution of the elastic strain energy, E_{el}, induced by the volume contraction upon formation of $NiSi_2$ becomes more significant with a much higher nucleation temperature of $NiSi_2$ in comparison with this study.

5.2 Ni film on oxide-covered Si (100)

5.2.1 Preliminary inspection of oxide-covered Si (100)

Figure 5.12 (a) shows an EELS spectrum, Figure 5.12 (b) a bright field image, and Figure 5.12 (c) the corresponding SAED pattern where the experiment was carried out. The EELS spectrum is shown without the Si edges, to emphasize the oxygen K edge at 532eV energy loss, arising from the oxide layer with the absence of carbon K edge.

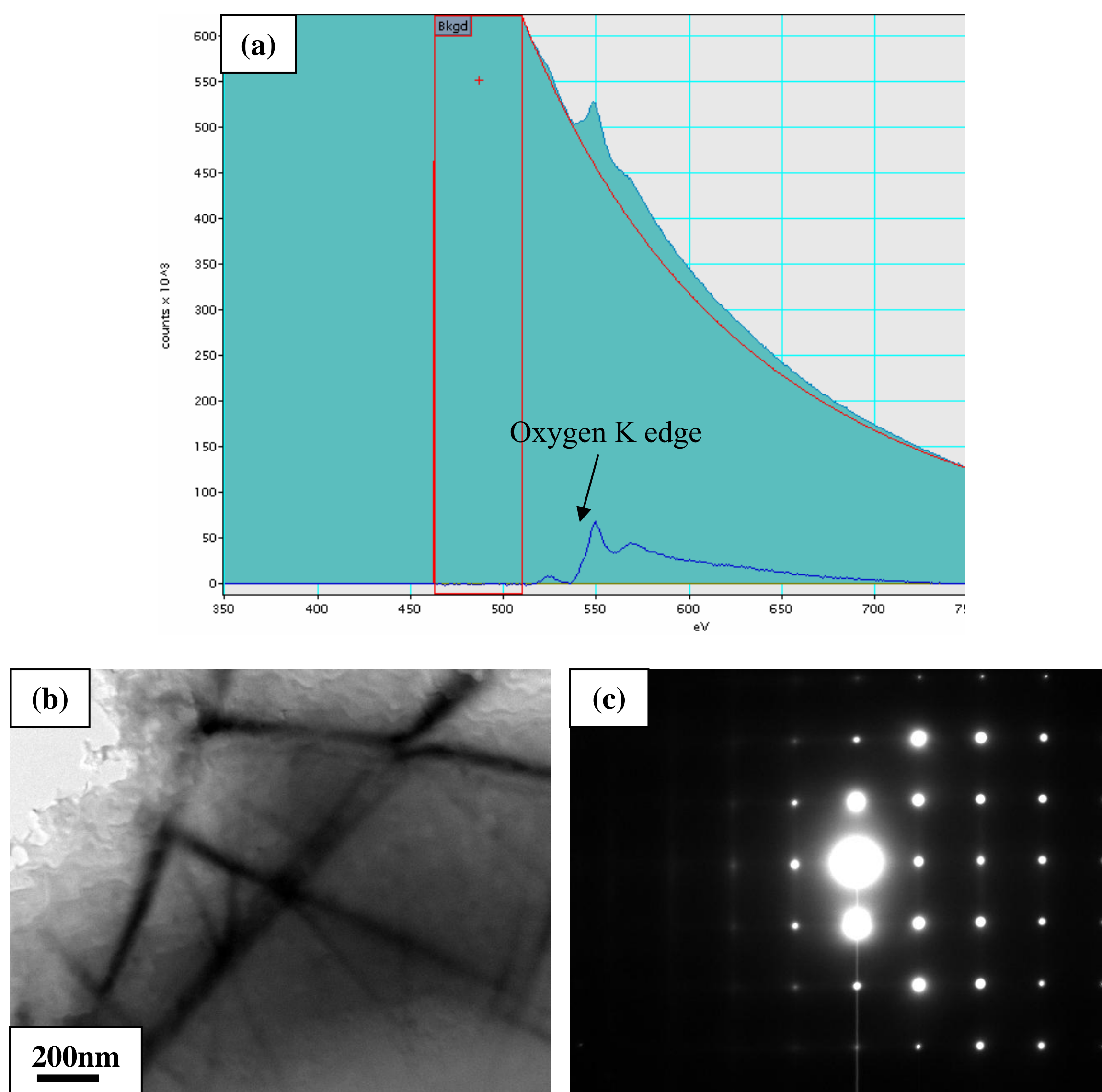

Figure 5.12 (a) EELS spectrum showing the oxygen K edge at 532eV, (b) bright field image and (c) SAED of an oxide-covered Si (100).

5.2.2 Nickel deposition on oxide-covered Si (100)

After the preliminary inspection of the oxide-covered Si (100) substrate, 12nm of Ni was deposited on the oxide-covered Si (100) surface. The deposition conditions used are described in section 4.4. Uniform coverage of the substrate was achieved, with a Ni film of average grain size of ~8nm, as observed in the bright field image in Figure 5.13 (a). The SAED pattern shows rings corresponding to the polycrystalline Ni film and spots of the [100] oriented Si substrate. Additional rings are attributed to the effects of multiple diffraction. Note that the (200) and (020) reflections, forbidden for the Si structure, do not appear in the diffraction pattern.

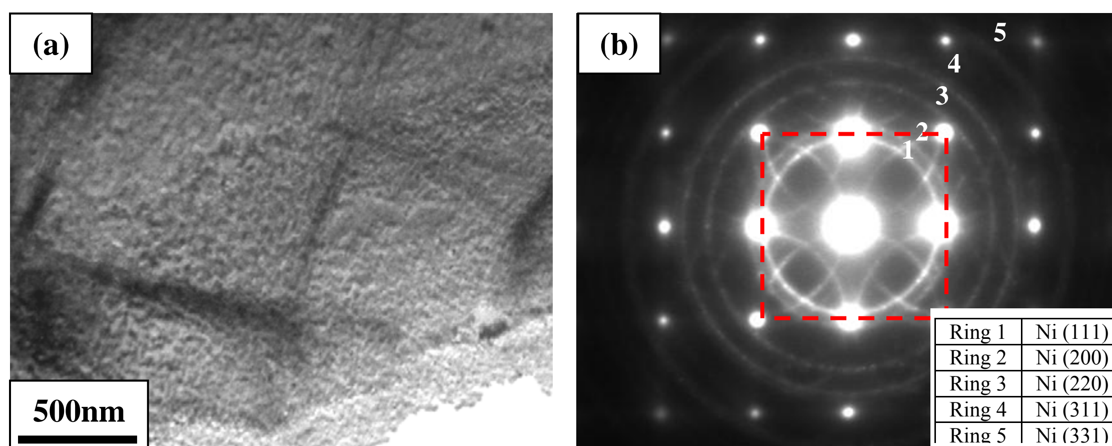

Figure 5.13 Corresponding (a) bright field images and (b) SAED for as deposited 12nm Ni on oxide-covered Si (100).

5.2.3 Annealing of the 12nm Ni film on oxide-covered Si (100)

The sample was heated at a rate of 30ºC per minute from room temperature to 200ºC. No evidence of an obvious reaction was observed until an annealing temperature of 200ºC was attained. The changes were found in the SAED patterns as represented in Figure 5.14 (a). Faint diffraction spots at the (200) and (020) positions appeared, showing that epitaxial $NiSi_2$ starts growing as the first silicide to be formed in this experiment. In

addition, the ring pattern corresponding to the Ni film became discontinuous. The bright field image in Figure 5.14 (b) still resembles the morphology of the as-deposited polycrystalline Ni film, showing the presence of unreacted Ni.

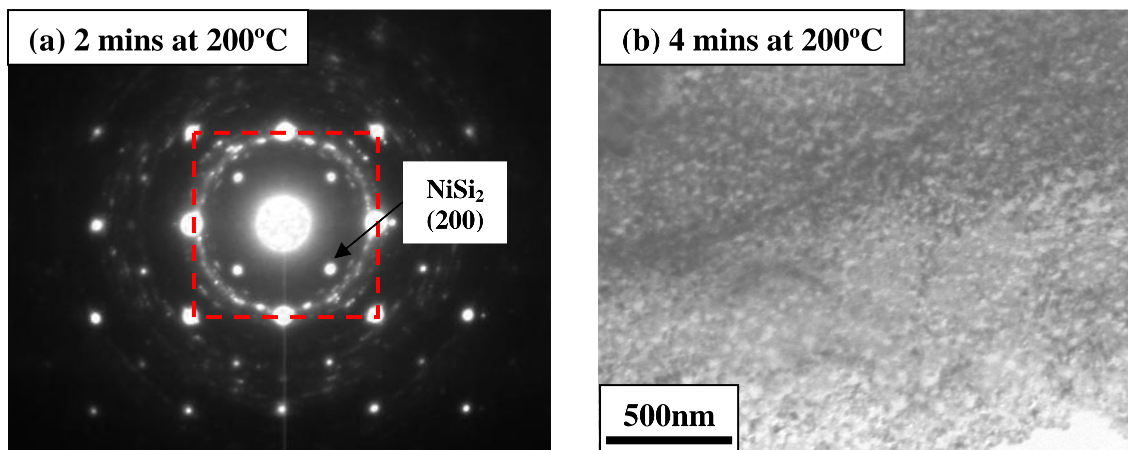

Figure 5.14 SAED (a) and bright field image (b) of sample heated to 200ºC, showing the formation of $NiSi_2$ with some unreacted Ni. The red dotted line in the SAED represents the Si (100) reflections.

By keeping the sample at 200ºC for another six minutes, more changes started to appear in the TEM images leaving a "wrinkled" like contrast as shown in Figure 5.15 (a). The corresponding SAED pattern is given in Figure 5.15 (b). By comparison with Figure 5.14 (a), it was clearly observed that the unreacted Ni layer had been completely consumed and newly appeared diffraction spots revealed the formation of a new phase. Indexing the diffraction pattern in Figure 5.15 (a) revealed that at this stage NiSi and $NiSi_2$ coexisted in the silicide film (Refer to Appendix section A.6 for detailed indexing). The crystallographic relation was deduced to be:

(1) $NiSi_2$ [100] // Si [100], $NiSi_2$ (200) // Si (400)

(2) NiSi [$\bar{1}$02] // Si [100], NiSi (020) // Si (220)

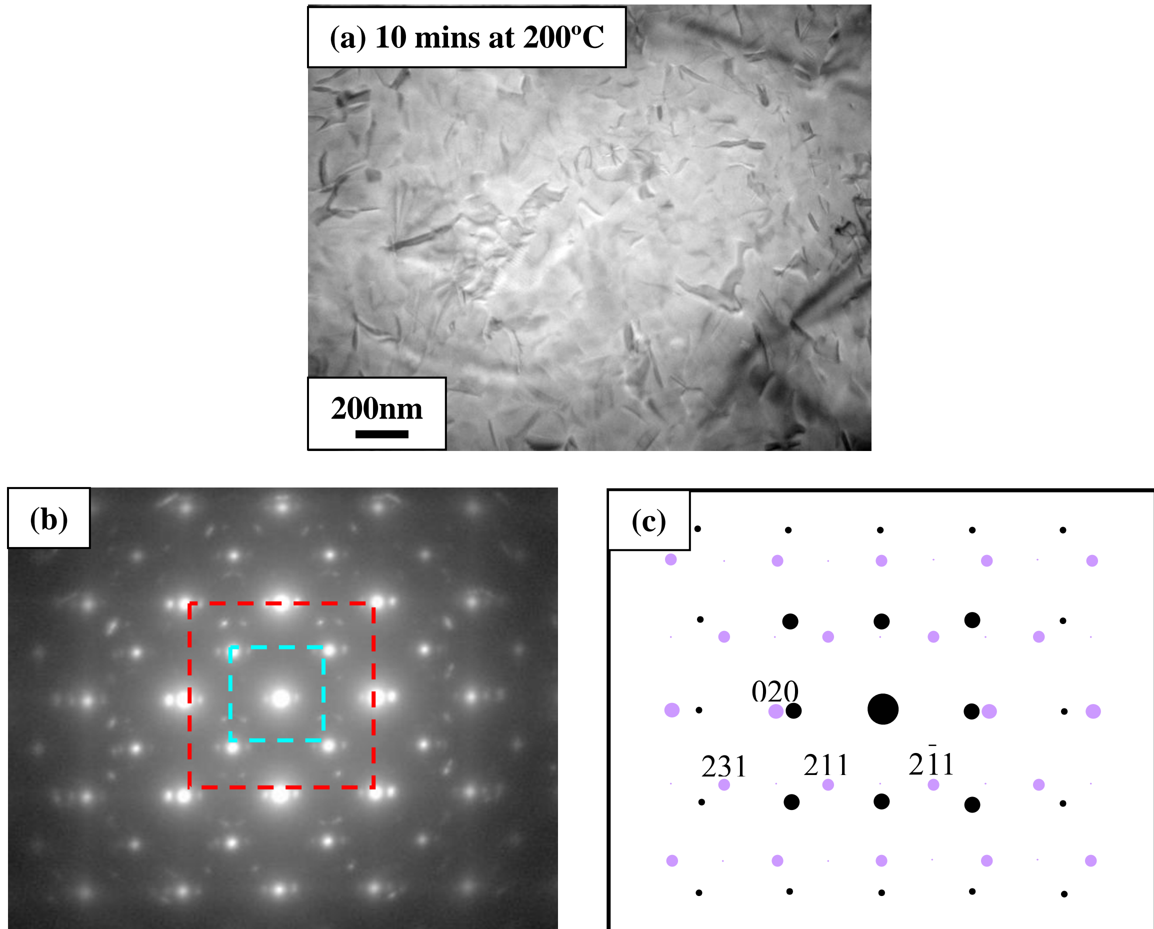

Figure 5.15 The bright field image in (a) represents the morphology of the sample after ten minutes at 200ºC. The corresponding SAED pattern in (b) shows the formation of NiSi. The red and blue dotted line represents the (100) Si and $NiSi_2$ reflections respectively. The simulated electron diffraction in (c) shows the diffraction pattern of the [$\bar{1}$02] NiSi zone axis (in purple spots).

This observation is in good agreement with a previous in-situ TEM study by Teodorescu *et al*[14]. It was shown that formation of the disilicide phase as the first phase, occurred at low temperatures due to the presence of a thin chemical oxide between the Ni and silicon substrate. Similarly, Tung *et al.*[15] and Kleinschmit *et al.*[16] reported the growth of epitaxial $CoSi_2$ on Si (100) using the oxide-mediated epitaxy method at temperatures between 500-700ºC. It was explained that the oxide layer acted as a diffusion barrier to mediate the flow of Co atoms through oxide to the Si surface so that only Si-rich silicide phases can be formed.

In the case of Ni on a clean Si (100) surface, the formation of the disilicide phase from the reaction of NiSi with Si at 650ºC was observed to be nucleation-controlled due to the contribution of the elastic strain energy, E_{el}, induced by the volume contraction upon formation of $NiSi_2$. An oxide layer between the Ni and Si allows the direct formation of $NiSi_2$ without going through any intermediate phases. This removes the elastic strain energy contribution, E_{el}, towards the energy barrier of the nucleation of $NiSi_2$. The change in free energy for this reaction becomes proportional to $\Delta G_1(NiSi_2)$ which leads to a smaller ΔG^*. Therefore the reaction ceases to be nucleation-controlled and allows the possibility for nucleation of the disilicide phase at low temperatures (see section 2.3.1).

Further heating of the sample produced no apparent changes, with the $NiSi_2$ and NiSi phases still coexisting. At temperatures higher than 650°C, the NiSi phase was found to be completely consumed to form only $NiSi_2$. This is obvious in the diffraction patterns (Figure 5.16 (a)), but also in the bright field image of Figure 5.16 (b). This image shows clear $NiSi_2$ grains with the presence of voids in some parts of the sample. The $NiSi_2$ grains appeared to look like rectangles or squares. This is due to the characteristic inverted-pyramidal shapes of the $NiSi_2$ grains[17]. The tip of the pyramid with four (111) facets is buried below the sample surface. The sides of the base of the pyramid lie along Si<110> directions, in the plane of the substrate surface. When the pyramids grow, they can form truncated pyramids with rectangular bases.

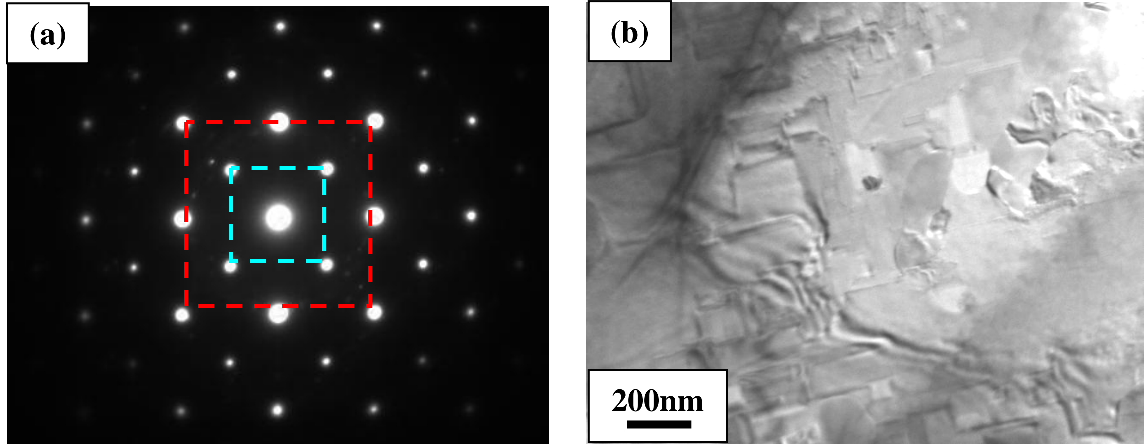

Figure 5.16 At 650ºC, the NiSi phase was consumed to form solely the $NiSi_2$ phase as presented in the (a) SAED and (b) bright field image. The red and blue dotted lines represent the Si and $NiSi_2$ reflections respectively.

5.3 Summary of Chapter 5

In this chapter two sets of experiments were carried out, namely *in-situ* deposition and annealing of 12nm Ni films on clean and oxide-covered Si (100). For the experiment of Ni on clean Si experiment, a uniform and pinhole-free but highly strained polycrystalline thin NiSi film was formed at 300ºC. The onset of agglomeration of the NiSi film was observed at a temperature range of 400-500ºC becoming more severe at higher temperatures to form isolated NiSi islands. The nucleation of $NiSi_2$ was first observed at 650ºC, occurring at the edges of the NiSi islands, at the free surface of the substrate. A NiSi:$NiSi_2$ interface was observed to propagate across the island and its movement was arrested just before it reached at the ends of the island. At this stage a NiSi:$NiSi_2$ grain boundary existed within the island. Increasing the temperature to 700ºC completed the transformation of the entire island to $NiSi_2$. Our observations are understood from a consideration of the reduction in the free energy barrier for nucleation

of $NiSi_2$ at the free surface of the film where enhanced strain relaxation can occur, in contrast to a location along the buried NiSi:Si interface.

During the *in situ* annealing of Ni on oxide-covered Si (100), epitaxial $NiSi_2$ was the first silicide phase to form at 200ºC. By keeping the sample at this temperature, the unreacted Ni eventually transformed to NiSi. At this stage, the coexistence of the NiSi and $NiSi_2$ phases was observed even after annealing in the temperature range of 200-650ºC. At temperatures above 650ºC, the NiSi layer was observed to be completely consumed to form entirely $NiSi_2$. Our observations suggest that the native oxide layer acts a diffusion barrier, which mediates the flux of Ni to the Si surface, promoting the nucleation of the Si-rich silicide phase of $NiSi_2$, at temperatures as low as 150ºC. The nucleation of the $NiSi_2$ phase from the direct reaction of Ni and Si excludes the contribution elastic strain energy, E_{el}, which is induced by the volume contraction when NiSi and Si reacts to form $NiSi_2$.

References:

[1] C.C. Ahn, O.L. Krivanek, R.P Burgner, M.M. Disko and P.R.Swann, *EELS Atlas (A Reference Guide of Electron Energy Loss Spectra Covering All Stable Elements)*, Gatan Inc., (1983).
[2] W.B. Pearson, *Pearson's Handbook of Crystallographic Data for Intermetallic Phases,* American Society for Metals, Metals Park, Ohio, (1985), 1770.
[3] Karen Maex, Marc Van Rossum, *Properties of Metal Silicides*, Institution of Electrical Engineers, UK, (1995), Chapt. 3.
[4] W.W. Mullins, *J. Appl. Phys.* **28(3)**, (1957), 333.
[5] T.P. Nolan, R. Sinclair and R. Beyers, *J. Appl. Phys.* **71(2)**, (1992), 720.
[6] E. Jiran and C.V. Thompson, *J. Electron. Mat.* **19(11)**, (1990), 1153.
[7] J.O. Olowolafe, M.A. Nicolet and J.W. Mayer, *Thin Solid Films* **38**, (1976), 143.
[8] F.M. d'Heurle, C.S Petersson, J.E.E Badlin, S.J. La Placa and C.Y. Wong, *J. Appl. Phys.* **55**, (1984), 4208.
[9] B.A. Julies, D. Knoesen, R. Pretorius, D. Adams, *Thin Solid Films* **347**, (1999), 201.

---

[10] M. Tinani, A. Mueller, Y. Gai, E.A. Irene, Y.Z. Hu and S.P. Tay, *J. Vac. Sci Tech B* **19**, (2001), 376.
[11] F.M. D'Heurle, *J. Mater. Res.* **3**, (1988), 167.
[12] A.S.W. Wong, D.Z. Chi, M. Loomans, D. Ma, M.Y. Lai, W.C. Tjiu, S.J. Chua, C.W. Lim and J.E. Greene, *Appl. Phys. Lett.* **81,** (2002), 5138.
[13] S.S. Lau and N.W. Cheung, *Thin Solid Films* **71**, (1980), 117.
[14] V. Teodorescu, L. Nistor, H. Bender, A. Steegen, A. Lauwers, K. Maex and J. Van Landuyt, *J. Appl. Phys*. **90**, (2001), 167.
[15] R.T. Tung, *Appl. Phys. Lett*. **68,** (1996), 3461.
[16] M. Kleinschmit, M. Yeadon, and J.M. Gibson, *Appl. Phys. Lett*. **75,** (1999), 3288.
[17] D. Fathy, O.W. Holland and J. Narayan, *J. Appl. Phys.* **58**, (1985), 295.

Chapter 6 Results and discussion II: Ni on relaxed $Si_{0.75}Ge_{0.25}$ (100)

In this chapter, the thermal reaction of a 12nm Ni film on a relaxed $Si_{0.75}Ge_{0.25}$ (100) substrate is reviewed. EELS, images and SAED data from the preliminary inspection of the cleanliness and composition of the substrate are presented in the first section. The following the section contains data obtained from the *in-situ* deposition of the Ni film on the substrate. Reactions and phase transformations during the annealing of the sample are covered in the next section. In addition to data obtained from imaging and SAED, this section includes data from EELS spectra and Energy-Filtered TEM (EFTEM) images taken at specific chosen temperatures. Elemental composition, in terms of percentage, of nickel, silicon and germanium will be quantified from the EELS spectra taken at different areas of the sample. This is to monitor the movement of the atoms as the samples are heated at the specific temperatures.

6.1 Preliminary inspection of relaxed $Si_{0.75}Ge_{0.25}$ (100)

Before the experiment, a preliminary inspection of the sample was carried out by obtaining EELS spectra, followed by SAED patterns and bright field images at different parts of the $Si_{0.75}Ge_{0.25}$ substrate. This is to observe for any obvious contaminants that may be present on the sample as well as to obtain the elemental composition of Si and Ge at the beginning of the experiment.

The EELS spectra from the substrate are shown in Figures 6.1 (a) and (b). The spectrum taken at low energy loss, in Figure 6.1 (a), shows the absence of the carbon K edge and the oxygen K edge. Using the EELS Atlas[1], the Si $L_{2,3}$ and L_1 edges are clearly indexed as shown on the spectrum. However, the Ge $M_{4,5}$ edge at 29eV is not visible as the spectrum starts at 50eV. The EELS spectrum taken at high energy loss in Figure 6.1 (b) clearly reflects the Ge $L_{2,3}$ and L_1 as well as the Si K_1. The elemental composition in atomic percent of the substrate was computed using the Gatan Microscopy Suite ™ version 1.2 software. The steps involved are as follows:

(1) The energy scale of the EELS spectrum in Figure 6.1 (b) is calibrated with the Ge L_3 and Si K_1 edges at energy loss of 1217eV and 1839eV respectively.

(2) Once this is done, the quantification program is run to calculate the elemental composition in percent (the method of calculation by the program is covered in section 4.7.2.3).

For the bare $Si_{0.75}Ge_{0.25}$ substrate the elemental composition is calculated to be Ge 25.9% and Si 74.1%, with an error of 0.9% from the specifications of the substrate.

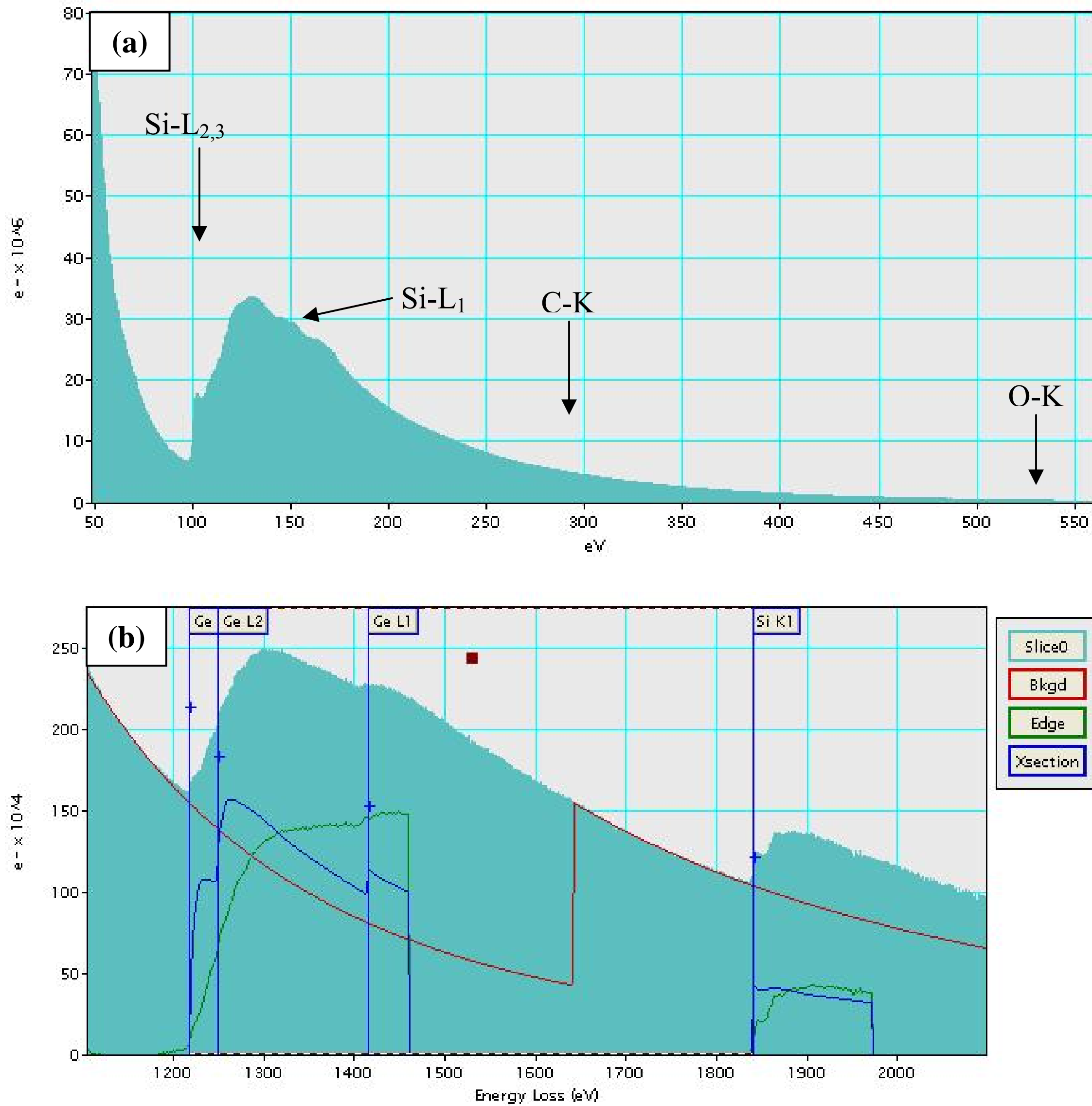

Figure 6.1 Showing the EELS spectrum taken at low energy loss in (a) with the absence of the carbon and oxygen edges. In (b), the EELS spectrum taken at higher energy loss is used to quantify the elemental composition of silicon and germanium, which was found to be 74.1% and 25.9% respectively.

The percentage error is only the statistical error in calculating the edge areas using the extrapolated background. It does not account for the systematic errors such as inaccuracies in calculated edge cross-sections, and the effect of multiple scattering. Thus absolute determination of composition is much less accurate than suggested by the error of 0.9%. The typical error for the elemental composition is ± 5 to

10 atomic percent. However relative composition (i.e. compositions of adjacent areas taken under the same conditions) can be determined much more accurately since the systematic errors are the same. Therefore, a $\frac{Ge}{Si}$ ratio of 0.35 is defined for the starting substrate and it is used a comparison with values taken at different temperatures during the reaction.

The SAED and bright field image of the $Si_{0.75}Ge_{0.25}$ substrate is represented in Figures 6.2 (a) and (b). In the SAED, there are no additional diffraction spots or rings that would arise if there were contaminants present on the sample. From the corresponding bright field image, bend contours are present in the thin areas close to the hole. To avoid additional undesirable strain due to the bending of thin foil, the focus of the experiments were in the thicker regions of the sample.

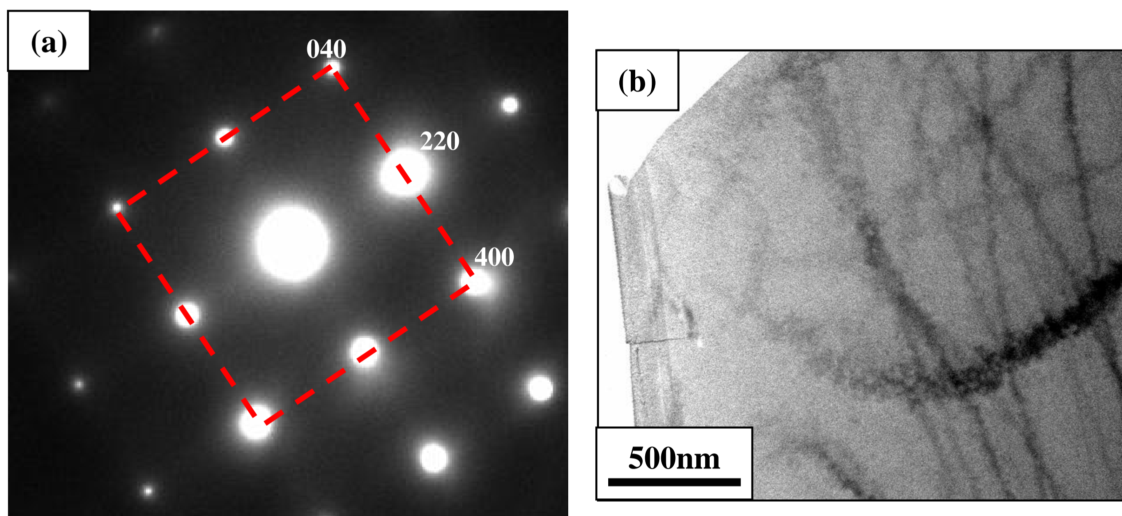

Figure 6.2 Showing (a) SAED and (b) bright field image of a clean relaxed $Si_{0.75}Ge_{0.25}$ substrate.

6.2 Nickel film deposition on relaxed $Si_{0.75}Ge_{0.25}$ (100)

Similarly to the previous two experiments, 12nm of Ni film was deposited on the relaxed $Si_{0.75}Ge_{0.25}$ substrate using the EFM3 evaporator. The conditions applied to deposit 12nm of Ni film on substrate are described in section 4.4. From the SAED pattern in Figure 6.3 (a) the polycrystalline rings that appear along with the $Si_{0.75}Ge_{0.25}$ substrate spots are from the polycrystalline Ni face-centered cubic film. Uniform coverage of the substrate was achieved, with a Ni film of average grain size ~5 to 8nm, as seen in Figure 6.3 (b). No evidence of a reaction of the Ni film with the $Si_{0.75}Ge_{0.25}$ substrate was observed.

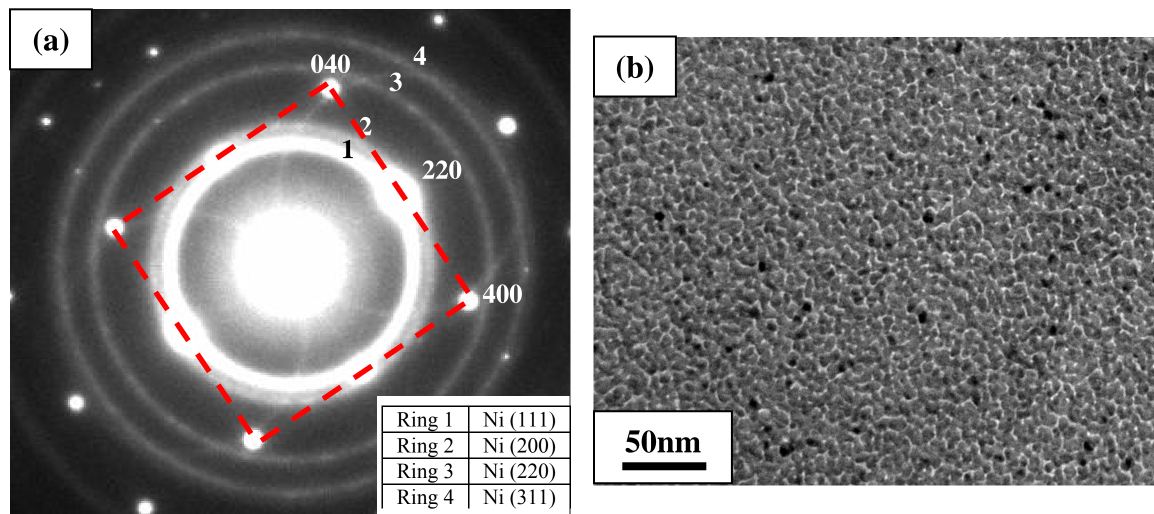

Figure 6.3 Corresponding (a) SAED and (b) bright field image of as deposited 12nm Ni on a $Si_{0.75}Ge_{0.25}$ substrate.

6.3 Annealing of the 12nm Ni film on relaxed $Si_{0.75}Ge_{0.25}$ (100)

The 12nm Ni on $Si_{0.75}Ge_{0.25}$ sample was annealed at a rate of 30ºC per minute. Results from selected area diffraction patterns show the initial reaction to form $Ni(Si_{0.75}Ge_{0.25})$ occurred at temperatures between 200 and 250ºC, as represented in Figure 6.4 (a). The presence of Ge thus appears to suppress the formation of monosilicide, which forms at temperatures 50-100ºC higher than in the case of Ni on Si (100). The reaction was obvious in TEM images (in Figure 6.4 (a)) showing the full transformation of the Ni film to form a continuous, pinhole-free polycrystalline $Ni(Si_{0.75}Ge_{0.25})$ film over the temperature range 300-350°C. The presence of bend contours in between and within the irregular grains of average grain size of ~ 200nm, shows the evidence of a highly strained silicide film, as also observed in the case of Ni on clean Si (100). Similarly, the difference in crystal structures, lattice parameters and thermal expansion coefficients between the monosilicide film and the substrate is attributed to the strain present in the silicide film.

The SAED pattern of the area is represented in Figure 6.4 (b). The reconstruction of the SAED pattern using JEMS in Figure 6.4 (c) shows that the reflections correspond closely to a super-cell of the NiSi orthorhombic phase with the MnP structure and space group *Pnma*. The crystallographic relation is: NiSi [100] // Si [100]. By definition[2], a cell, which may be used to build a crystal lattice, but which is not a unit cell, is called a super-cell. A super-cell, which is made of several unit cells, can be either commensurate or incommensurate with the unit cell. In this case, the NiSi super-cell is a commensurate super-cell with new lattice parameters:

$$a_{super\text{-}cell} = 3a_{unitcell} = 3(5.18) = 15.54\text{Å}$$

$$b_{super\text{-}cell} = 3b_{unitcell} = 3(3.34) = 10.02\text{Å}$$

$$c_{super\text{-}cell} = 3c_{unitcell} = 3(5.62) = 16.86\text{Å}$$

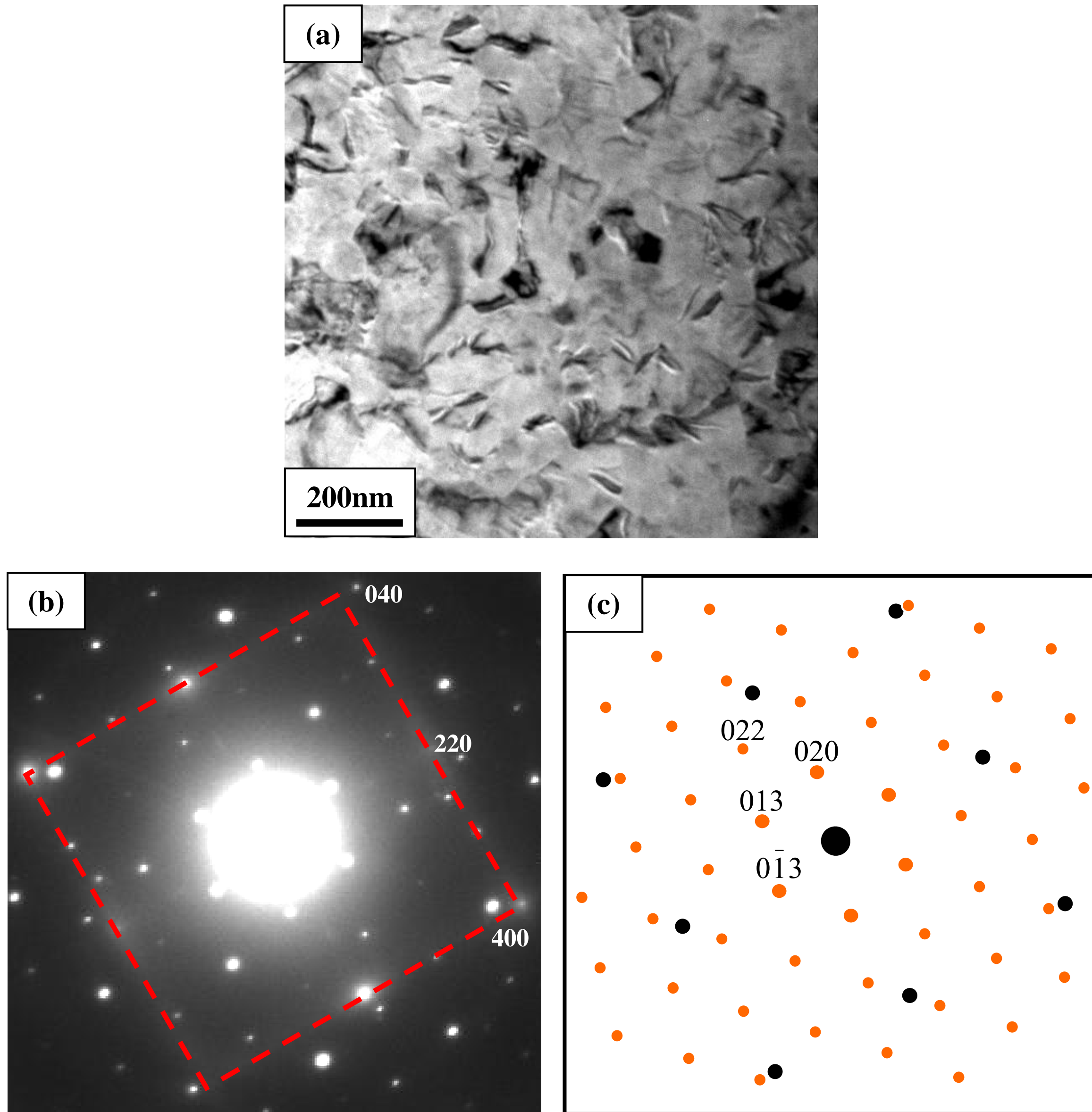

Figure 6.4 The bright field image is shown in (a) of 12nm Ni on $Si_{0.75}Ge_{0.25}$ sample at 350 ºC. The corresponding SAED in (b) is indexed with $Si_{0.75}Ge_{0.25}$ plane indices. The red dotted line represents the $Si_{0.75}Ge_{0.25}$ (100) reflections. The simulated diffraction pattern in (c) shows the matching spot pattern of a NiSi super-cell. The simulated data is indexed with NiSi plane indices.

In addition, the diffraction pattern seems to resemble a reciprocal space hexagonal crystal structure. This is due to the to the closely-matched d-spacing and the angle of approximately 60º between the diffracting planes of the orthorhombic NiSi structure along the [100] zone axis. For example, the d-spacing for the NiSi super-cell of the (020) and (013) is 5.01 Ǻ and 4.9014 Ǻ respectively and an angle of 60.71º between the two planes.

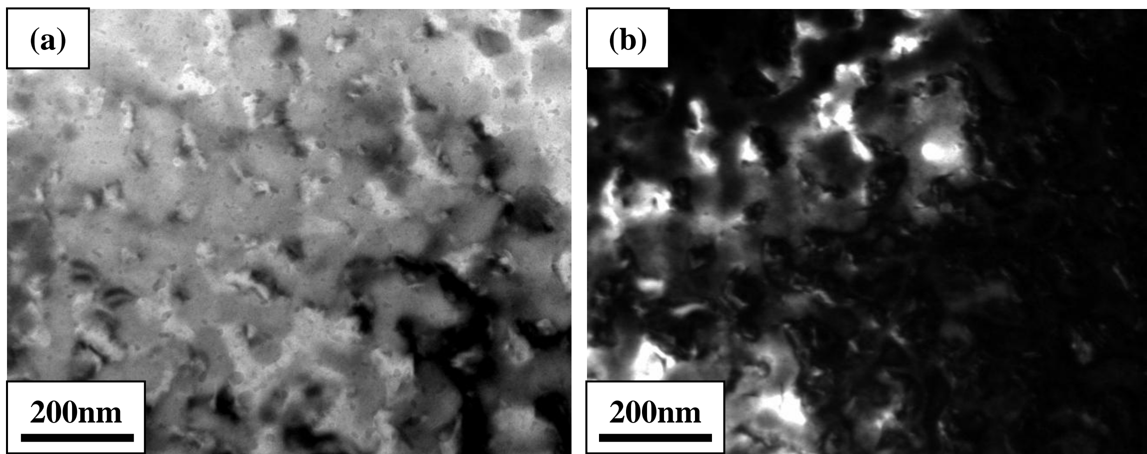

Figure 6.5 The agglomeration of the Ni(SiGe) is observed in the bright field image in (a) of the sample annealed to 400ºC with the corresponding dark field image in (b) of the silicide islands.

Upon annealing above 400°C, significant grain growth was observed, with the average grain size increasing from 200 to 350nm. At this stage, agglomeration of the films began to occur as shown in Figure 6.5. Voids started to appear at grain boundaries, exposing areas of the bare substrate. The agglomeration process became more severe as the sample was further annealed to 550ºC. At this point, *in-situ* EELS spectra were obtained from different parts of the sample, as in Figure 6.6. This revealed that in areas where the film breaks up exposing the underlying $Si_{0.75}Ge_{0.25}$ substrate, there is an increase in the $\frac{Ge}{Si}$ ratio from 0.35 to 0.40, as compared with measurements made prior

to Ni deposition (section 6.1). In these areas, no Ni was detected. But in regions still covered by Ni(SiGe) grains, there is a decrease of the $\frac{Ge}{Si}$ ratio from 0.35 to 0.29. The stoichiometry of the silicide grains becomes $Ni(Si_{0.783}Ge_{0.217})$.

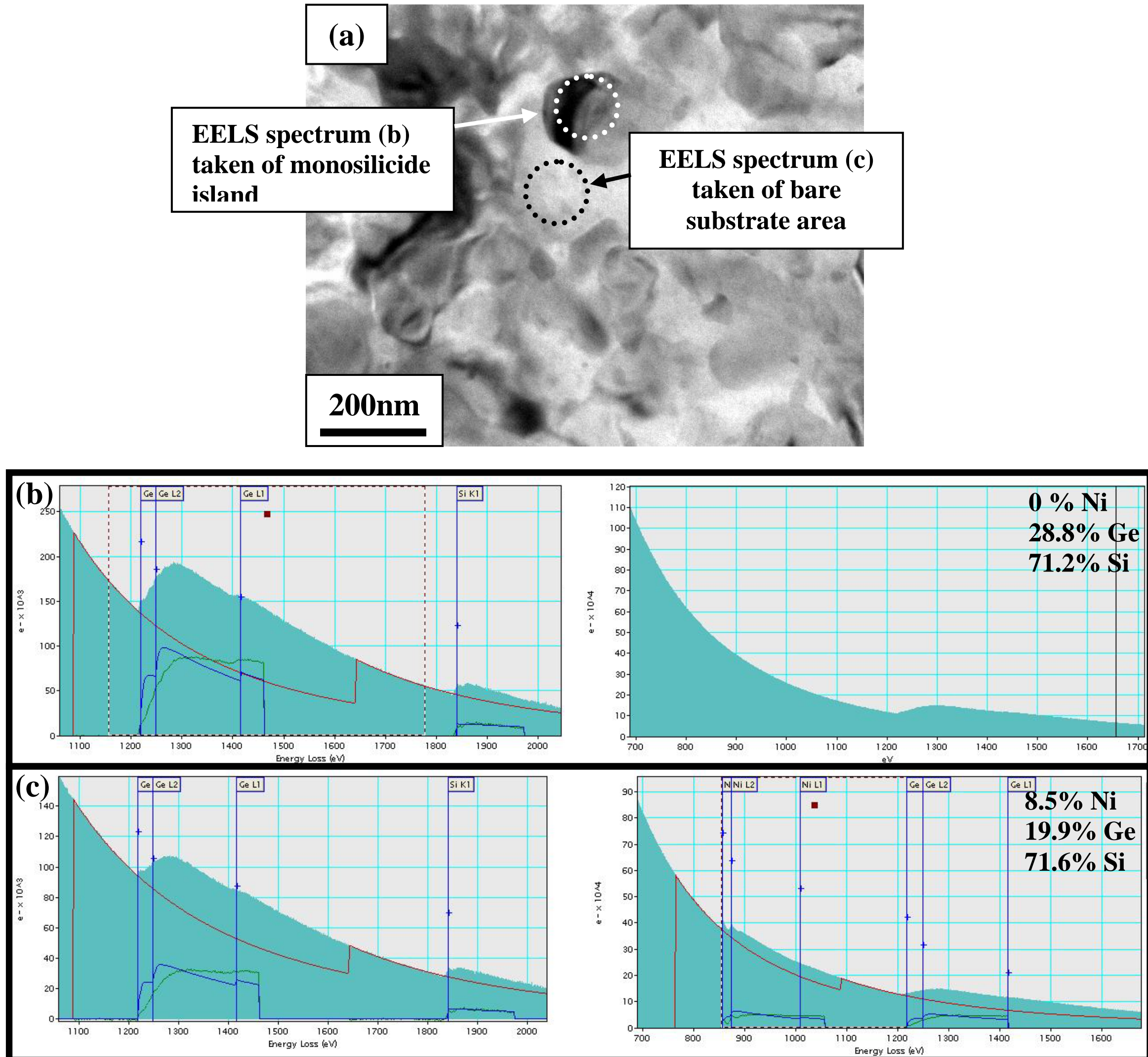

Figure 6.6 The bright field image in (a) showing the area where the EELS analysis was done, in the area of bare substrate for (b) and area of the monosilicide islands in (c). The percentage values represent the combined composition values of the three elements.

Our observations support the suggestion that Ge had began to segregate away from the $Ni(Si_{1-y}Ge_y)$ grains (where y becomes <0.25) towards the grain boundaries during annealing at elevated temperatures. This contributes to the break-up and agglomeration of the monosilicide film, in which the exposed substrate areas are Ge-rich. This phenomenon can be attributed to the values of the heat of formation for NiSi and NiGe, which have been determined[3] to be about –45 and –32 kJ/mol, respectively. These values suggest the crystal energy could be reduced by 13 kJ/mol, if Si atoms could replace the Ge atoms in the monosilicide film. Therefore, Ni atoms would tend to react preferably with Si atoms with the exclusion of Ge to the grain boundaries.

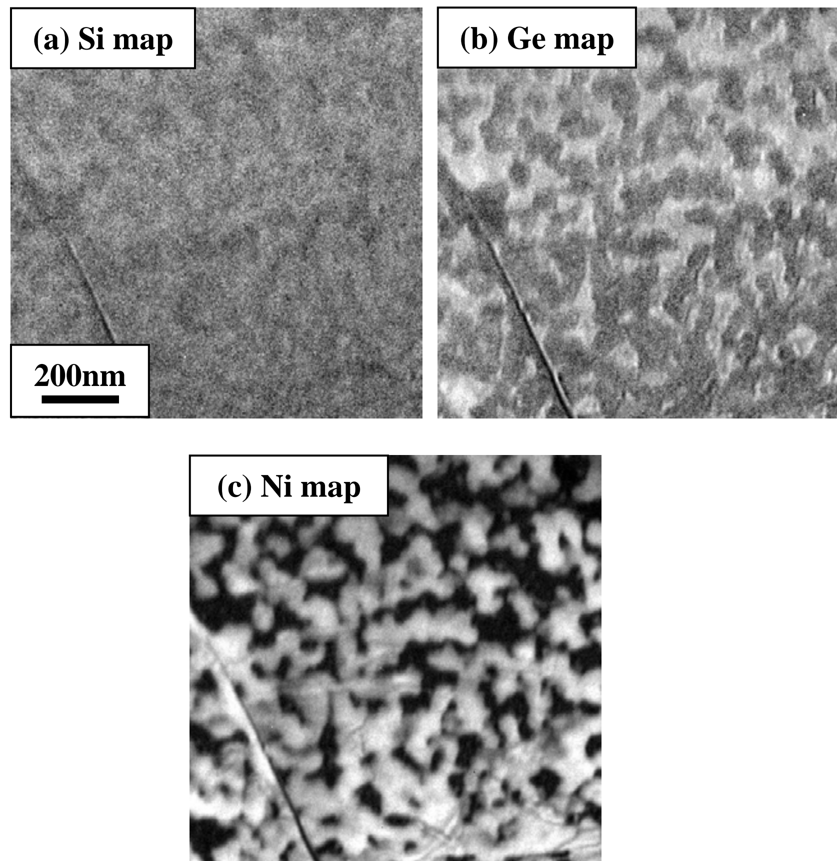

Figure 6.7 Showing the EFTEM images of (a) Si, (b) Ge and (c) Ni taken of the sample annealed at 550ºC.

This was further observed in EFTEM images taken at 550 ºC in Figure 6.7. The images reaffirm the observation that in areas where the bare substrate was visible, the Ge and Si concentrations are considerably higher in comparison with the other regions covered by the monosilicide islands. In contrast, a much lower concentration of Ni atoms was observed at areas with the bare substrate in comparison with the monosilicide islands.

Continued annealing at 700ºC led to a reduction in the number density of monosilicide islands, with a corresponding increase in their projected area and their thickness (as determined from an increase in mass-thickness image contrast in Figure 6.8) consistent with an Ostwald ripening process.

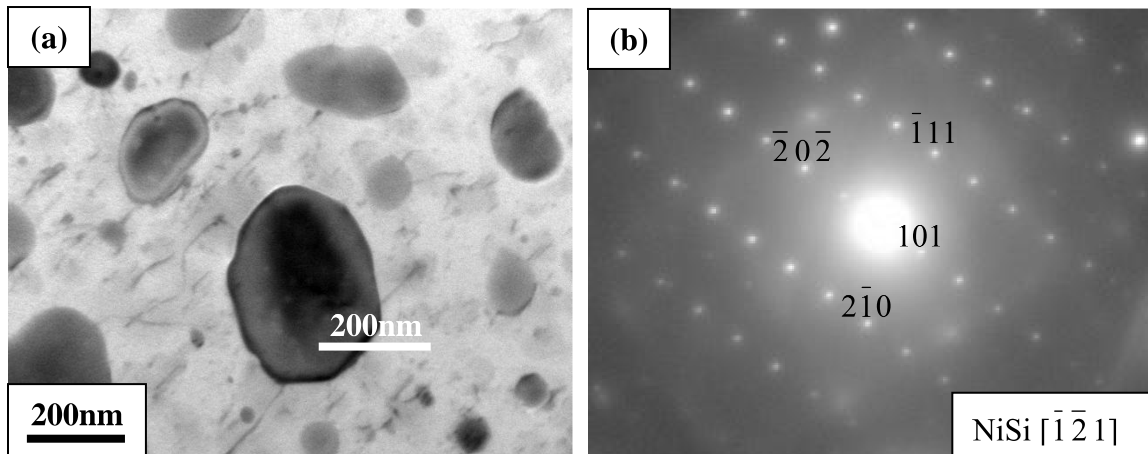

Figure 6.8 Showing the bright field images of $Ni(Si_{1-y}Ge_y)$ (where y<0.25) islands of the sample at 700ºC. An increase in mass-thickness image contrast suggests that the islands have become thicker. The corresponding SAED in (b) of the monosilicide island shows the crystallographic relation: NiSi $[\bar{1}\,\bar{2}\,1]$ // Si [100].

In his work, Pey *et al.*[4] explained that during the thermal reaction between a 25nm Ni film and $Si_{0.75}Ge_{0.25}$ alloy in the range of 500-700°C, the Ni atoms from the monosilicide islands diffuse deeper into the substrate while Ge atoms diffuse out of the

islands towards the surface. This interdiffusion increases at higher temperatures with no Ge segregation found at the silicide/substrate interface shown clearly in the cross-section TEM images in Figure 6.9. This is consistent with our observations of the monosilicide islands becoming thicker as the sample was annealed to 700ºC. Since there is a preference to form NiSi rather than NiGe due to the lower heat formation, Ni atoms will tend to diffuse into the underlying $Si_{0.75}Ge_{0.25}$ substrate, where there is a continuous supply of Si atoms, with Ge diffusing laterally out of the silicide.

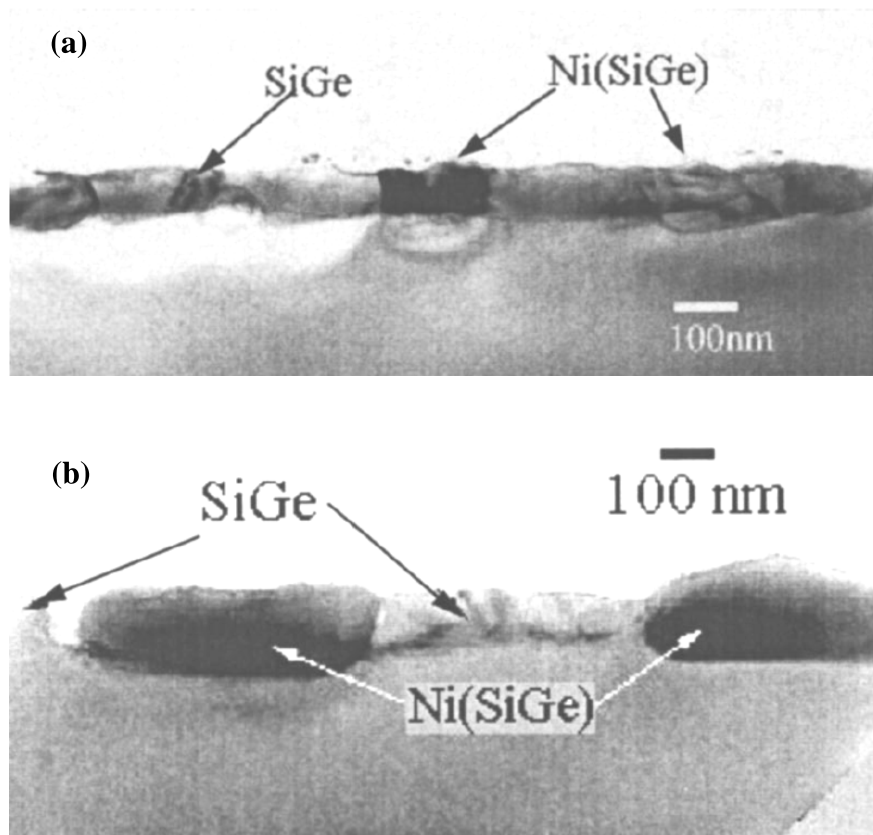

Figure 6.9 Reproduced from Pey *et al.*[4] showing a cross-sectional TEM image of Ni-silicided $Si_{0.75}Ge_{0.25}$ annealed at (a) 500ºC and (b) 800ºC. Comparing the two images, the monosilicide islands are much bigger and diffused deeper into the substrate at 800ºC.

Samples were further annealed to ~940-960°C at a ramp rate of 10°C per minute before the first evidence of $NiSi_2$ formation was observed. Islands with the characteristic square plan-view profile were observed, and a representative image is shown in Figure 6.10. Due to mass-thickness contrast, the characteristic inverted-pyramidal shapes of the $NiSi_2$ grains can be seen, with four (111) facets buried below the sample surface. The sides of the base of the pyramid lie along Si<110> directions, in the plane of the substrate surface. SAEDs and dark field images revealed the islands to be epitaxial, with the expected cube-on-cube orientation relationship[5]. In our previous experiment with Ni on Si (100), the formation of NiSi is the first phase to be observed, followed by $NiSi_2$ at 650ºC, and the temperatures at which these transformations were observed are consistent with a number of other reports[6,7,8,9]. However, in the case of Ni on $Si_{0.75}Ge_{0.25}$ substrates, no prior reports have been made of the formation of $NiSi_2$ on SiGe alloy substrates, and the compound $NiGe_2$ is not known in either bulk or thin film form[10].

The difficulty of nucleating $NiSi_2$ from Ni $(Si_{1-y}Ge_y)$ (where $y<0.25$) on $Si_{0.75}Ge_{0.25}$ is highlighted by our observations, where $NiSi_2$ was not formed below ~940ºC. Indeed, only a small fraction (~10%) of the monosilicide grains were observed to transform to $NiSi_2$, even after several minutes annealing in the range 940-960°C. Previous authors have reported in-situ X-ray diffraction studies during annealing of Ni films on $Si_{1-x}Ge_x$ to 850°C ($x=0.29$ and 0.58) and 950°C ($x=0.25$), with no evidence of $NiSi_2$ formation.

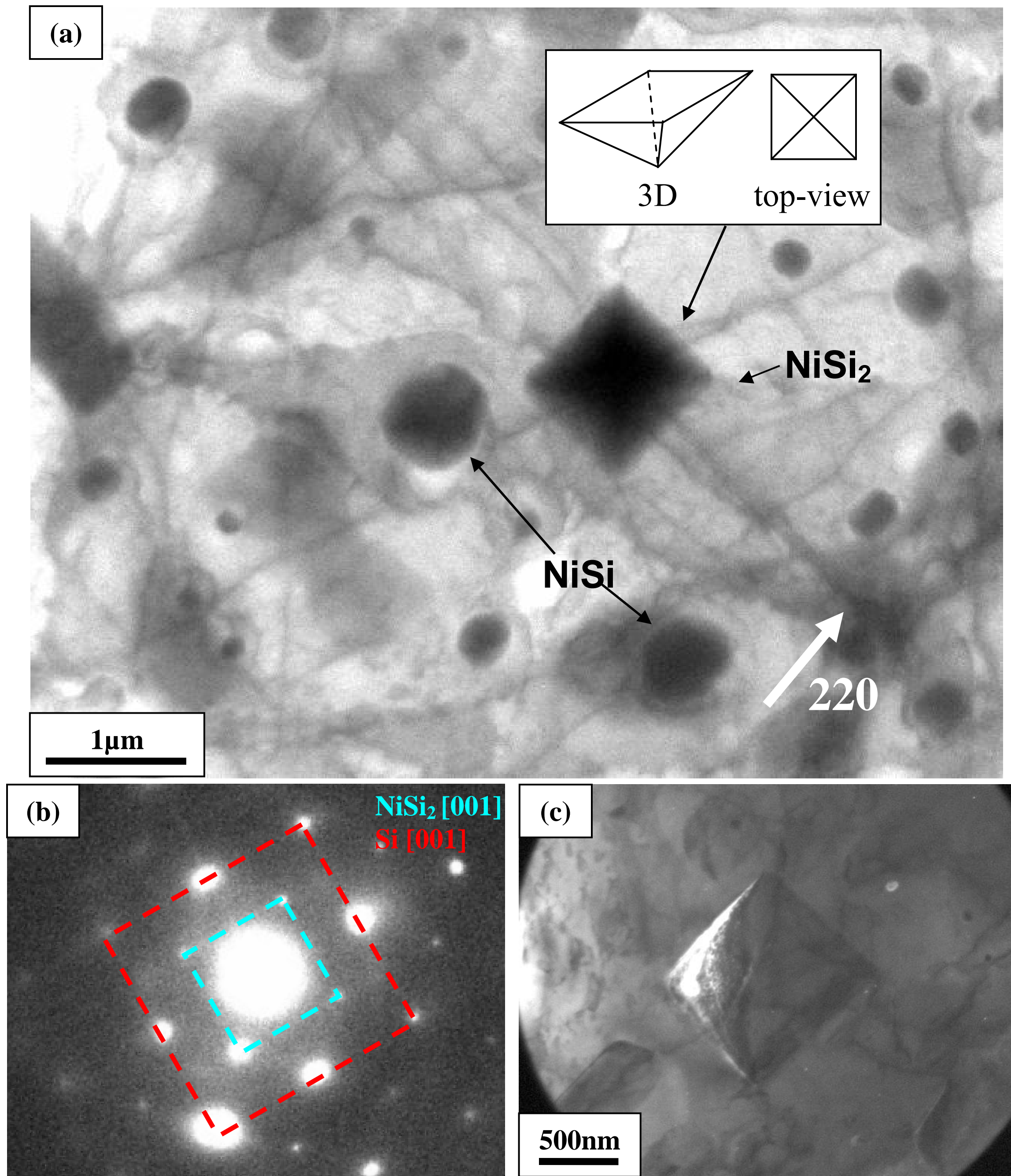

Figure 6.10 Showing a $NiSi_2$ grain with characteristic square plan view shape in (a), with the sides of the grain along the <110> directions. Mass-thickness contrast of the square grain reveals the characteristic inverted pyramidal shape of the $NiSi_2$ phase. The corresponding SAED in (b) (unit cell of Si and $NiSi_2$ in red and blue dotted line respectively) and dark field image in (c) shows the cube-on-cube relationship with the substrate with the crystallographic relation: $NiSi_2$ (100) // Si (100), $NiSi_2$ [100] // Si [100].

The presence of Ge clearly increases the nucleation barrier for $NiSi_2$ formation, suppressing the transformation in our experiments to substantially higher temperatures. According to the work of Seger et al.[11], a sudden decrease in Ge content of $Ni(Si_{1-x}Ge_x)$ films on $Si_{0.7}Ge_{0.3}$ may be expected at temperatures between 600 and 650°C. Below 600°C, they found that the monosilicide had the same Si:Ge ratio as the substrate, i.e. $Ni(Si_{0.7}Ge_{0.3})$; however, above 650°C, the Ge content was observed to fall from 30% to ~10%.

Entropy of mixing calculations[12] show that the free energy of formation ΔG of $NiSi_2$ from NiSi and Si is –10kJmol^{-1}. In the case of $NiSi_2$ formation from $Ni(Si_{0.9}Ge_{0.1})$, the free energy change is reduced to –8.5kJmol^{-1}. Since the equilibrium density of critical nuclei may be shown from classical nucleation theory to be proportional to

$$\exp(-\Delta\sigma^3/\Delta G^2 kT)$$

The presence of Ge is likely to have made an important contribution to the observed increase in the temperature at which $NiSi_2$ nucleation was observed in our experiments (~300K higher than in the absence of Ge).

However there is another observation made at 940-960ºC, which coincides with the formation of $NiSi_2$. Upon reaching that temperature range, the germanosilicide islands begin to creep along the surface of the $Si_{0.75}Ge_{0.25}$ substrate in a liquid-like motion leaving behind dark and bright patches as shown by the image contrast in Figure 6.11 (a). The movement of these islands was mostly around their original positions. However in some instances, some of the islands traveled as far as approximately 2µm. It seemed as though they were burrowing along the surface of the substrate leaving a bright trail as observed from real-time video images in Figure 6.11 (b).

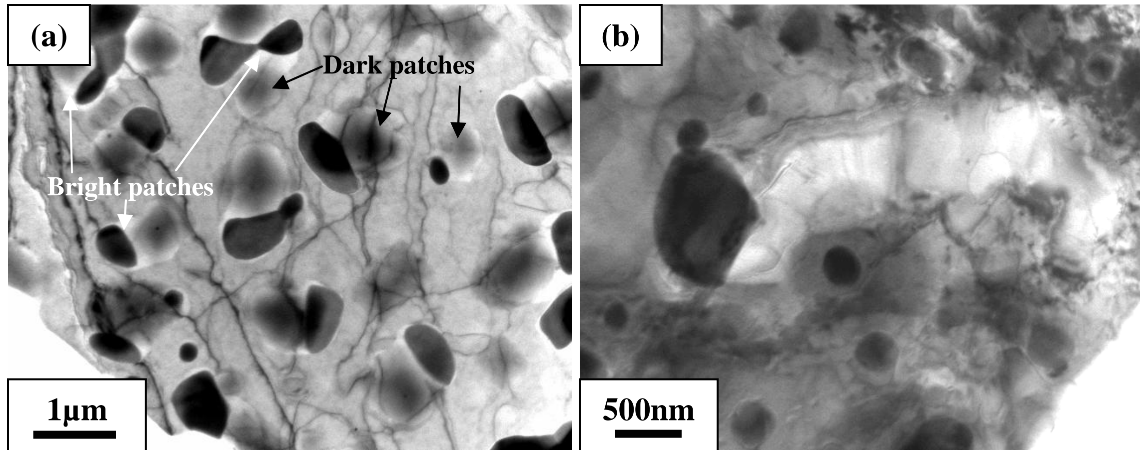

Figure 6.11 Showing areas of dark and bright patches as the monosilicide islands begin to creep along the surface of the $Si_{0.75}Ge_{0.25}$ substrate upon reaching the temperature range of 940-960ºC.

In-situ EELS spectra taken from the dark and bright patches revealed the absence of Ni atoms. This indicated that the dark and bright patches are areas of bare substrate. The elemental composition of Si and Ge was calculated from the EELS spectra obtained from the dark and bright patches, as well as areas of bare substrate without the patches. Calculations from the dark and bright patches revealed that in these regions there is a decrease of the $\frac{Ge}{Si}$ ratio from 0.35 to 0.10-0.15, as compared with measurements made prior to Ni deposition. While in areas of the substrate without the dark and bright patches, the $\frac{Ge}{Si}$ ratio increased from 0.35 to 0.44.

EFTEM images of Ni, Ge and Si elements were obtained in these areas of the sample as shown in Figure 6.12. The Ni elemental map clearly outlines the areas with the germanosilicide islands. However from the Si and Ge element maps, it is obvious that the areas with the bright and dark patches are actually localized areas of bare $Si_{0.75}Ge_{0.25}$ substrate where Ge concentration has depleted significantly, and are thus richer in Si.

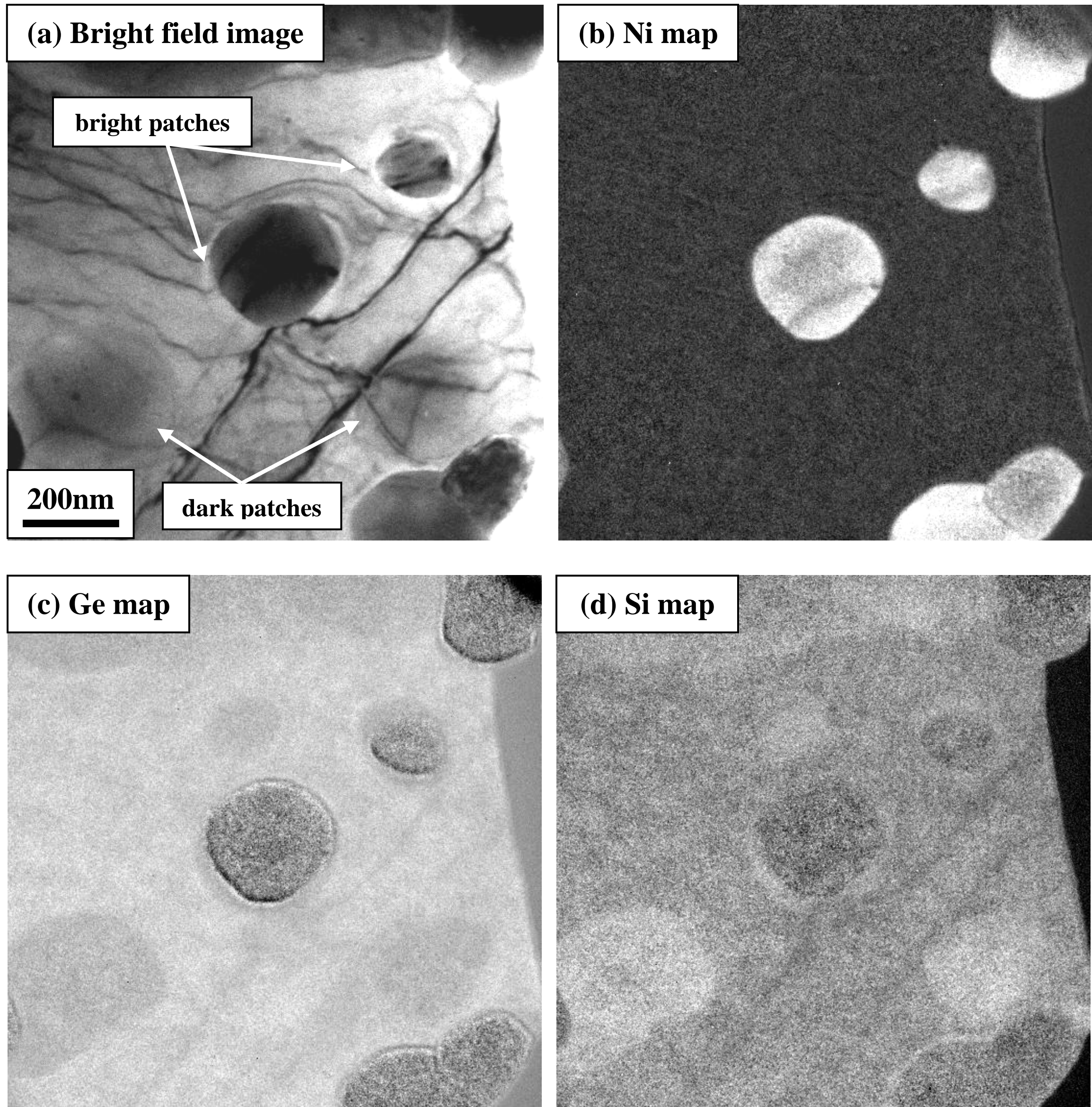

Figure 6.12 EFTEM images were obtained for the area of the sample at 940-960C shown in (a). The Ni map in (b) outlines the area with the monosilicide islands. From the (c) Ge and (d) Si maps it can be observed that the bright and dark patches form the bright field image in (a) are localized areas with lower Ge concentration but rich in Si.

We can consider the possibility that annealing at the elevated temperatures used here may have resulted in decrease of the Ge concentration at localized areas of the substrate by evaporation. Jones *et al.* [13] described a cleaning procedure for $Si_{1-x}Ge_x$ alloy films and strained layer films on SiGe substrates, involving ex-situ ultra-violet ozone

(UVO) enhanced oxidation followed by in-situ desorption of the oxide film at temperatures ≤ 1050°C. For relaxed $Si_{0.7}Ge_{0.3}$ samples, it was found that after UVO cleaning the Ge content dropped from 30% in the bulk to 2%-12% in the top surface layer of 1-5nm. In this situation, the layer will be subject to a tensile strain due to the lattice mismatch induced by the Ge depletion. This tensile strain will increase the barrier to the nucleation of $NiSi_2$ since, as discussed earlier, the reaction results in a volume contraction and thus further tensile strain.

6.4 Summary of Chapter 6

In this chapter, the thermal reaction between a 12nm Ni film on a relaxed $Si_{0.75}Ge_{0.25}$ substrate was observed with increasing temperature. The first evidence of a reaction was in the temperature range of 200-250°C, where a polycrystalline and highly strained monosilicide $Ni(Si_{0.75}Ge_{0.25})$ was formed. The formation temperature was 50-100°C higher than in the case of Ni on Si (100), indicating that the presence of Ge has retarded the reaction to a higher temperature.

Agglomeration of the monosilicide film started to occur at 400°C with voids appearing at the grain boundaries. The agglomeration process becomes more severe at 550°C, with the film breaking up to form discrete islands, exposing areas of bare substrate. EELS and EFTEM analysis at this temperature revealed that Ge atoms from the monosilicide islands have segregated to the grain boundaries and areas of bare substrate making these areas Ge-rich. The segregation of Ge is attributed to the higher heat of formation of NiGe in comparison to NiSi.

Increasing the temperature to 700°C, lead to the reduction in the density of the monosilicide islands with the islands becoming thicker. At this stage, Ni atoms were diffusing into the $Si_{0.75}Ge_{0.25}$ substrate with Ge atoms diffusing to the surface at the areas with bare substrate.

Upon annealing to the temperature range of 940-960°C, the $NiSi_2$ grains with the characteristic square plan-view profile was observed after several minutes. At the same time, EELS and EFTEM analysis revealed that there were localized areas of bright and dark patches where the Ge concentration has been depleted significantly. It is suggested that the local decrease in Ge has been caused by evaporation of Ge, leaving behind a strained Si layer. The presence of Ge increases the temperature at which the onset of the transformation of $NiSi_2$ is observed to be ~300°C more than in the case of Ni on Si (100). This is attributed to the reduced free energy of formation of $NiSi_2$ in the presence of Ge.

References:

[1] C.C. Ahn, O.L. Krivanek, R.P Burgner, M.M. Disko and P.R.Swann, *EELS Atlas (A reference guide of electron energy loss spectra covering all stable elements)*, Gatan Inc., (1983).

[2] J.J. Rousseau, *Basic Crystallography,* John Wiley and Sons, (1998), Chapt. 2.

[3] F.R. Deboer, R. Boom, W.C. Mattens, A.R. Miedema and A.K. Niessen, *Cohesion in Metals: Transition Metal Alloys,* North-Holland, Amsterdam, (1988).

[4] K.L. Pey, W.K. Choi, S. Chattopadhyay, H.B. Zhao, E.A. Fitzgerald, D.A. Antoniadis and P.S. Lee*, J. Vac. Sci. Technol. A* **20(6)**, (2002), 1903.

[5] R. Nath and M. Yeadon, *Electrochem. Solid-State Lett.* **7(10)**, (2004), in print.

[6] J.O. Olowolafe, M.-A. Nicolet and J.W. Mayer, *Thin Solid Films* **38**, (1976), 143.

[7] F.M. d'Heurle, C.S. Petersson, J.E.E. Baglin, S.J. La Placa and C.Y. Wong, *J. Appl. Phys.* **55**, (1984), 4208.

[8] B.A. Julies, D. Knoesen, R. Pretorius and D. Adams, *Thin Solid Films* **347**, (1999), 201.

[9] M. Tinani, A. Mueller, Y. Gai, E.A. Irene, Y.Z. Hu and S.P. Tay, *J. Vac. Sci Tech B* **19**, (2001), 376.

[10] M.W. Wittmer, M.A. Nicolet and J.W. Mayer, *Thin Solid Films* **42**, (1997), 51.

[11] J. Seger, S.L. Zhang, D. Mangelinck and H.H. Radamson, *Appl. Phys. Lett.* **81**, (2002), 1978.
[12] F.M. D'Heurle, *J. Mater. Res.* **3(1)**, (1988), 167.
[13] D.E. Jones, J.P. Pelz, Y.H. Xie, P.J. Silverman and E.A Fitzgerald, *Surf. Sci.* **341**, (1995), L1005.

Chapter 7 Conclusion

In this work, the thermal reactions at different temperatures were studied for a 12nm Ni film on Si (100) and relaxed $Si_{0.75}Ge_{0.25}$ (100) substrates using a modified *in-situ* UHV TEM; MERLION, which enabled real-time *in-situ* observation of phase transformations, agglomeration of the thin films and the nucleation of the disilicide for both cases. The schematic diagram shown in Figure 7.1 shows a comparison of reactions for the Ni/Si and Ni/$Si_{0.75}Ge_{0.25}$ systems at different temperatures.

Upon annealing the samples, the formation of the monosilicide phase was observed for the Ni/Si and Ni/$Si_{0.75}Ge_{0.25}$ system at 150ºC and 200-250ºC respectively. The presence of Ge clearly retarded the thermal reaction to form the monosilicide phase. In these systems, a continuous polycrystalline but highly strained film with an average grain size of 200nm was observed.

As the samples were further annealed, significant grain growth followed by the onset of agglomeration of the monosilicide films occurred. Voids started to appear in the monosilicide film at 450ºC for Ni/Si and 400ºC for Ni/$Si_{0.75}Ge_{0.25}$. The agglomeration process became more severe at 550ºC for both systems. At this point the monosilicide film had broken up into islands leaving exposed areas of bare substrate. In the Ni/$Si_{0.75}Ge_{0.25}$ system, EELS and EFTEM data showed that Ge atoms from the monosilicide islands have segregated to the grain boundaries and areas of bare substrate making these areas Ge-rich. It was explained that the segregation of Ge is attributed to the higher heat of formation of NiGe in comparison to NiSi. Ni atoms would tend to react preferably with Si atoms with the exclusion of Ge from the monosilicide islands, making them depleted of Ge.

In the Ni/Si system, the nucleation of the $NiSi_2$ was first observed at 650ºC, occurring at the thin edges of the NiSi islands, at the free surface of the substrate. Our observations are understood from a consideration of the reduction in the energy barrier for nucleation of $NiSi_2$ at the free surface of the film where enhanced strain relaxation can occur, in contrast to a location along the buried NiSi:Si interface. In comparison for the $Ni/Si_{0.75}Ge_{0.25}$ system, the formation of $NiSi_2$ was observed at 940-960ºC. Only a small fraction (~10%) of the monosilicide islands were observed to transform to $NiSi_2$. The presence of Ge had clearly increased the nucleation temperature for $NiSi_2$ by ~300ºC more than in the case of Ni/Si. This was attributed to the reduced free energy of formation of $NiSi_2$ from $-10kJmol^{-1}$ (from NiSi) to $-8.5kJmol^{-1}$ (from $Ni(Si_{0.9}Ge_{0.1})$). At the same time, EELS and EFTEM data showed that there were localized areas where the Ge concentration was depleted significantly due to evaporation, leaving behind a layer of strained Si. Since the phase $NiGe_2$ is not known to form, the presence of areas with only strained Si enabled the formation of $NiSi_2$.

Some future work can be undertaken to better understand the mechanism for the formation of $NiSi_2$ on SiGe substrates. A clearer picture of the diffusion of the Ni, Si and Ge can be obtained if EELS and EFTEM data are obtained from *ex-situ* cross-sectional samples annealed at different temperatures and correlated to the *in-situ* data shown in this work.

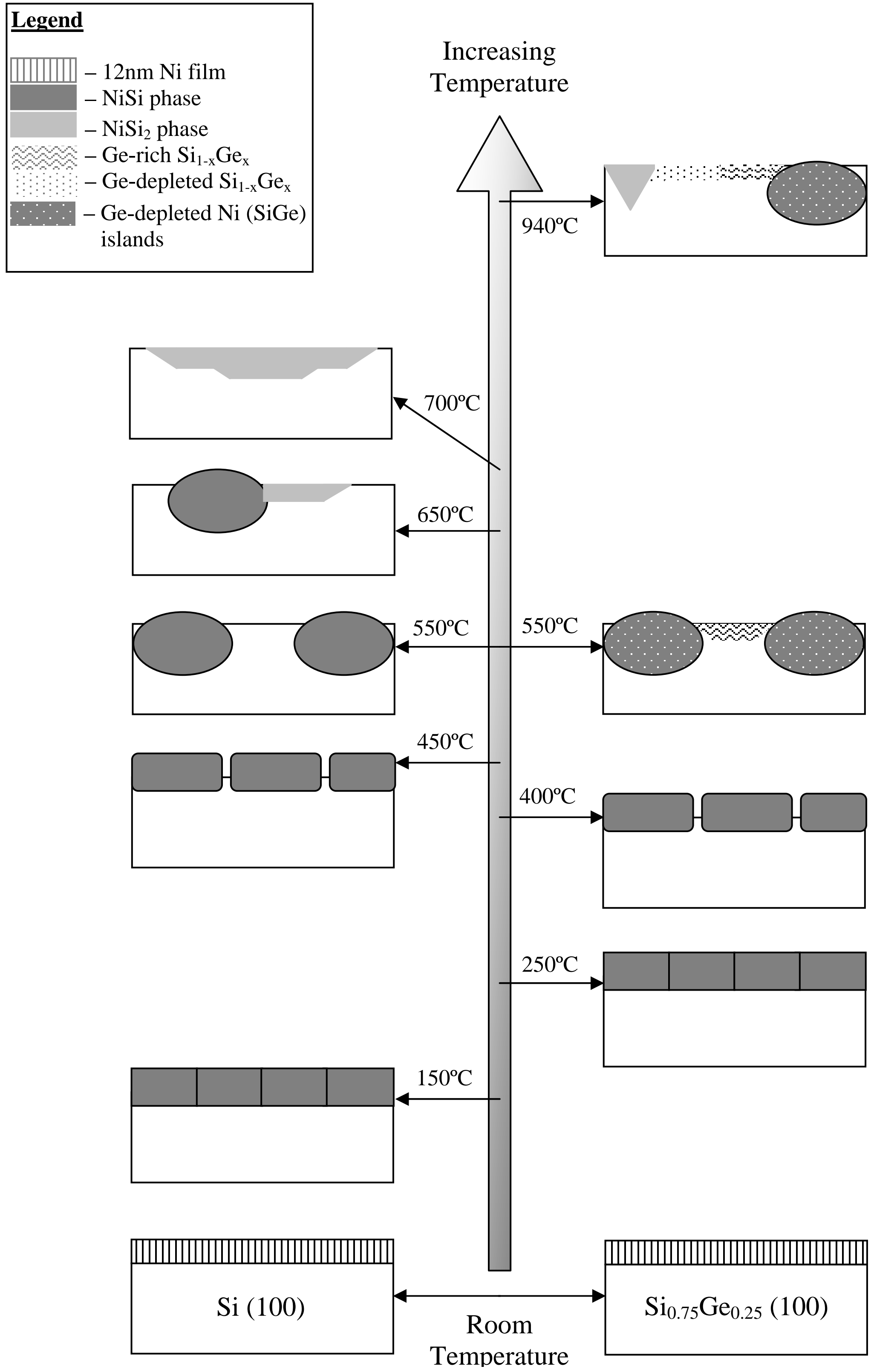

Figure 7.1 Showing a schematic diagram comparing the thermal reaction of 12nm Ni on Si (100) and relaxed $Si_{0.75}Ge_{0.25}$ (100) substrates.

Appendix Indexing of SAED patterns

A.1 Identification of major spots and calibration of SAED patterns

First and foremost, the center spot of the SAED, which corresponds to the direct transmitted beam, must be identified. This can be easily identified, as it is the central and brightest spot for a ring or spot pattern in a SAED. The identification and calibration of SAED patterns were then carried out in three steps.

1. In the first step, the d-spacings of the ring or spot pattern was calculated by using any of the two methods below:
   a. Camera constant method.
   b. Ratio method.
2. The second step measures the angles between the two spots that have been indexed by the first step to verify that the spots have been indexed correctly.
3. Lastly, the SAED pattern is simulated using the Electron Microscopy Software Java (JEMS) version 1.3402W2003, to verify the analysis of the experiment data.

A.1.1 Step one

For the camera constant method, we use the inverse relationship between real and reciprocal space, which is given by equation 3.14. Rearranging the equation gives

$$d_{hkl} = \frac{\lambda L}{R} = \frac{C}{R} \quad \text{(A.1)}$$

where the product of λL can be taken as C, which is a camera constant value for a given camera length. For all the experiments SAED patterns were taken at camera length, L of

100cm. Since the accelerating voltage of the electron beam for the JEOL 2000V is 200 keV, the corresponding wavelength of the electron beam, λ can be calculated as approximately 0.0025nm. The radius of the spots, R can be measured from the SAED pattern. Given the information above, we can now carry the calculation of the d-spacing values for each pair of spots. The values are then compared and matched to the d-spacing values of Si found in the 2001 JCPDS-Powder Diffraction Data, File 26-1481.

The ratio method uses the ratios between the squared values of the d-spacing of planes of atoms to index the reflections found in a SAED pattern. It can be further explained using Si as an example. Silicon has a diamond structure and the relation between the d-spacing, d and lattice constant, a of (hkl) plane of atoms can be expressed as:

$$\frac{1}{d^2} = \frac{h^2 + k^2 + l^2}{a^2} \tag{A.2}$$

Let $h^2 + k^2 + l^2 = N^2$, the ratio of the d-spacings for two different reflections spot 1 and 2 in a SAED, can be expressed as:

$$\frac{d_2^2}{d_1^2} = \frac{N_1^2}{N_2^2} \tag{A.3}$$

In order to relate this equation between d and N to the radius of a spot or ring reflection, R, Equation 3.6 can be expressed as:

$$\frac{d_2^2}{d_1^2} = \frac{N_1^2}{N_2^2} = \frac{R_1^2}{R_2^2} \tag{A.4}$$

The ratio of the square of the d-spacings of the reflecting planes of (220) and (400) is 0.5, as listed in Table A.1. If the ratio of the square of the measure R-values is also 0.5, then we can conclude that the two planes are indeed the (220) and (400) planes.

Plane	$d^2 = \frac{a^2}{h^2 + k^2 + l^2}$	$\frac{d_{400}^2}{d_{220}^2}$
(220)	$d_{220} = a^2/8$	0.5
(400)	$d_{400} = a^2/16$	

Table A.1 Ratio of square of d-spacing between Si (400) and Si (220) planes.

A.1.2 Step two and three

From definition, the angles between the planes of atoms in the real and reciprocal lattice are the same. Therefore angles calculated in the real space between plane A and plane B, with miller indices ($h_a k_a l_a$))and ($h_b k_b l_b$) respectively, should closely correspond to the angles between the spots of plane A and B in the diffraction pattern. The angles between the planes for different crystals structure are:

For cubic, $$\cos\theta = \frac{h_a h_b + k_a k_b + l_a l_b}{\sqrt{h_a^2 + k_a^2 + l_a^2} \bullet \sqrt{h_b^2 + k_b^2 + l_b^2}} \qquad (A.5)$$

For orthorhombic with lattice parameters a ≠ b ≠ c,

$$\cos\theta = \frac{\frac{h_a h_b}{a^2} + \frac{k_a k_b}{b^2} + \frac{l_a l_b}{c^2}}{\sqrt{\frac{h_a^2}{a^2} + \frac{k_a^2}{b^2} + \frac{l_a^2}{c^2}} \bullet \sqrt{\frac{h_b^2}{a^2} + \frac{k_b^2}{b^2} + \frac{l_b^2}{c^2}}} \qquad (A.6)$$

In the last step, as mentioned, the diffraction is simulated using JEMS to see if it fits with the experimental analysis. To illustrate the analysis of the diffraction patterns several examples of diffraction data from the experiments will be used.

A.2 Calibration and indexing of SAED pattern in Figure 5.1 (b)

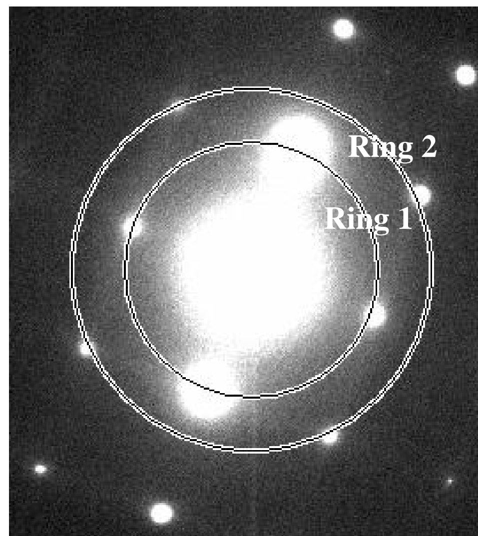

Figure A.1 Showing SAED pattern of a clean Si (100) sample for 12nm Ni on Si experiment from Figure 5.1 (b)

To further illustrate the steps for analysis, we will calibrate and index the SAED for the 12nm Ni on clean Si (100) experiment from Figure A.1 taken from Figure 5.1 (b). The spot patterns that are assumed to correspond to (220) and (400) planes are marked Ring 1 and Ring 2 respectively in the micrograph, while the transmitted beam is the center of the rings. Using the second method in the first step, we calibrate the spots by first measuring the radius of the rings in terms of pixels in the micrograph processing

program under Microsoft Windows, Digital Micrograph 3.1 which is 146.186 and 204.013 for Ring 1 and 2 respectively.

With the ratio from equation A.3, we have

$$\frac{d_2^2}{d_1^2} = \frac{R_1^2}{R_2^2} = 146.186^2/204.013^2 = 0.513$$

which gives almost the same value as listed in Table A.1. Therefore, it can be initially be concluded that the rings marked 1 and 2 are the (220) and (400) reflecting planes of the silicon single crystal substrate with an error percentage of ± 2.6%.

The second step would be calculate the angle between the two set of spots and compare it with the calculated angle between Si (220) and Si (400). For a Si cubic system, we use equation A.5,

$$\cos\theta = \frac{4*2+0*2+0*0}{\sqrt{4^2+0^2+0^2}\bullet\sqrt{2^2+2^2+0^2}}$$

$$\Rightarrow \qquad \theta = 45^\circ$$

Comparing this with the experimental measurement of 44.79, there is a percentage error of ± 0.5%.

The third step would be simulating the diffraction pattern using JEMS with the zone axis of [100] at the camera length of 100cm as in Figure A.2. The simulated data clearly corresponds to the experimental results and this verifies its validity.

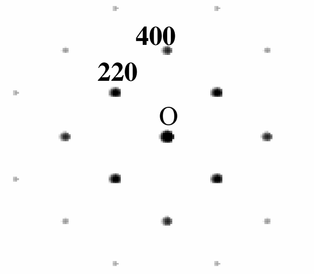

Figure A.2 Showing a simulated diffraction pattern of a single crystal of Si (100) along the [100] zone axis.

From the calibration done for the Si (100), we can determine the camera constant, λL and use this value to index other diffraction patterns taken at the same camera length. The reader should take note the units for this value is arbitrary to the software used to make the measurements.

From equation 3.14, the camera constant can be determined as follows,

For Si (220), λL = R(pixels) • d(Å) = 146.186 • 1.9202 = 280.071

For Si (400), λL = R(pixels) • d(Å) = 204.013 • 1.3576 = 276.968

The average value for the camera constant = 278.520

This constant value will be used to calculate the d-spacing of each spot or ring pattern using the measured radius from the center beam and equation 3.14.

As mentioned, the 200 kV electron beam used in this study corresponds to a wavelength λ, of 0.0025nm. Since λ is small, the Bragg angle θ is about 0.5° for low-order planes. Planes which gives rise to strong maxima will therefore be approximately parallel to the electron beam direction. Reflections from planes such as (111) are not excited at this orientation. This is because the angle of the (111) plane is at 35.3° to the [100] beam direction.

When the electron beam is parallel to an important zone axis there will be a large number of planes sufficiently close to their Bragg angles to give rise to diffracted beams, because strong reflections will be excited even when the incident beam does not exactly satisfy the equation (3.8). This relaxation of Bragg's law arises because the specimens from which the patterns are obtained are thin and the discrete maxima expected from bulk crystals, become elongated parallel to the thin dimensions of the sample. This is the reason for the observation of the (400) and (220) planes as the low order planes, even though the planes are at an angle of 0° to the direction of the [100] beam, which should not give rise to strong reflections according to Bragg's law. Therefore, the direction of the electron beam traveling down the sample is parallel to the [100] direction will correspond diffraction to occur at the Si (400) and Si (220) planes. These are the two other major sets of reflections that we will need to identify in the each SAED, to calibrate the diffraction patterns.

A.3 Indexing of SAED in Figure 5.2 (b)

Figure A.3 shows the SAED taken from the as-deposited 12nm Ni film on the Si (100) substrate from Figure 5.2 (b). The square-array spot pattern can be clearly identified as single crystal Si (100) with [100] zone axis, which will be used for the calibration of this SAED (refer to section A.2). In addition to the spot pattern, there is a polycrystalline ring pattern, which will be indexed in this section. Measurements of the radius and calculation of the d-spacing of each of the rings is represented in Table A.2. As shown in the table, the calculated d-spacing closely matched with the d-spacing plane indices of nickel from the JCPDS file 04-0850. From this analysis of the data, it is

concluded that the nickel deposited on the Si (100) is a polycrystalline film with face-centered cubic structure and space group of $Fm\bar{3}m$.

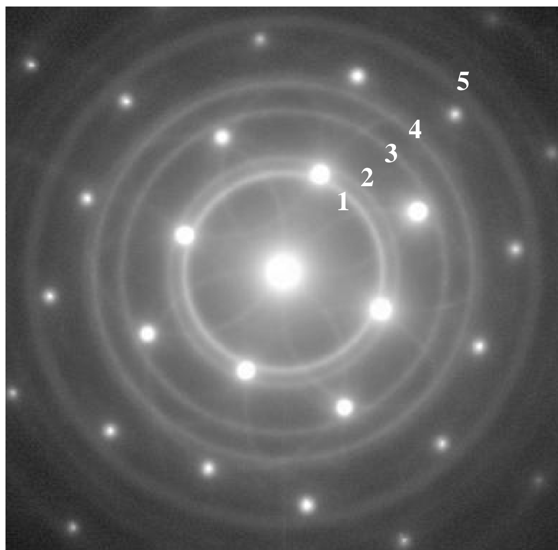

Figure A.3 SAED pattern for as deposited 12nm Ni on Si (100) sample from Figure 5.2 (b).

Ring	Radius(r)	Calculated d-spacing (Å) = λL / r	d-spacing of planes of atoms from JCPDS file 04-0850 which matches the calculated values	
1	137	2.033	2.034	(111)
2	154.5	1.803	1.762	(200)
3	223	1.249	1.246	(220)
4	262	1.063	1.0624	(311)
5	349	0.798	0.8084	(331)

Table A.2 Showing the comparison and analysis of the calculated d-spacings of the Ni polycrystalline rings with d-spacings from a standard JCPDS file 04-0850.

A.4 Indexing of SAED pattern in Figure 5.4 (a)

The SAED in Figure A.4 shows a square-array spot pattern, indicated by a red square, can be clearly identified as single crystal Si (100) with [100] zone axis, which will be used for the calibration of this SAED (refer to section A2). Other spots of interest

are labeled and measurements of the radius and calculation of the d-spacing of each of the spots is represented in Table A.3. As shown in the table, the calculated d-spacing closely match with the d-spacings of the plane indices of the NiSi phase from the JCPDS file 38-0844.

To further verify that the calculated d-spacings of the spot pattern belong to the NiSi phase of JCPDS file 38-0844, we can proceed with step two by calculating the angles between the proposed planes of atoms as shown in Table A.4. As observed in Table A4, the ($\bar{1}01$) plane was used rather than the (101) plane. This is because the proposed structure is orthorhombic, and while the d-spacings of ($\bar{1}01$) and (101) are the same, the angle between the two planes and a reference plane are different. For example, if the reference plane is (112) plane, the angles for the ($\bar{1}01$) and (101) planes are 78.6º and 41.2º. Judging from the angle between spot 1 and 6, 41.2º would definitely be unlikely. Therefore, spot 1 is more likely to be the ($\bar{1}01$), while the (101) plane is omitted.

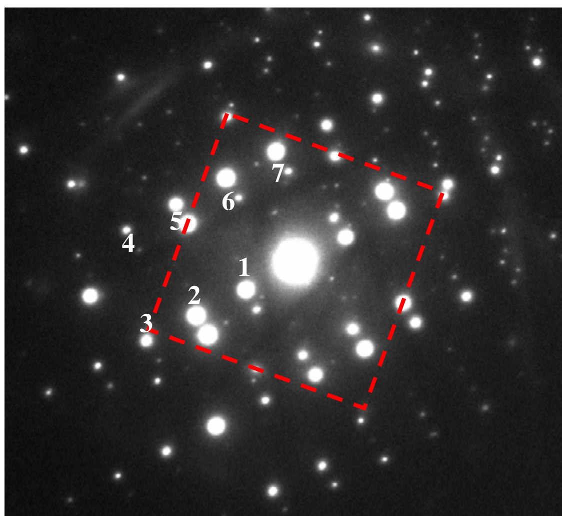

Figure A.4 SAED pattern of NiSi film from Figure 5.4 (a).

Finally, the experimental data is verified by simulating the diffraction pattern using JEMS. The zone axis was first calculated, which is the direction perpendicular to all the proposed plane indices. Using the dot product for vectors, the zone axis can be calculated as $[1\bar{3}1]$. The simulated data indexed with NiSi plane indices is shown in Figure A.5. With reference to detailed analysis and evidence from experimental data, it can be concluded that the SAED from Figure 5.4 (a) is of orthorhombic NiSi with the MnP structure and space group Pnma (62).

Spot	Radius(r)	Calculated d-spacing (Å) = λL / r	d-spacing of planes of atoms from JCPDS file 38-0844 which matches the calculated values	
1	73	3.815	3.842	(101)
2	147	1.895	1.921	(202)
3	293	0.951	0.9605	(303)
4	225	1.238	1.260	(114)
5	169	1.648	1.632	(013)
6	143	1.947	1.978	(112)
7	146	1.908	1.919	(211)

Table A.3 Showing the comparison and analysis of the calculated d-spacings of Figure 5.4 (a) spot pattern with d-spacings from a standard JCPDS file 38-0844.

Planes	$(\bar{1}01)$	$(\bar{2}02)$	$(\bar{3}03)$	$(\bar{1}14)$	(013)	(112)	(211)
$(\bar{1}01)$		0º	0º	38.6º	54.0º	78.6º	107.9º
$(\bar{2}02)$	0º		0º	38.6º	54.0º	78.6º	107.9º
$(\bar{3}03)$	0º	0º		38.6º	54.0º	78.6º	107.9º
$(\bar{1}14)$	38.6º	38.6º	38.6º		15.4º	40.0º	75.2º
(013)	54.0º	54.0º	54.0º	15.4º		24.6º	53.9º
(112)	78.6º	78.6º	78.6º	40.0º	24.6º		29.3º
(211)	107.9º	107.9º	107.9º	75.2º	53.9º	29.3º	

Table A.4 Showing the calculated angles between planes of atoms with d-spacings matching closely with experimental data in Figure 5.4 (a).

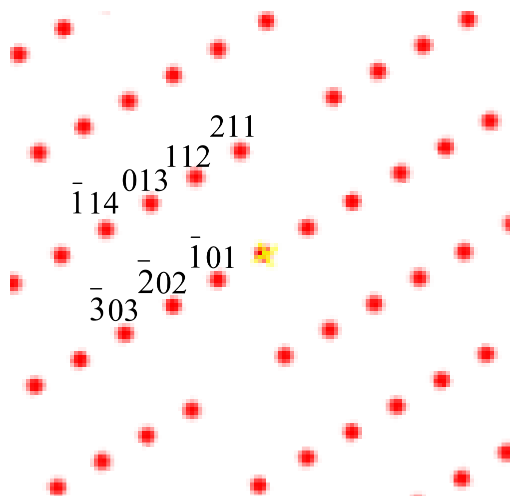

Figure A.5 Showing a simulated diffraction pattern of orthorhombic NiSi along the [1 $\bar{3}$ 1] zone axis.

A.5 Indexing of SAED pattern in Figure 5.4 (c)

The SAED in Figure A.6 shows a square-array spot pattern, indicated by the red square, which can be clearly identified as single crystal Si (100) with the [100] zone axis, which will be used for the calibration of this SAED (refer to section A.2). Other spots of interest are labeled in Figure A.6 and measurements of the radius and calculation of d-spacings of each of the spots is represented in Table A.5. As shown in the table, the calculated d-spacings closely match with the d-spacings of the plane indices of the NiSi phase from the JCPDS file 38-0844.

To further verify that the calculated d-spacings of the spot pattern belong to the NiSi phase of JCPDS file 38-0844, step two was carried out by calculating the angles between the proposed planes of atoms as shown in Table A.6.

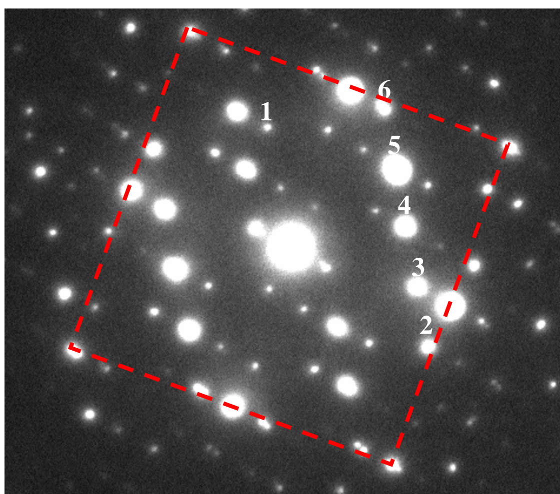

Figure A.6 SAED pattern of NiSi film from Figure 5.4 (c).

Finally, the experimental data is verified by simulating the diffraction pattern using JEMS. The zone axis was first calculated, which is the direction perpendicular to all the proposed plane indices. Using the dot product for vectors, the zone axis can be calculated as [010]. The simulated data indexed with NiSi plane indices is shown in Figure A.7. With reference to detailed analysis and evidence from experimental data, it can be concluded that the SAED from Figure 5.5(c) is of orthorhombic NiSi with the MnP structure and space group Pnma (62).

Spot	Radius(r)	Calculated d-spacing (Å) = λL / r	d-spacing of planes of atoms from JCPDS file 38-0844 which matches the calculated values	
1	99	2.813	2.830	(002)
2	145	1.9208	1.921	(202)
3	117	2.381	2.375	(201)
4	106	2.628	2.616	(200)
5	117	2.381	2.375	(201)
6	146	1.908	1.921	(202)

Table A.5 Showing the comparison and analysis of the calculated d-spacings of Figure 5.4 (c) spot pattern with d-spacings from a standard JCPDS file 38-0844.

Planes	(002)	$(\bar{2}0\bar{2})$	$(\bar{2}0\bar{1})$	$(\bar{2}00)$	$(\bar{2}01)$	$(\bar{2}02)$
(002)		132.76º	114.81º	90º	65.19º	47.24º
$(\bar{2}0\bar{2})$	132.76º		17.95º	42.76º	67.57º	85.52º
$(\bar{2}0\bar{1})$	114.81º	17.95º		24.81º	49.63º	67.57º
$(\bar{2}00)$	90º	42.76º	24.81º		24.81º	42.76º
$(\bar{2}01)$	65.19º	67.57º	49.63º	24.81º		17.95º
$(\bar{2}02)$	47.24º	85.52º	67.57º	42.76º	17.95º	

Table A.6 Showing the calculated angles between planes of atoms with d-spacings matching closely with experimental data in Figure 5.4 (c).

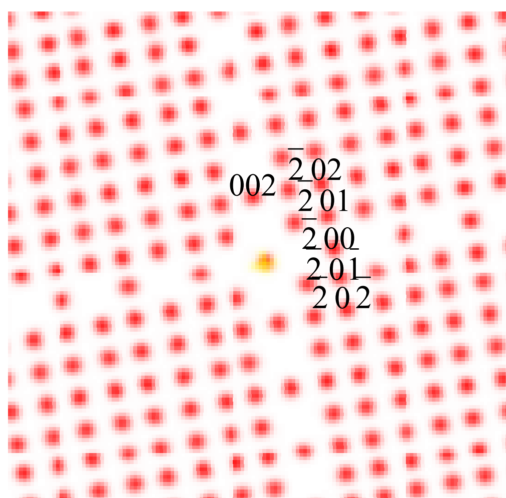

Figure A.7 Showing a simulated diffraction pattern of orthorhombic NiSi along the [010] zone axis.

A.6 Indexing SAED pattern from Figure 5.15 (b)

The square-array spot pattern of single crystal Si (100) with the [100] zone axis, indicated by a red square in Figure A.8 was used for the calibration of this SAED pattern (refer to section A.2). Other spots of interest are labeled in Figure A.8 and measurements

of the radius and calculation of d-spacing of each of the spots is represented in Table A.7. As shown in the table, the calculated d-spacings closely match with the d-spacings of the plane indices of the NiSi phase from the JCPDS file 38-0844.

To further verify that the calculated d-spacings of the spot pattern belong to the NiSi phase of JCPDS file 38-0844, step two was carried out by calculating the angles between the proposed planes of atoms as shown in Table A.8.

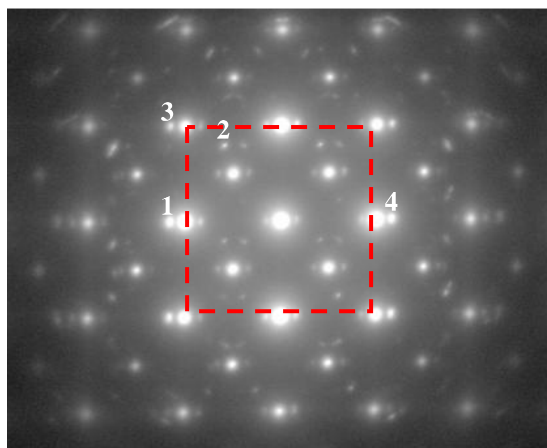

Figure A.8 SAED pattern from Figure 5.15 (b).

Finally, the experimental data is verified by simulating the diffraction pattern using JEMS. First the zone axis is calculated, which is the direction perpendicular to all the proposed plane indices. Using the dot product for vectors, the zone axis can be calculated as $[\bar{1}02]$. The simulated data indexed with NiSi plane indices is shown in Figure A.9. With reference to detailed analysis and evidence from experimental data, it can be concluded that the SAED from Figure 5.15 (b) is of orthorhombic NiSi with the MnP structure and space group Pnma (62).

Spot	Radius(r)	Calculated d-spacing (Å) = λL / r	d-spacing of planes of atoms from JCPDS file 38-0844 which matches the calculated values	
1	172	1.619	1.629	(020)
2	145	1.921	1.919	(211)
3	207	1.345	1.343	(221)
4	171	1.628	1.629	(020)

Table A7 Showing the comparison and analysis of the calculated d-spacings of Figure 5.15 (b) spot pattern with d-spacings from a standard JCPDS file 38-0844.

Planes	(020)	(211)	(221)	$(0\bar{2}0)$
(020)		53.91°	34.45°	180°
(211)	53.91°		19.46°	126.09°
(221)	34.45°	19.46°		145.55°
$(0\bar{2}0)$	180°	126.09°	145.55°	

Table A8 Showing the calculated angles between planes of atoms with d-spacings matching closely with experimental data in Figure 5.15 (b).

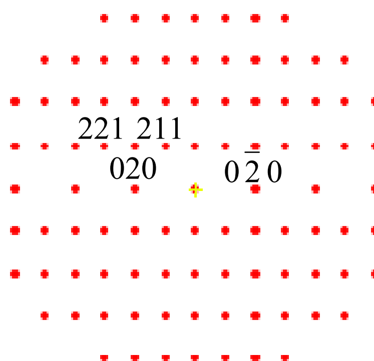

Figure A9 Showing a simulated diffraction pattern of orthorhombic NiSi along the [$\bar{1}02$] zone axis.